August 2020

A Study on the Dynamic Manipulation of Structured Light Using Orbital Angular Momentum for Wireless Underwater Links

Kaitlyn S. Morgan
Clemson University, ksm@g.clemson.edu

A STUDY ON THE DYNAMIC MANIPULATION OF STRUCTURED LIGHT USING ORBITAL ANGULAR MOMENTUM FOR WIRELESS UNDERWATER LINKS

A Dissertation
Presented to
the Graduate School of
Clemson University

In Partial Fulfillment
of the Requirements for the Degree
Doctor of Philosophy
Electrical Engineering

---

by
Kaitlyn Morgan
August 2020

Accepted by:
Dr. Eric G. Johnson, Committee Chair
Dr. Anthony Martin
Dr. Richard J. Watkins
Dr. Lin Zhu

ABSTRACT

In this work, the dynamic generation of structured light modes was demonstrated using coherent, co-aligned beams carrying orbital angular momentum (CCOAM). These modes are created using sources with blue/green wavelengths to study the effects of propagation and applications underwater maritime environments. Three techniques are discussed and are compared to simulation using a Rayleigh-Sommerfeld propagation kernel: concentric phase plates, Mach-Zehnder Interferometry, and the HOBBIT (Higher Order Bessel Beams Integrated in Time). These three systems are used to examine the modal integrity, controllability, and unique applications.

Structured CCOAM modes were first demonstrated using a 450 nm source and concentric phase plates and were propagated through 3 meters of turbid underwater environments. Beam coherence was measured using image registration, and the wavefronts were found to maintain their structure despite propagation through extreme turbidity. In addition, the source was amplitude modulated to verify that the mode structure can carry an amplitude modulation signal.

Next, an interferometry approach is used so that the two interfering modes can be controlled separately. The relative phase is controlled between the two interfering modes by manipulating the optical path length that each mode travels using an electro-optic phase modulator. Phase modulation allows for precise yet limited control of the wavefront and structure. Two setups were examined, a fiber-to-free-space Mach-Zehnder interferometer, and a HOBBIT system with two inputs. Phase only control was demonstrated using sinusoidal modulation and an orthogonal frequency division multiplexing (OFDM) signal

applied to the phase modulator. The modulated signals were successfully transmitted 3 and 6 meters through turbid water. Phase only modulation allowed for the transmission of a constant-amplitude signal, which provides nonlinear manipulation of the signal, such as amplification and harmonic generation, which are both crucial in creating high-power signals in the visible regime. The interferometry setups are very sensitive and a phase drift was found to occur due to temperature fluctuations and small movements of optical fiber in the setup, so a preliminary phase-lock loop was designed and tested to eliminate the phase drift. Without applied modulation, a RMS phase error of less than $\lambda/30$ was measured.

Lastly an acousto-optic deflector (AOD) was added to the HOBBIT setup, which adds mode tunability in addition to amplitude and phase control. The traveling acoustic wave also induces a frequency shift in the optical signal producing a continuous modulation of the output CCOAM mode. This is demonstrated by using a pulsed 450 nm diode to strobe the signal. Operation in pulsed mode enables the system to perform a self-referencing wavefront recovery from which the total OAM was extracted.

DEDICATION

To my family, friends and coworkers for their support and encouragement throughout this journey.

ACKNOWLEDGMENTS

I would like to thank my advisor, Dr. Eric Johnson, for his guidance, insight, and support throughout my graduate studies. Without his advice and encouragement I would not have had access to the ongoing research opportunities and incredible facilities. He also showed me how a small research question can grow and develop into something much bigger.

I would like to thank my committee members for their time, effort, and helpful advice: Dr. Anthony Martin, Dr. Richard Watkins, and Dr. Lin Zhu. I would also like to acknowledge Dr. Brandon Cochenour and Dr. Linda Mullen for introducing me to ocean optics and helping me during this journey.

I would like to thank the past and present members of the Micro-Photonics Laboratory. I would like to thank Dr. Keith Miller for his support and assistance and always being available to bounce ideas off of. I would like to thank Wenzhe Li, who has been working with me throughout this entire journey.

I would like to thank my family for their undying support, words of encouragement, and letting me ramble on and on about the projects I was working on.

Lastly, I would like to thank my fiancé, Taylor whose love and support was invaluable this entire time.

The funding for this research was provided by: N00014-16-1-3090, N00014-17-1-2779, N00014-18-1-2377, ONR N00014-141-0264, HEL-JTO/AFOSR FA9550-10-1-0543, ARO/MURI W911NF1110297, and ONR STTR N13A-023-0367

TABLE OF CONTENTS

Page

Table of Contents (Continued)

Page

LIST OF TABLES

Table Page

LIST OF FIGURES

LIST OF ABBREVIATIONS

AOD	Acousto-optic deflector
APD	Avalanche photodetector
AWG	Arbitrary waveform generator
BER	Bit error ratio
CCD	Charge-coupled device
CCOAM	Coherent co-aligned orbital angular momentum
CEOFDM	Constant-envelope orthogonal frequency division multiplexing
DPP	Diffractive phase plate
FDM	Frequency division multiplexing
FEC	Forward error correction
FOV	Field of view
FWHM	Full-width half-max
GaN	Gallium Nitride
HOBBIT	Higher Order Bessel Beams Integrated in Time
HOPES	Higher-order Poincaré sphere equivalent
MZI	Mach-Zehnder Interferometer
NPBS	Non-polarizing beam splitter
NRZ	Non-return-to-zero
OAM	Orbital angular momentum
OFDM	Orthogonal frequency division multiplexing
OOK	On-off-keying
PAPR	Peak-to-average-power ratio
PDM	Pulse division modulation
PLL	Phase locked loop
PPLN	Period poled lithium niobate
RMS	Root mean squared
SDM	Space division multiplexing
SLM	Spatial Light Modulator
SNR	Signal to noise ratio
QAM	Quadrature amplitude modulation
WUO	Wireless underwater optical

LIST OF SYMBOLS

A	Amplitude
c	Attenuation coefficient (m^{-1})
cz	Attenuation length
f	frequency
F	focal length of a lens
i	imaginary unit
m	OAM index; OAM charge number
M	Magnification factor
P	Power
r	Radial polar coordinate
R	Correlation Coefficient
$s(t)$	RF signal applied to AOD
$S(t)$	Piston wavefront due to the AOD
w_0	Beam waist (radius)
x	Cartesian coordinate (vertical)
y	Cartesian coordinate (horizontal)
z	Cylindrical/Cartesian coordinate and direction of propagation
δ	Total relative phase between two CCOAM beams
θ	Azimuthal polar coordinate
ϕ	Optical wavefront
Φa	Correlation optic a
Φb	Correlation optic b
Φu	Unwrapper log polar optic
Φw	Wrapper log polar optic
v	Frequency of light
ζ	Gouy phase
ξ	AOD first-order deflection angle

CHAPTER ONE

INTRODUCTION

1.1. Background

Orbital angular momentum (OAM) describes the component of angular momentum an electromagnetic field can carry due to the spatial distribution of the field, not the polarization. Since it was first measured in 1992 by Allen et. al. [1], the study of this phenomena has significantly grown due to their unique spatial distributions, orthogonality, and other characteristics. More recently, OAM has been brought into underwater environments to explore its utility in underwater optical links.

Underwater acoustic signals have been studied for over 100 years, predating the 1800s. In the early 1900s, after the sinking of the Titanic, acoustic systems were studied to detect icebergs. Since then, human activity underwater has grown and the technology has had decades of study and development to include sonar radar and acoustic communications which can reach distances in excess of 100 km at rates on the order of 1 kb/s. Still, there are several drawbacks to acoustic signals, including low directionality and therefore multipath loss, latency, and beam spread. As human presence in the underwater environment increases, these acoustic background noise levels are ever increasing as well. This not only affects marine life, but also can impact acoustic sensors and networks.

There is a growing interest in utilizing underwater optical links as a supplementation to acoustic networks due to their potentially high bandwidths, data rates, stealth, and significantly lower impact on marine life. Acoustic signals can travel kilometers, but they have an extremely long wavelength that limits modulation rates to the kHz. In addition,

these signals have very poor directionality. On the other hand, optical signals can be modulated at extremely high rates, but at much shorter ranges due to the attenuation of electromagnetic waves underwater. Because of this, the wavelengths typically used for free space communication links—such as infrared, radio waves, and microwaves—are only able to travel very short distances underwater.

Accordingly, the study of optical signals underwater is relatively new. Cochenour et. al have demonstrated that for a system with a wide field of view, high-frequency modulated signals experience greater latency affects due to scattering particulates than lower frequency amplitude modulation due to photons scattering out of the ballistic signal, then scattering back into the field of view (FOV) of the detector, decreasing signal fidelity [2]. One solution is to use structured light instead of a typical Gaussian beam, which facilitates filtering scattered photons out of the FOV and recovering transmitted information at extremely low photon levels. This can be done using an optical correlation, a simple and elegant solution to wavefront matching that has been utilized in optical signal processing since at least the late 1960s [3, 4, 5]. The general idea is that incoherent light, such as solar background will not be transformed while coherent light which may or may not include scattered photons from the source will not match and will be transformed out of the detector FOV.

Structured light can also be useful in increasing informational capacity of a photon, which is why we are particularly interested in using beams carrying OAM. There are several dimensions of an electromagnetic wave which can be controlled to extract or impart information. These include time, frequency, spatial structure, polarization, and complex

amplitude [6]. When used in a communication system, these control dimension are known as time division multiplexing, frequency division multiplexing (FDM), space division multiplexing (SDM) or mode division multiplexing, polarization division multiplexing (PDM), and quadrature amplitude modulation (QAM). Each of these dimensions can be combined without loss of information thus increasing the information carried by each photon. It is common practice to increase the data rate of a bandwidth limited system by combining as many of these controllable dimensions as possible. For example, SDM can be combined with PDM and QAM to maximize data transmission [7, 8, 9]. This is desirable because of the harsh environment as will be discussed in the following section.

1.2. Underwater Communications

Underwater acoustic transmissions have been well established for long distance underwater communications, but are lacking in data rate and security, making optical signals an attractive supplement for underwater wireless communications. Fiber-optic communications are a viable option for static transmitters and receivers but can be unsuitable for underwater vehicles, divers, etc., where tethering would limit operation. As mentioned above, traditional radio and microwave frequencies exhibit significant attenuation in seawater due to absorption, conductivity, and turbidity of the environment which is caused by impurities such as salts, floating sediment, or even microscopic organisms. The composition of the environment can significantly impact the optical signals. Generally, light in the blue/green range has been found to exhibit minimal absorption through water with wavelength depending on the composition [10, 11]. Visible light in the blue and green wavelengths have been used to successfully demonstrate links with

propagation distances of over 100 meters underwater [12, 13] and is therefore an exciting possible option for short-ranged wireless underwater optical (WUO) systems.

WUO links are primarily affected by absorption and scattering [2]. The attenuation of non-scattered light is characterized by the attenuation coefficient, *c*, which is the sum of the absorption coefficient and the scattering coefficient. Typical scattering coefficients for common underwater environments are shown in Table 1.2.1.

Table 1.2.1 Typical Ocean attenuation coefficients [14].

Water Type	**Absorption (m^{-1})**	**Scattering (m^{-1})**	***c*** **(m^{-1})**
Pure Sea	0.053	0.003	0.056
Clear Ocean	0.069	0.080	0.150
Coastal	0.088	0.216	0.305
Turbid Harbor	0.295	1.875	2.170

The non-scattered or ballistic signal attenuates exponentially according to the Beer-Lambert law [15]:

$$P = P_o \exp(-cz), \tag{1.1}$$

where P is the received power, P_o is the initial power of the transmitted signal, and z is the physical range that the signal travels. The product, cz, is the attenuation length. The absorption spectrum of water promotes operation of WUO links at blue/green wavelengths, with the ideal wavelength varying depending on the properties and particulate composition of the local water source. In fact, simply switching to a 1 μm source increases the attenuation coefficient by over 3 orders of magnitude. Most optical communication components and systems are designed and optimized at 1064 nm and 1550 nm, while devices for operation

at blue/green wavelengths are rare. For this reason, some of the work presented in this dissertation is presented using infrared wavelengths to demonstrate the proof of concept.

The Beer Lambert law gives the power attenuation of only the ballistic photons. The received power given in equation 1.1 decays exponentially proportionally to the attenuation length *cz* of the environment. In reality, the receiver can have a large field-of-view (FOV) such that some of the scattered photons can end up collected by the receiver. For higher particulate concentrations or long propagations distances, where *cz* is significantly large receivers can collect photons that have scattered multiple times. For illustration, this is typically noticeable when $cz > \sim 10$ for a FOV of ~5°, and is commonly referred to as the multiple-scattering regime and results in scattered light dominating the total received signal. The start of this region changes depending on the scattering properties of the particulates and the system FOV [2, 16, 17].

An example is shown in Figure 1.2.1 from [18]. In this work we examined the propagation of beams carrying OAM through laboratory simulated underwater scattering. The scattering environments were simulated using Equate® liquid antacid and polystyrene beads to create mie scattering. The liquid antacid is comprised of aluminum hydroxide and magnesium hydroxide particles which vary in size and shape but are on the order of 10-100s of microns. The polystyrene beads were 930 nm in diameter and are spherical. Thus, the scattering properties are expected to be different and show that the receiver collects a higher amount of scattered light for the liquid antacid than the beads. Interestingly there is more power collected at the receiver that is dependent on charge number, a value used to quantify

the degree of OAM that a beam carries and will be described in the next section, but this is most likely due to beam size after propagation than an effect of the OAM.

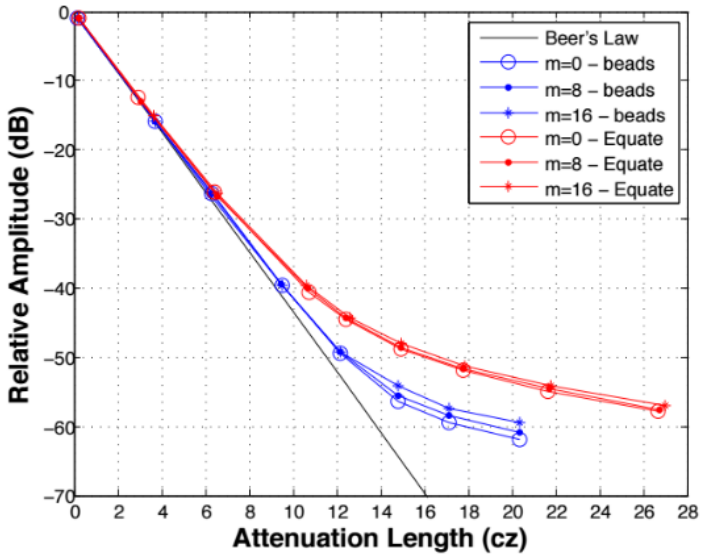

Figure 1.2.1 Underwater propagation of amplitude modulated spatial modes carrying orbital angular momentum, showing the attenuation divergence from the Beer-Lambert law after *cz* is greater than ~10 [18].

The underwater environment is bandlimited by scattering and absorption. By encoding information onto different photon dimensions – such as its complex amplitude, polarization, spatial structure, frequency, or in time – we can increase the spectral efficiency of the link, where the spectral efficiency η of the link is defined as the channel capacity in bits per second divided by the link bandwidth. Shannon's theorem limits the data capacity of a given link $\eta = \log_2(1 + S/N)$, where *S/N* gives the signal-to-noise ratio (SNR) of the link. When examining the maximum spectral efficiency of a modulation scheme, in general the more complex the modulation scheme, the closer the scheme can approach Shannon's limit but at the cost of a higher SNR requirement. This work will primarily focus on

encoding information in the spatial structure of a photon in combination with the beams complex amplitude.

1.3. Orbital Angular Momentum

In 1992, Les Allen et. al. showed that light beams with helical wavefronts can carry OAM [1]. The helical wavefront is commonly expressed using the OAM phase term $\exp(-im\theta)$, where i is the imaginary unit, θ is the azimuthal angle and m is the charge number. The charge number m in this work is used to describe the average OAM carried by each photon, it can be thought of as the number of 2π helical twists over one wavelength. A linearly polarized monochromatic electric field, propagating in the $+z$ direction and carrying OAM, can therefore be expressed in vector form by

$$\vec{\mathcal{E}}_m(r,\theta,z,t) = A_m(r,\theta,z)\cos\left(kz - 2\pi\nu t + \phi(r,\theta,z) + m\theta\right)\hat{x} \tag{1.2}$$

where $k = 2\pi n\nu/c$, n is the refractive index of the dielectric medium in which the light is propagating, c represents the velocity of light in vacuum, ν is the optical frequency and $A_m(r,\theta,z)$ and $\phi(r,\theta,z)$ are the amplitude and phase, respectfully of the wave at any position (r,θ,z). In this work, we are able to use a scalar representation of the electric field because the diffracting structures are very large compared with the wavelength of light [5]. Therefore we can generally use the scalar representation in phasor form:

$$U_m(r,\theta,z,t) = A_m(r,\theta,z)\exp\left(-i\phi(r,\theta,z) - im\theta\right) \tag{1.3}$$

The OAM term imparts an azimuthal phase dependence on the beam that appears as a 2π phase that ramps m times over one wavelength as shown in Figure 1.3.1. This spiraling of the wavefront gives OAM-carrying beams unique properties such as handedness, angular

momentum proportional to *m*, and mode orthogonality for integer values of *m*. For these reasons, OAM has been explored for use as optical tweezers [19, 20], imaging [21, 22], quantum information processing [23, 24], and also in atmospheric free space optical links [25, 26].

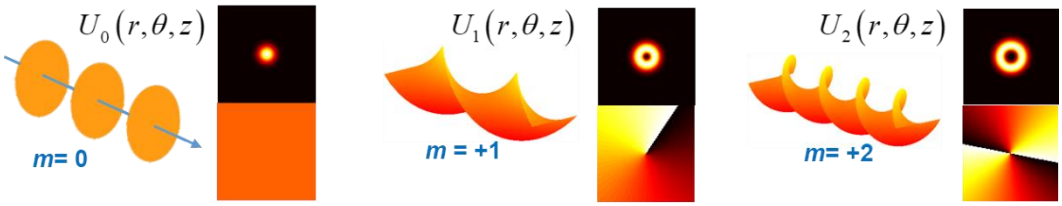

Figure 1.3.1 Three beams carrying OAM are illustrated, one without OAM (*m*=0), one with *m*=1, and one with *m*=2. Illustrations of the wavefront are shown, in addition to cross-sectional intensity profiles and optical wavefronts.

i. Incoherent underwater propagation

By taking advantage of the modal orthogonality, we were the first to demonstrate the use of OAM states in a SDM WUO link to increase the bandwidth of the underwater link despite an optically and temporally bandlimited channel [7]. In this work we demonstrate the incoherent superposition of two OAM states and successful modulation and separation of the signals after propagation through a turbid underwater environment. The setup is shown in Figure 1.3.3. The optical sources are two ThorLabs LDM9LP pigtailed laser diode mounts and output unpolarized light at 445 nm. The transmitter is comprised of two beams co-aligned using a non-polarizing beamsplitter. OAM is imparted onto each beam using spiral phase plates, the operation of which is illustrated in Figure 1.3.2 where the planar wavefront passes through the spiral phase plate. This phase plate has a varying azimuthal thickness, which produces the helical wavefront after the optical signal

propagates through due to the refractive index of the material. More details on optical fabrication are found in appendix A. The receiver is comprised of another non-polarizing beamsplitter to split the signal into two parts, where each is sent to an optical correlator designed to correlate with each transmitted mode. The beam profiles at one of the receivers are shown in Figure 1.3.4, where the bright center is collected on a detector. From this figure it is clear that there is minimal crosstalk between the modes because the correlator pushes the non-correlated beam outside of the detector field of view.

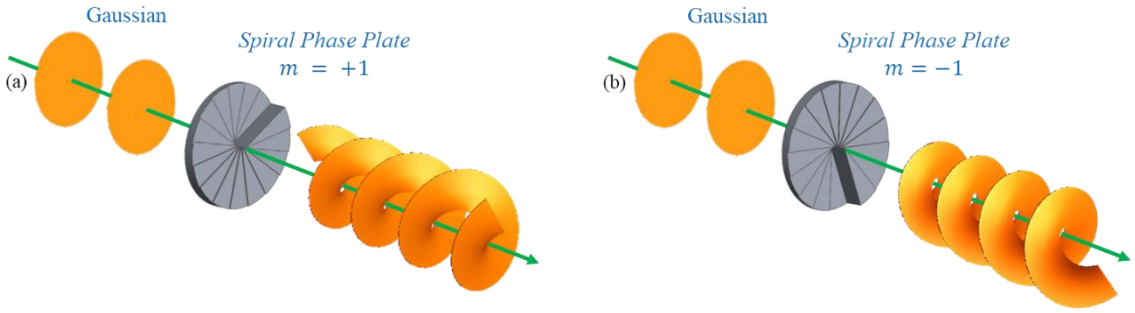

Figure 1.3.2. Generation of OAM beams using spiral phase plates for charge numbers (a) m = +1 and (b) m = -1

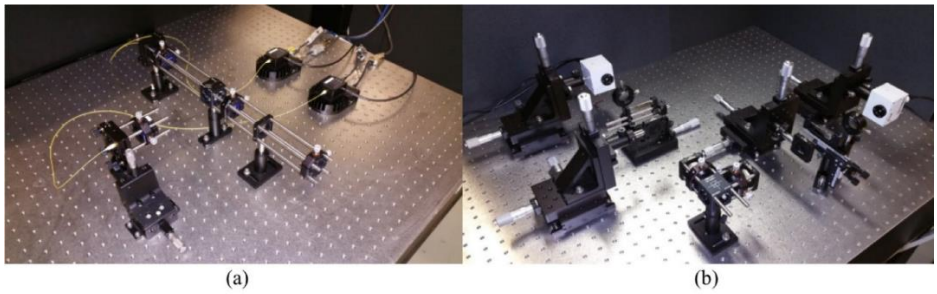

Figure 1.3.3. Photographs of the (a) transmitter and (b) receiver

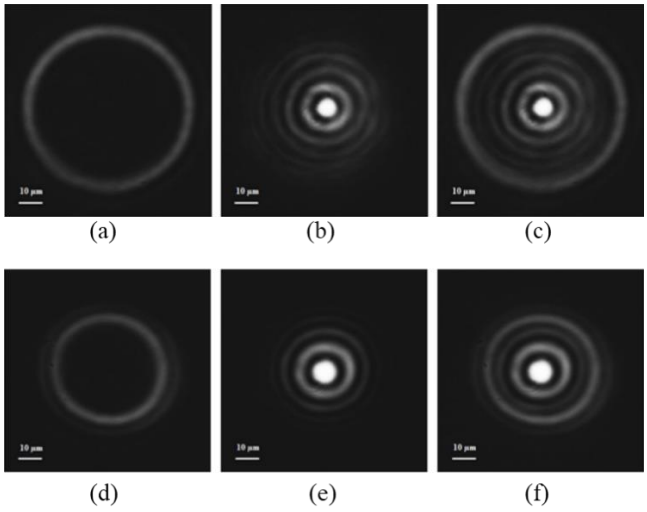

Figure 1.3.4 Demultiplexed image distribution of a (a) m = -8, (b) m = +8 and (c) m = ±8, all after propagating through the correlation optic for m = +8 and a (d) m = -4, (e) m = +4 and (f) m = ±4, all after propagating through the correlation optic for m = +4.

In this work, we demonstrated the successful simultaneous transmission and recovery of two 1.5 Gbps amplitude modulated signals using the incoherent combination of different OAM states. This is possible due to the orthogonality of different OAM charges, but also demonstrated that the wavefronts are minimally impacted by the scattering environments. More recently, this method was used to demonstrate a 40-Gbps link [9] and was also combined with PDM [8].

The study of the propagation of OAM states in underwater environments is of growing interest and there are many interesting discoveries. The optical wavefront is recoverable and are orthogonal despite propagation through turbid environments [25, 7]. It has also been shown that different OAM states have different scattering cones depending on the charge number [18, 27, 28]. The main question is to what extent we can exploit the

spatial aspects of OAM while still recovering the signal such that we can improve WUO links.

1.4. Structured Light

In order to exploit the spatial properties of OAM, we need easy ways to generate the modes. There are several common techniques used to create structured light using both passive and active techniques. For the purpose of this work we will focus on methods that are used to generate beams carrying OAM. Passive techniques include cylindrical lenses [29], spiral phase plates [30], metamaterials [31], and geometrical transformations such as the log-polar transformation [32, 33, 34]. Active techniques include spatial light modulators [35, 36, 37],and liquid-crystal q-plates [38].

By coherently superimposing beams carrying OAM, the spiraling wavefronts interact to create unique azimuthally periodic interference patterns. An example is shown below

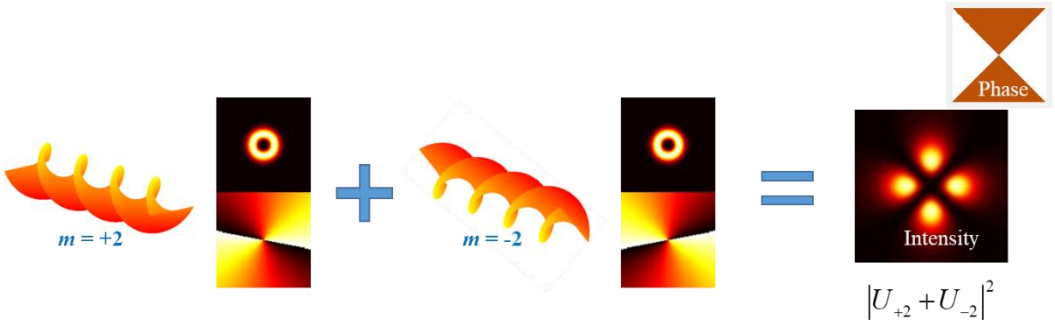

Figure 1.4.1 The coherent combination of two opposite-handed helical wavefronts produce azimuthally distributes interference fringes.

There are countless interesting applications of structured light including structured light illumination for computational imaging, compressive sensing, wavefront control

through turbid/turbulent media. On the communications side, structured light can be used in space-division multiplexing or mode-division multiplexing in addition to use as a carrier for amplitude modulation.

When using optical signal underwater, it is important to have elements that can handle higher power applications due to the high attenuation of the environments. Therefore, spatial light modulators and liquid crystal devices are not ideal due to their lower damage thresholds. These elements are also relatively slow, having modulation rates on the order of 30 Hz for most common devices.

This work will present four techniques of generating structured light, each with their own advantages and disadvantages and all exploiting the wavefront of beams carrying OAM to generate the structured light modes. The first employs a single optical phase plate etched with two concentric OAM wavefronts. The second employs a Mach-Zehnder interferometry system to create two different and coherent and co-aligned OAM (CCOAM) wavefronts and then combine them using superposition. The final two use a series of geometrical transformations including two cylindrical lenses known as the HOBBIT (Higher Order Bessel Beams Integrated in Time) system.

The HOBBIT system uses optical geometrical transformations to creates beams that carry OAM. The first implementation of the HOBBIT system linearly converts a displacement into beams carrying OAM. For example, a fiber array with four outputs could be used as the input to the system to create four OAM beams with equally spaced charge numbers. The second implementation utilizes the HOBBIT system in conjunction with an acousto-optic deflector (AOD) cell, combining both passive and active elements to create a

highly dynamic system that linearly translates the deflection from the AOD into a corresponding OAM charge. This second system can be used both to rapidly switch modes and also precisely control the wavefront.

1.5. Peer work and state of the art

As mentioned above, there is a plethora of applications using structured light and OAM states; therefore the generation and control of structured light has been studied in various systems.

In 2018, we demonstrated a multilevel quadrature amplitude modulation (QAM) equivalent technique without using amplitude modulation to increase data throughput by mapping spatial structure to a 2D vector space using interferometry and phase modulators [39]. Later in 2018, we showed that by adding amplitude control we can create a 3D-QAM equivalent scheme by mapping spatial structure to a 3D-vector space that is a higher-order Poincaré equivalent sphere for these structured modes [40]. In 2019, Zhao et. al. demonstrate an interesting technique of generating beams with spatiotemporal control using multiple optical frequency comb lines [41].

On the sensing side, structured light has been used in computational imaging applications. In 2009, Jack et. al. demonstrated ghost imaging using a spatial light modulator (SLM) to create coupled OAM states [22]. In 2013, Lavery et. al. used coupled OAM states generated using an SLM to detect a rotating object [42]. In In 2016, Ryabtsev et. al. demonstrated the use of OAM states to measure vorticity in fluids also using an SLM to generate the modes [43]. In 2017 Akhlagi and Dogariu demonstrated the use of stochastic structured light to track objects that are visually obscured by turbid environments [44]. In

2017, Cochenour et. al. demonstrated object detection in a turbid underwater environment using beams carrying OAM [45]. In 2020, Watkins et. al. showed the potential application of characterizing atmospheric turbulence using a continuous scan of OAM states [46].

In 2014, Strain et. al. demonstrated OAM mode switching at speeds of 10 and 20 μs using a compact vortex emitter operational at near-infrared wavelengths [47]. In 2017, Lei et. al. demonstrated a high capacity router that was able to create 49 OAM channels with switching speeds of 6.9 μs [48]. Log-polar optics designed to perform a geometrical transformation of an optical signal from Cartesian coordinates to a log-polar coordinate system were first presented in 2010 by Berkhout et. al. [49], though the optical transformation had been studied in other optical applications previously to create rotation invariant optical systems [50]. In 2016, Ruffato et. al. demonstrated using the optics in reverse to create OAM states [34]. In 2019, Li et. al. demonstrated a tunable OAM generator with a switching speed of 2.3 μs [32]. In 2019, Ruffato et. al. explored overcoming limitations of the log-polar optics [51]. In 2020, Dai et. al. demonstrated wavelength scalability of OAM generation using the HOBBIT system and second harmonic generation [52].

For higher degrees of control, coherent combinations of OAM states have been explored. In 2001, Mair et. al studied entangled OAM states using spontaneous parametric down conversion to generate the states [53]. In 2014, Krenn et. al. used these same modes in a 3 km atmospheric communication link using a SLM to generate the wavefronts of OAM combinations at speeds of 20 s [36]. In 2014, Anguita et. al. explored various combinations

of OAM states to create highly complex intensity profiles using a spatial light modulator [54].

1.6. Motivation

Principally, the work presented in this dissertation has the goal of controlling structured light modes created with CCOAM states for underwater environments in order to increase the spectral efficiency of a given link. In the future, we will utilize the control of these mode to create sensor systems to characterize the underwater and maritime environments. It has been well established that electromagnetic communication and sensing systems are flip sides of the same coin. They both face the similar environmental issues, only one is trying to compensate or work around environmental factors, while the other quantifies those same factors. In addition, modulation rates can be vastly different. Also, visible light signals can provide higher resolution than is achievable through the traditional acoustic signals, has better directionality and therefore security, and finally has a much lower impact on marine life.

The primary areas of interest are as follows: how well do these beams hold up in harsh underwater environments and how precisely can we control and manipulate the beams. Answering these questions will pave the way for the use of these beams. First we must examine the spatial structure of these modes after propagation through harsh environments and determine whether or not this spatial structure is compromised when controlled and manipulated at high rates. Second, we must examine how precisely we can control and manipulate these basic combinations. Thirdly, we must ensure the power scalability of mode generation for future applications by combining the system with a pulsed

source. Answering these three questions will promote and enable the future study of CCOAM states as a remote sensor, imager, or communications tool.

1.7. Dissertation Outline

In this dissertation, chapter one discusses the motivation and background of our work as well as the state of the art of related works.

Chapter two will introduce a passive optical element called a concentric phase plate that can be used to create structured light by creating CCOAM modes. The resulting wavefronts will be compared to simulation to explore beam development during propagation as a result of concentric phase plate design. Three different concentric phase plates will be used to create structured light that will then be propagated through a turbid environment to explore how robust these modes are. We will also apply an amplitude modulation to the signal to demonstrate communication capabilities of these specific beams in maritime environments.

Chapter three will discuss two alternative systems that can generate light in a similar manner to the concentric phase plates but will open up additional degrees of freedom in the control of the wavefront. The first is a Mach-Zehnder interferometry system used to create CCOAM states and the second is a geometrical transformation system referred to as the HOBBIT system which uses a series of optical transformations to create both OAM and CCOAM states. System and modal similarities and differences will be explored as well as system drawbacks. The results show that phase control can add an additional degree of control that can be precisely manipulated in order to increase data capacity of a link even through high scattering environments.

Chapter four will introduce an acousto-optic deflector (AOD) to the HOBBIT system and discuss the functionality of this system for generating multiple CCOAM states. It will introduce optical Doppler effects on the electromagnetic wave as a result of propagation through a traveling acoustic wave. Finally it will cover the combination of the system with a pulsed source to demonstrate imaging of the AOD-HOBBIT system.

Chapter five will summarize the studies throughout the dissertation and outline the future research.

CHAPTER TWO

STRUCTURED LIGHT USING PASSIVE OPTICS

2.1. Introduction

Previously we have examined the propagation and modulation capabilities of incoherent OAM states with symmetric profiles in WUO systems [7, 18]. In this chapter we will explore spatial profiles generated using concentric spiral phase plates to create combinations of coherent OAM states. The concentric OAM states produce interference patterns with azimuthally periodic locations of constructive and destructive interference due to the OAM phase terms. Typically, CCOAM states are created through free space interferometric setups such as the Mach-Zehnder interferometer and require extremely precise alignment [20, 54]. Free space interferometry is heavily dependent on coherence length and therefore, precision of alignment and optical path length are typically critical. Instead, the states can be generated using a single diffractive phase plate (DPP), which allows us to use a source with short coherence length to study these beams. Diffractive optical elements are designed and fabricated to realize three different CCOAM states at 450 nm. The propagation of these beams through turbid water is studied to determine their suitability for future underwater optical links.

2.2. Passive optical elements: diffractive phase plates

In this work, we use DPPs to generate the CCOAM states. These optics operate similar to the spiral phase plates introduced in section 1.3. These passive optics have several advantages over SLMs. First, the optics have 100% fill factors, which have unparalleled efficiency. The resolution of SLMs is limited to the pixel size and coding scheme, whereas

the resolution of diffractive optics is limited only by the fabrication technique used. Additionally, because these devices are comprised of fused silica glass, they can be utilized in high-power optical systems, whereas SLMs could sustain damage. Additionally, using a fused silica DPP does not have any thermal or electrical requirements since it is a purely passive optical component.

The DPPs consist of the concentric combination of two spiral phase plates, one inside the other. The inner portion has counter-clockwise phase wrap of $(m_1 \times 2\pi)$ and the outer region has a clockwise phase wrap of $(m_2 \times 2\pi)$, where m_1 and m_2 represent the respective OAM mode indices. The phase profile of a concentric DPP is given by

$$\varphi(r,\theta) = \begin{cases} \exp(-im_1\theta), & 0 \le r < r_1 \\ \exp(-im_2\theta), & r_1 \le r < r_2 \\ 1, & r_2 \le r \end{cases} \tag{2.1}$$

where θ and r are polar coordinates. The values of r_1 and r_2 determine the radius of the inner and outer OAM phase plate respectively. The three fabricated phase plates are shown in Figure 2.2.1 with more details given in Appendix A.

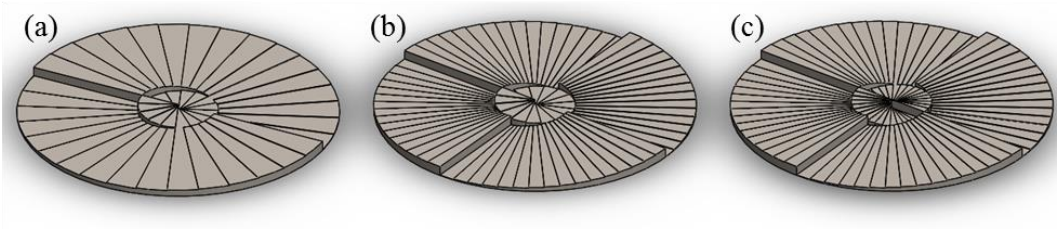

Figure 2.2.1 Schematic drawing of the concentric DPPs with (a) m_1 = 1 and m_2 = -2 (b) m_1 = 1 and m_2 = -4 and (c) m_1 = 2 and m_2 = -4.

If the phase element represented in equation (2.1) is illuminated with a Gaussian beam, the resulting beam at the optic planecan be represented in scalar form as:

$$u(r,\theta)=\begin{cases}\exp\left(-2r^2/w_0^2\right)\exp\left(-im_1\theta\right), & 0\le r<r_1\\ \exp\left(-2r^2/w_0^2\right)\exp\left(-im_2\theta\right), & r_1\le r<r_2\\ \exp\left(-2r^2/w_0^2\right), & r_2\le r\end{cases}. \tag{2.2}$$

A proportionate percent of power is passed through the inner and outer portions of the DPP in order to form the interference patterns, illustrated in Figure 2.2.2. The limits of equation 2.1 and 2.2 are derived from the power in a normalized Gaussian Beam. When the ratio of r to w_0 are altered, the resulting interference patterns change as shown in Figure 2.2.3(a-c).

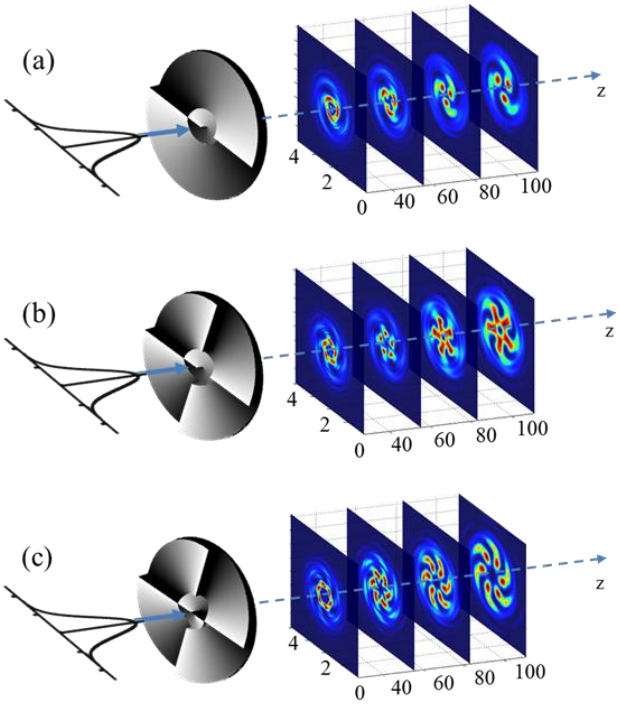

Figure 2.2.2. Schematic diagram for concentric vortex beam generation by the DPP with (a) m_1=1 and m_2=-2, (b) m_1=1 and m_2=-4, and (c) m_1=2 and m_2=-4 showing propagation of a Gaussian beam through the optical element (Dimension unit: mm)

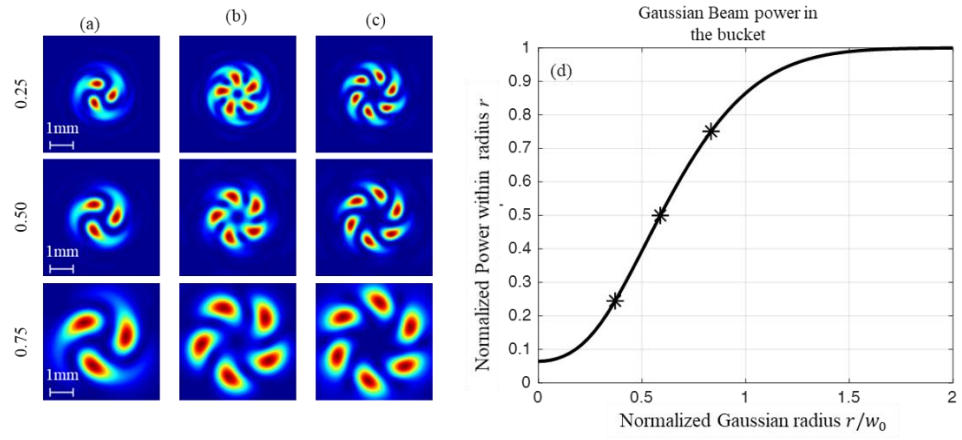

Figure 2.2.3. Three meter propagation of a Gaussian after passing through DPPs with (a) $m_1 = 1$ and $m_2 = -2$ (b) $m_1 = 1$ and $m_2 = -4$ and (c) $m_1 = 2$ and $m_2 = -4$ for three different power ratios passing through the inner and outer OAM plate. (d) Bucket power of a Gaussian beam as a function of bucket radius r normalized by the Gaussian beam waist w_0.

Figure 2.2.3 shows that by changing r/w_0, the intensity profiles are minimally impacted. Additionally, the resulting power passing through the inner portion as a function of incident Gaussian beam waist is plotted in Figure 2.2.3(d). The concentric vortices examined in this paper and the interference of OAM modes are quite similar in nature and have yet to be investigated for their propagation properties through turbid media or underwater propagation.

As the beam propagates, the two portions diverge and combine both as a result of the divergence of the OAM beam [55] and the discontinuity at r_1.

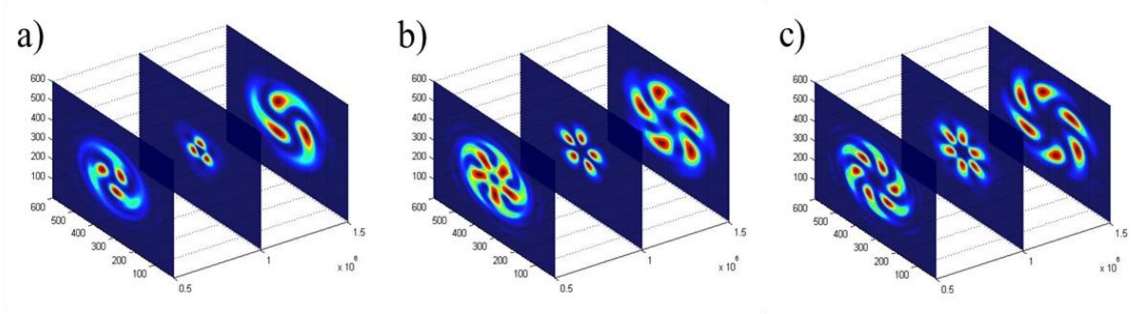

Figure 2.2.4. Illustration of beam development for the propagation of the three concentric vortices through a lens with focal length = 1.0 m. (Dimension unit: mm) (a) m_1 = 1 and m_2 = -2 (b) m_1 = 1 and m_2 = -4 and (c) m_1 = 2 and m_2 = -4

The resulting intensity profiles shown in Figure 2.2.4 experience a slight left-handed rotation due to the natural divergence of the beam components [20]. By exploiting Gouy phase, this handed nature can be used to determine distance protection. When these profiles are passed through a lens, the beam appears to rotate until the focal plane where the phase shifts and the resulting output appears to rotate in the opposite direction, shown in Figure 2.2.4. Additionally, it can be observed that the interference fringes also rotate with propagation. For the case of superimposed optical vortices where the relative phase of the two beams, δ, remains constant, the resulting angular change in the profile position between two points along the direction of propagation is defined as

$$\Delta\phi_v = \frac{|m_1| - |m_2|}{m_1 - m_2}\zeta\delta\,, \tag{2.3}$$

where $\zeta = \tan^{-1}(z / z_R)$ is the Gouy phase and z_R describes the Raleigh range [20]. By combining this property with image processing technologies, these intensity profiles could

be used to probe an environment and obtain ranging information. It is important to note that the relative phase cannot be changed on the optics after fabrication. In order to induce rotation, one can simply rotate the optic.

2.3. Simulation results

A numerical implementation of the Rayleigh-Sommerfeld diffraction integral [5] is used to simulate the development of these beams through a non-scattering environment, and given by

$$U_p(x,y) = \iint u(\xi,\eta) \frac{e^{i\frac{2\pi z}{\lambda}\sqrt{1+\left(\frac{x-\xi}{z}\right)^2+\left(\frac{y-\eta}{z}\right)^2}}}{i\lambda z\left[1+\left(\frac{x-\xi}{z}\right)^2+\left(\frac{y-\eta}{z}\right)^2\right]} d\xi d\eta, \tag{2.4}$$

where $U_p(x,y)$ is the electric field at the observation point $p(x,y)$, $u(\zeta,\eta)$ is the electric field within the aperture and in this case is defined by equation 2.2, and z is the propagation distance from the input plane where the phase optic is illuminated to the plane where the point $p(x,y)$ is located.

For this simulated propagation, $u(\zeta,\eta)$ has r_1 = 0.625 mm, r_2 = 2.5 mm and w_0 = 1.15 mm, matching the design specifications used in the experiment. In this case, approximately 45% of the Gaussian power passes through the inner vortex while 55% passes through the outer.

Additionally, these beams must travel some distance before the interference patterns form properly as can be seen in Figure 2.2.2. Intensity profile images were captured in air at different distances from the phase plate and compared to simulation results for the same

corresponding distances, illustrated in Figure 2.3.1, in order to demonstrate the development of the spatial profile. These intensity profiles are imaged in the near-field. Therefore, the profiles will continue to morph as they travel through the link, yet from Figure 2.3.2 it is apparent that after propagation of 1 meter through water, the change in intensity profile is negligible. At a wavelength of 450 nm, water has a refractive index of approximately 1.34 and was utilized to extend the optical path length of the simulation after the propagation through air.

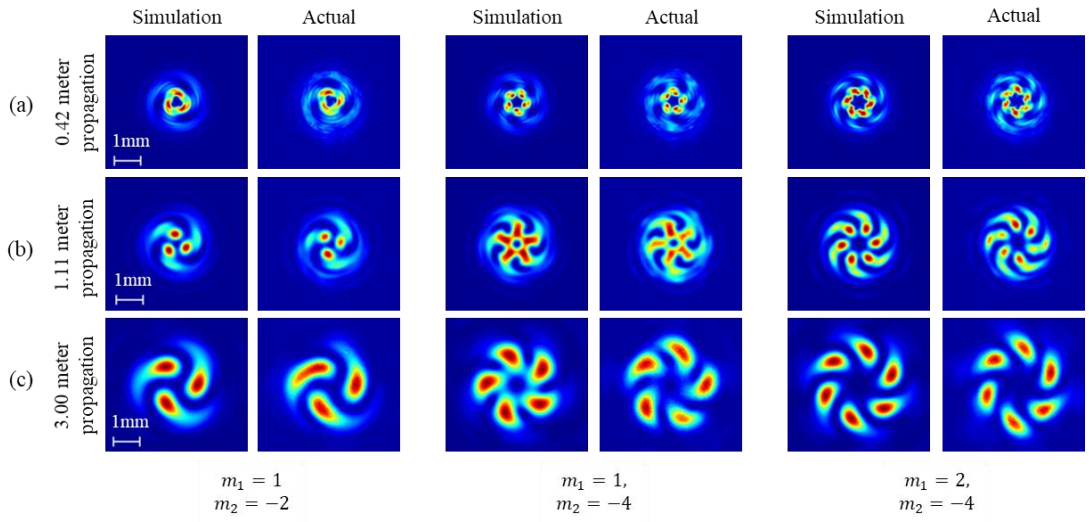

Figure 2.3.1. Propagation simulation in air of the development of concentric vortex beams of intensity profiles after propagation through corresponding concentric phase plate (a).

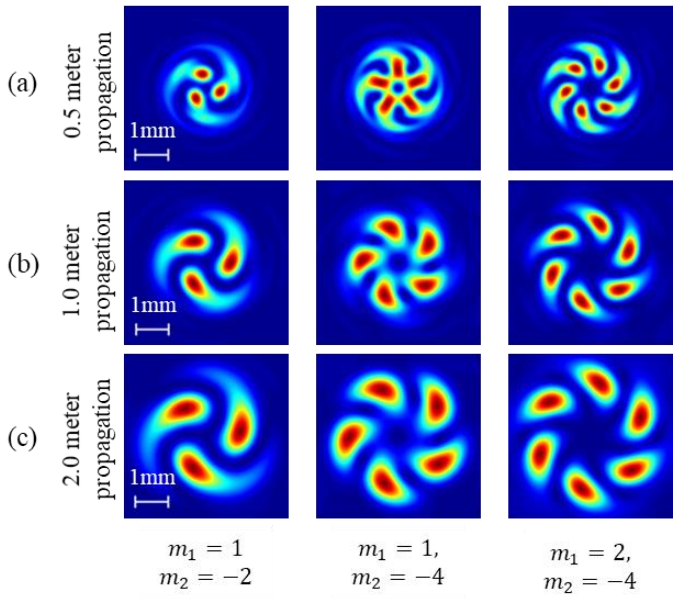

Figure 2.3.2. Simulated concentric vortex development after (a) 0.5 m, (b) 1.0 m, and (c) 3.0 m through water channel after 1.11 m propagation through air.

2.4. Experimental results

To examine the effects of a turbid environment on the propagation of these concentric vortex beams, two types of measurements were performed with a free-space link. The first type of measurement was performed using a setup illustrated in Figure 2.4.1. The light source was a mounted ThorLabs LDM9LP laser diode operating at 450 nm, corresponding to the approximate absorption minimum in clear ocean water. The output power was controlled electrically with a DC Bias current. The output from the fiber pigtail is connected to a collimator and then expanded using a Keplerian telescope system to achieve a collimated Gaussian with a 2.3 mm diameter. The Gaussian beam is then passed through the diffractive phase plate and propagates approximately 1.11 meters before entering the water channel. This distance was selected such that the interference between

inner and outer generated vortex beams have propagated far enough to give a distinct pattern when comparing constructive and destructive interference, seen in Figure 2.3.1, while still able to capture the entire beam on the CCD (charge coupled device) array after propagation through the water channel as simulated in Figure 2.3.2. This also tells us that these beams are still partially developed until propagation of about 1 meter into the water channel. Afterwards, these beams continue to propagate the remaining 1.96 meters through the water channel.

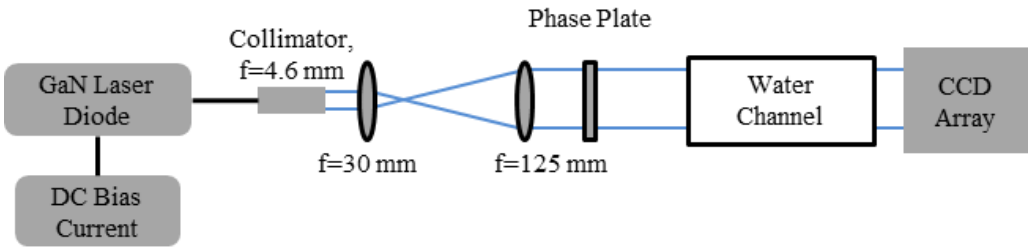

Figure 2.4.1. Schematic overview of the link.

Liquid antacid was used to increase turbidity in the water channel, this substance has long been used to emulate oceanic conditions [56]. The attenuation coefficient of each solution was determined by measuring the laser power before and after the water channel, and attenuation according to the Beer Lambert law was verified. After transmission through the channel, the attenuated beam is imaged onto a WATEC 902-H2 visible CCD camera. The collected images are processed to calculate the correlation coefficient between the clear-water case and turbid cases.

The calculation of the coefficient was done using the 2-dimensional form of the Pearson Product moment, given by

$$R = \frac{\sum_d \sum_e (A_{de} - \bar{A})\left(B_{de} - \bar{B}\right)}{\sqrt{\left(\sum_d \sum_e (A_{de} - \bar{A})^2\right)\left(\sum_d \sum_e \left(B_{de} - \bar{B}\right)^2\right)}}. \tag{2.5}$$

In this equation, A and B are two D by E images, where A_{de} corresponds to the pixel value in image A at location [d,e], B_{de} gives the pixel value in image B at location [d,e], and the first moment of image A and image B are expressed as

$$\bar{A} = \frac{1}{DE} \sum_d \sum_e A_{de} \tag{2.6}$$

$$\bar{B} = \frac{1}{DE} \sum_d \sum_e B_{de} \tag{2.7}$$

The correlation coefficient is calculated for the whole image where D = 512 pixels and E = 480 pixels and the pixel pitch is 9.8 μm. Individual shifts in the image were corrected for prior to computing the correlation coefficients. It is important to adjust for any slight misalignments of the CCD array from successive measurements which can be caused by replacing the water in the channel. Rotation of the images was not an issue, since these beams do not show any rotation with increasing turbidity and the optical path length does not significantly change between runs.

The intensity profiles of the propagated concentric vortices after propagation through clear and highly turbid water are shown in Figure 2.4.2. These images are juxtaposed with the corresponding simulated beam using the optic described in equation 2.1. The clear water images approximately match that of these simulations. The irregular

intensity distribution between the interference fringes can be attributed to a slightly oblong incident Gaussian beam. After propagation through the turbid environment the low frequency information in the intensity profile sees very little distortion. The scattering is obvious from the high frequency intensity profile information as a result of the scattering medium. To quantify this scattering contribution, a correlation coefficient is computed for the beams without scattering agents added to the water and at various points with increasing scattering as a result of increasing the liquid antacid concentration.

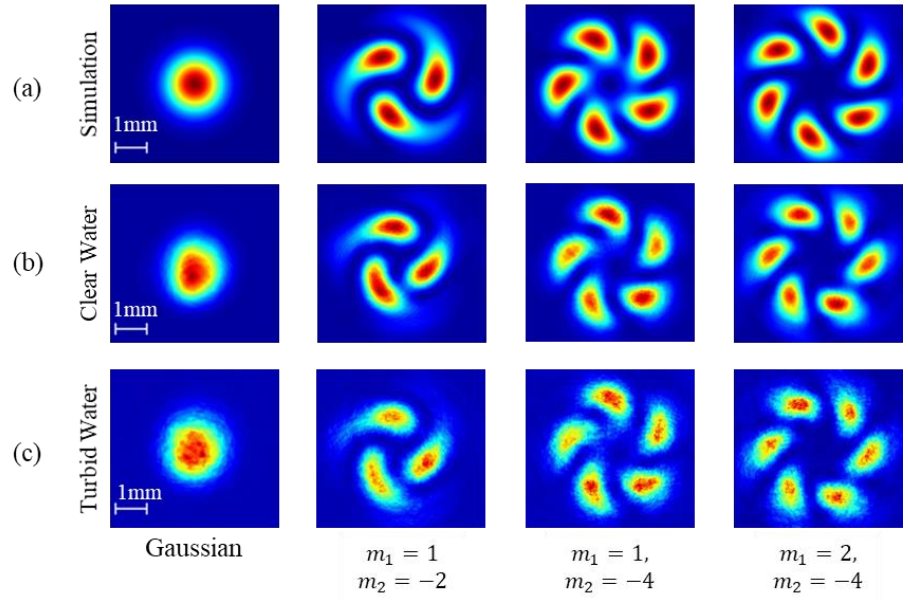

Figure 2.4.2. Intensity profiles for (a) simulated propagation through air with an equivalent optical path length (OPL) of approximately 5.1 m from the phase plate, (b) propagation with through $cz \cong 0.2$, and (c) $cz \cong 13$.

The correlation coefficients calculated for each case are compared in Figure 2.4.3. As the attenuation coefficient of the water channel is increased, the correlation coefficient for each beam decreases. This is a result of light scattering into the CCD array, which

produces distorted images while reducing the contrast of the image. These correlation coefficients are comparable to that of a Gaussian beam despite having a more complex intensity profile. Each calculated coefficient is well over 0.9, where 1 corresponds to perfect correlation and 0 to no correlation. This indicates excellent preservation of the spatial profiles despite propagation through extremely turbid conditions.

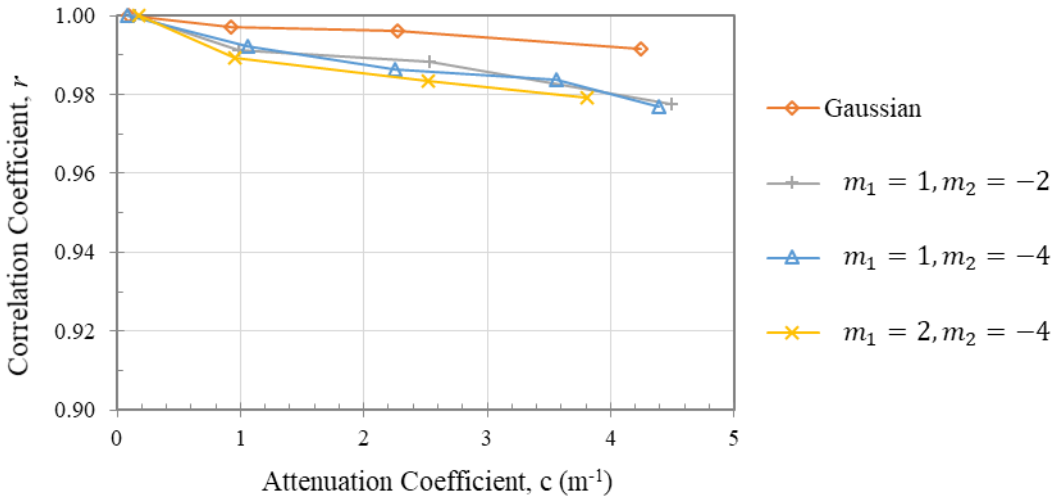

Figure 2.4.3. Comparison of correlation coefficients after propagation through 3 meters of turbid media showing excellent correlation (>>0.9)

In addition to investigating the integrity of the spatial beam patterns, a second measurement was made to characterize the temporal characteristics of the link. Amplitude modulation will determine whether the increase in turbidity will impact data rates of standard binary amplitude modulation of the 450 nm laser. The original setup was modified to the design indicated in Figure 2.4.4. A signal consisting of a 32-bit, pseudo-random, M-series, on-off keying, non-return-to-zero (OOK-NRZ) bit sequence operating at 1.5 GHz was generated using a Tektronix AWG615, Arbitrary Waveform Generator. This signal was

then amplified using a 10 dB Picosecond Pulse Labs 5828-MP amplifier, and combined with a DC bias current through a bias tee located in the ThorLabs LDM9LP pigtailed laser diode mount. The AWG output signal was optimized for the diode such that after the amplifier the AC current was 50 mA peak-to-peak with a DC bias of 60 mA.

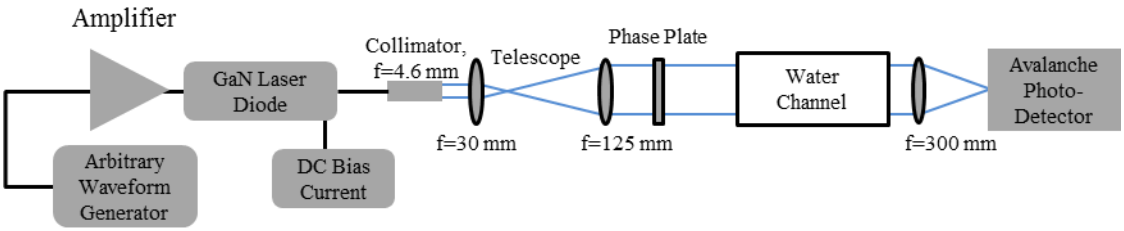

Figure 2.4.4. Schematic overview of setup modification for modulation implementation.

After propagation through the link, the optical signal was focused onto a Menlo Systems APD210 Si Avalanche PhotoDetector (APD) using a 300 mm focal length lens. The converted electrical signal was fed directly into a Tektronix TDS8200 digital sampling oscilloscope. An eye diagram was created using a collection of 1000 waveforms and is shown in Figure 2.4.5, for each concentric vortex. The mean and standard deviation of the upper and lower rails were measured on these eye diagram using a histogram. The window used was measured from 40% to 60% of the bit period. These values were used in estimating the bit error ratio (BER) of the signal using the formula below for equal probability signals for "1" and "0":

$$BER = \frac{1}{4} erfc\left(\frac{\mu_1 - V_{th}}{\sigma_1\sqrt{2}}\right) + \frac{1}{4}\ erfc\left(\frac{V_{th} - \mu_0}{\sigma_0\sqrt{2}}\right) \tag{2.8}$$

where μ_j and σ_j are the mean and standard deviation of the signals j = 0 or 1,

$$erfc(x) = \frac{2}{\sqrt{\pi}} \int_x^{\infty} \exp\left(-t^2\right) dt, \tag{2.9}$$

and V_{th} is the threshold voltage of the received signal given by

$$V_{th} = \frac{\mu_0 \sigma_1 + \mu_1 \sigma_0}{\sigma_0 + \sigma_1}. \tag{2.10}$$

The BER was measured for clean and turbid water with an attenuation coefficient of approximately $cz = 0.27$ and $cz = 1.48$, respectively. Higher coefficients were not measured due to the low signal power at these higher turbidities causing a decrease in the signal-to-noise ratio of the APD. The field of view was limited by the 300 mm focal length lens and the 0.5 mm detector diameter. The full-angle field of view was calculated to be $0.02°$ using $\text{AFOV} = 2 \times \tan^{-1}\left(h/2f\right)$ were h is half of the detector diameter and f is the focal length of the lens.

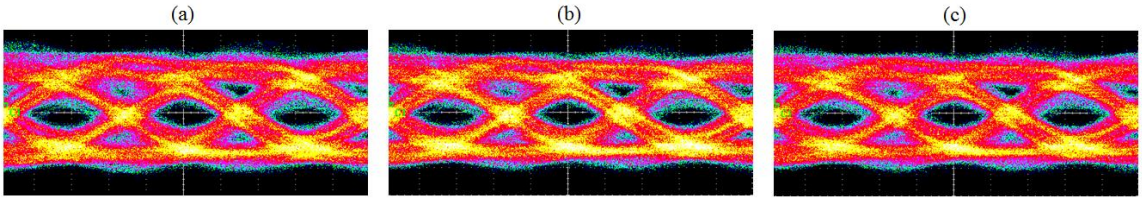

Figure 2.4.5. Eye diagrams from the CCOAM stats with (a) m_1=1 and m_2=-2, (b) m_1=1 and m_2=-4, and (c) m_1=2 and m_2=-4

The BER of each eye diagram was estimated using equation 2.8 and is reported in Table 2.4.1. It is most likely that the higher BERs for the larger charge numbers can be attributed to the increased divergence. This will result in a higher percentage of the signal

collected by the APD. Additionally, signal modulation at 1.5 GHz showed no degradation over the turbidities tested. The consistencies are promising, but because measurements were limited, more work needs to be done exploring the effect of higher turbidity on modulation. Widening the field of view and decreasing the photon count would lend more insight into the characterization of temporal scattering.

Table 2.4.1. BER of propagated beams.

State	**cz=*0.27***	**cz=*1.48***
Gaussian	$5.96\cdot 10^{-4}$	$5.96\cdot 10^{-4}$
m_1=1 and m_2=-2	$5.47\cdot 10^{-4}$	$5.34\cdot 10^{-4}$
m_1=1 and m_2=-4	$5.39\cdot 10^{-4}$	$5.71\cdot 10^{-4}$
m_1=2 and m_2=-4	$6.32\cdot 10^{-4}$	$6.74\cdot 10^{-4}$

The BERs are below the limit of 10^{-4} for a system utilizing forward error correction (FEC) techniques. The consistency of the correlation coefficient, in addition to successful modulation demonstrates the ability to maintain the more complex spatial profile despite extreme turbid conditions. It is important to note that these beams encountered minimal turbulence and it would be interesting to examine the response of these beams to turbulence as well. Furthermore, it will be useful to examine other combinations of concentric vortices in order to further explore the propagation properties

2.5. Summary

The use of a single optical element, the concentric DPP, is a simple method of generating the CCOAM states through interferometry. Segmenting the optical element eliminates the need for free space interferometric methods, which minimizes alignment constraints when studying non-dynamic modes. This is also important for optical sources with short coherence lengths, as is typical in GaN laser diodes in the 450-470 nm spectral

range. DPP elements are also very efficient in the generation of such beams and can withstand high power densities if necessary. In this chapter, three different concentric DPPs were designed to generate three combinations of CCOAM states; however, more complex beams could be possible, such as the combination of 3 or more states.

The three CCOAM states were propagated through a water channel to investigate the spatial and temporal characteristics of a free-space underwater communication link using CCOAM structured light modes through highly turbid environments. The scattering levels investigated herein are comparable to that of highly turbid ocean harbors. Despite the propagation through approximately 13 attenuation lengths, well within the multiple scattering regime, the spatial profiles were maintained as demonstrated with correlation coefficients in excess of 0.97 as when compared with the lowest attenuation case. This preservation of beam quality and temporal modulation is quite promising for communication, imaging, and sensing applications in oceanic environments.

In addition, to understand the impact on directly modulating the optical source and its impact on a binary data communication channel, high data rate modulation was demonstrated at 1.5 GHz for conditions exceeding that of a coastal ocean. The BERs realized were on the order of 10^{-4} for the OOK-NRZ pulses from a directly modulated 450 nm GaN laser diode. Increasing receiver aperture and field of view stands to extend the operating range of the optical link, though the contribution of multiply scattered light will warrant additional study on the behavior of OAM states as well as the high speed data it carries. One feature of this approach is that multiple concentric vortices can be used to increase the data rate by realizing parallel optical channels.

In this chapter we were the first to examine the propagation of these CCOAM beams through underwater turbid environments. We showed that these structured light modes can be easily created using DPPs consisting of concentric spiral phase plates, even for sources with low coherence. In addition, we found that the spatial structure of these modes is well maintained even after propagation through extreme turbidity. Finally we demonstrated that information can still be transmitted using these structured modes in a manner similar to the incoherent SDM OAM system presented in chapter 1. The spectral efficiency of the link created in this work is not improved ($\eta \leq 1$) over that of a simple amplitude modulated Gaussian beam, because there is no dynamic control over the mode structure, but we do know that physically rotating the DPPs produces a rotation in the interference fringes. Naturally, this led us to wonder if there could be an advantage to using a different setup so that we can more dynamically control these modes, such as a Mach-Zehnder interferometry setup.

CHAPTER THREE

DYNAMIC STRUCTURED LIGHT USING COHERENT COALIGNED OAM

3.1. Introduction

From the previous chapter, we found that we can easily create CCOAM beams using a single optical element. If instead we use separate components to create the OAM beams then coherently couple them together using interferometric techniques such as a Mach-Zehnder interferometer (MZI), we gain an additional degree of freedom for dynamic control [57, 58]. The MZI setup is not ideal because combinations are not limited to two beams [59], alignment can get complex, and each additional beamsplitter will produce a 3 dB power loss. By using interferometry we will be able to control the relative phase between the two interfering modes at rates that well exceed that of a SDM. These types of signals are commonly used in the study of quantum entanglement and the control is used to verify the Bell inequality. CCOAM beams for quantum entanglement are typically generated at very low powers using an SLM, neither of which are acceptable for communications.

Phase control will enable CCOAM modes to be used to rapidly manipulate the beam profile in space and time, opening up an additional dimensionality for encoding information using phase modulation [60, 40]. Traditional methods of encoding information on the amplitude of the signal are highly effective in typical cases, but can be disadvantageous in underwater environments where power scalability is important.

As discussed in the previous chapter, CCOAM beams can be created using concentric DPPs and result in azimuthally periodic locations of constructive and destructive

interference depending on the OAM charge numbers chosen. The same is true for two interfering OAM states combined using an MZI. For the most basic case of two identical beams with equal but opposite charge numbers, equation 1.3 can be re-written as

$$U_{+m}+U_{-m}=\sqrt{\rho(t)}A_{|m|}(r,\theta,z)\cos\left(\frac{\chi(t)}{2}\right)\exp(-im\theta) \\ +\sqrt{\rho(t)}A_{|m|}(r,\theta,z)\sin\left(\frac{\chi(t)}{2}\right)\exp(im\theta)\exp(i\delta(t)) \tag{3.1}$$

where $A_m(r,\theta,z)$ defines the amplitude profile of the beam and is dependent on the method of mode generation in spatial coordinates, ρ controls the total power of the signal, χ controls the power ratio between the two states, and δ is an additional phase difference. Equation (3.1) shows that we have temporal control of (ρ,χ,z) in addition to our choice of m. For a beam propagating through a spiral DPP, the amplitude profile can be represented by a Laguerre-Gaussian component given by [61]:

$$A_{|m|}(r,\theta,z)=\sqrt{\frac{2}{\pi(|m|)!}}\frac{w_0}{w(z)}\left(\frac{r\sqrt{2}}{w(z)}\right)^{|m|}\exp\left(-\frac{r^2}{w^2(z)}\right)L_0^{|m|}\left(\frac{2r^2}{w^2(z)}\right)\times \\ \exp\left(-ik\frac{r^2}{2R(z)}\right)\exp(i\zeta(z)) \tag{3.2}$$

where $L_{p=0}^{|m|}$ are the generalized Laguerre polynomials, $w(z)$ is radius at which the field amplitude falls to $1/e$, w_0 is the beam waist, $R(z)$ is the radius of curvature, and $\zeta(z)$ is the Gouy phase at z. These modal combinations can be mapped to a Hilbert space similar to the higher-order Poincaré sphere used to map polarization vector beams. Instead we will be using the higher-order Poincaré equivalent sphere (HOPES) [62] to represent the modal

combination given by equation 3.1. A general concept is given in Figure 3.1.1 which illustrates control of both the relative phase δ and total amplitude ρ for the coherent combination of $m = +1$ and $m = -1$ with equal powers.

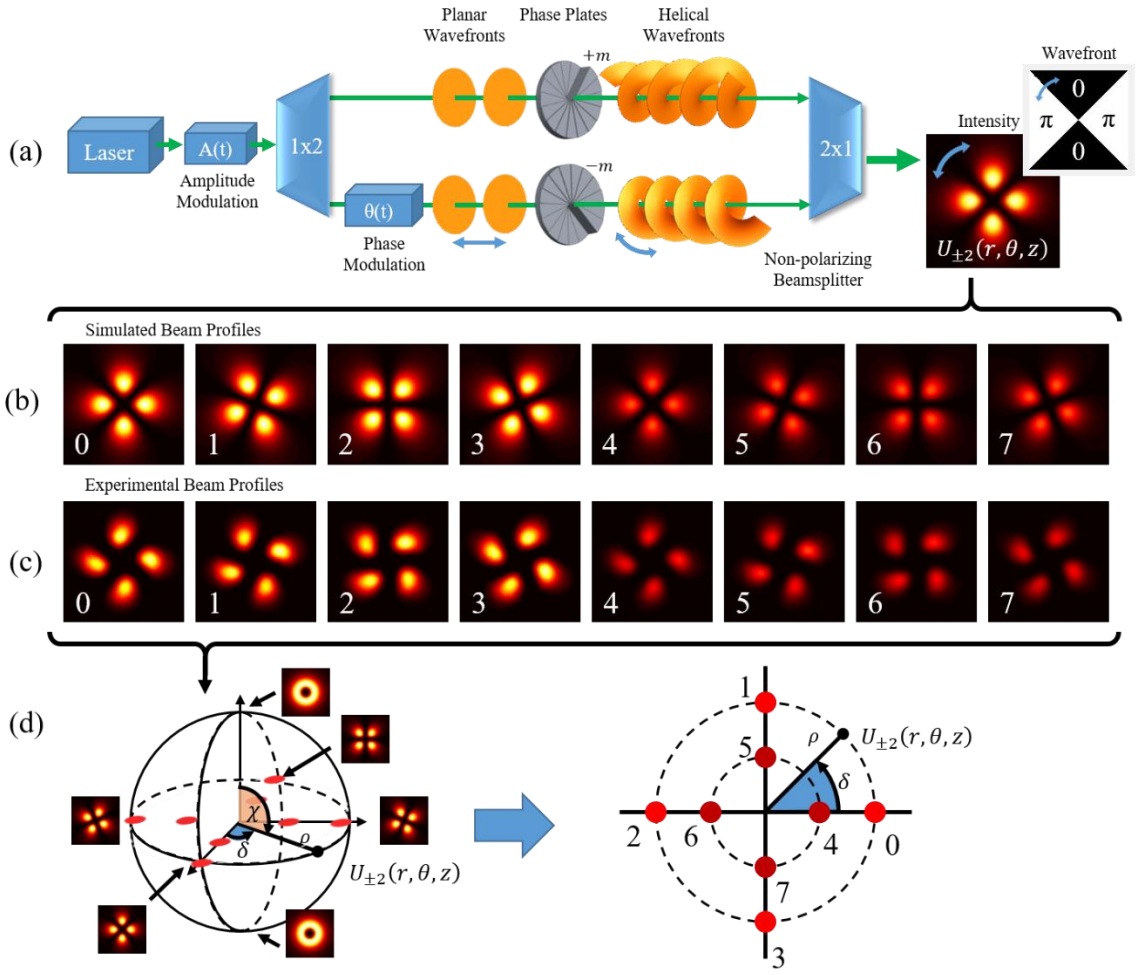

Figure 3.1.1 (a) Modulation concept illustrating Generation of CCOAM states. (b) Simulated output images for an 8-symbol system compared to (c) corresponding experimental images, which can then be mapped to (d) constellation space on the equator of a higher-order Poincaré sphere equivalent, with symbol locations indicated on the equator plane where $\chi=\pi/2$, and ρ and δ are controlled.

For the case where both beams have equal power, $\chi = \pi/2$, so the beam is mapped to the equator of the HOPES sphere shown in Figure 3.1.1 (d). Equation 3.1 can be simplified to

$$U_{+m} + U_{-m} = \sqrt{\frac{\rho(t)}{2}} A_{|m|}(r,\theta,z)\cos\left(m\theta + \frac{\delta(t)}{2}\right). \tag{3.3}$$

The two combined beams have identical intensity profiles A_m and only differ in the helical rotation of the wavefront illustrated in Figure 3.1.1 (a). When they are coherently co-aligned, the equal but opposite wavefronts cancel producing a binary wavefront with an intensity profile defined by

$$|U_{+m} + U_{-m}|^2 = \frac{\rho^2}{2} |A_{|m|}(r,\theta,z)|^2 \cos^2\left(m\theta + \frac{\delta}{2}\right). \tag{3.4}$$

The intensity profile will therefore rotate on axis proportional to $\delta/2m$, as can be seen in Figure 3.1.1 (b,c).

In this chapter we will explore two interferometry techniques to create the CCOAM modes: a Mach-Zehnder interferometry system and a series of geometrical transformations known as the HOBBIT system which creates Higher Order Bessel Beams Integrated in Time. Both systems have their own unique advantages and disadvantages and create slightly different output modes.

First we will demonstrate proof-of-concept work at 1550 nm using the MZI setup. Here we will demonstrate both amplitude and phase control which will allow us to fully access the Poincaré equivalent space. Next we will demonstrate a similar system at 532 nm. To create high-powered CCOAM beams in the green regime, the phase modulated CCOAM beam at 1064 nm is used to pump a nonlinear period poled lithium niobate (PPLN) crystal to generate a 532 nm signal. This complex process and its full effect on beams carrying

OAM is not within the scope of this work, but in general and for the following applications, the charge number *m* is doubled and this is briefly discussed in section 3.3. This is a nonlinear process, and is therefore extremely amplitude sensitive so this experiment will demonstrate precise phase-only control as these signals are used in an underwater communications link.

3.2. Amplitude and phase control

In this section we present a proof of concept for precise and rapid amplitude and phase control using a 1550 nm source [40]. As the basis of this work, the modulation concept of OAM beams is shown in Figure 3.2.1. The actual setup uses fiber-to-free space interferometry setup with a 1550 nm source attached to 1x2 fiber coupler. The two outputs of the coupler are each attached to a fiber coupled amplitude and phase modulator. The output s of the phase modulators are collimated and propagated through an $m = +2$ spiral phase plate which are then superimposed and co-aligned using a non-polarizing beamsplitter. Both optics have the same helicity because one will be flipped after reflection through the beamsplitter.

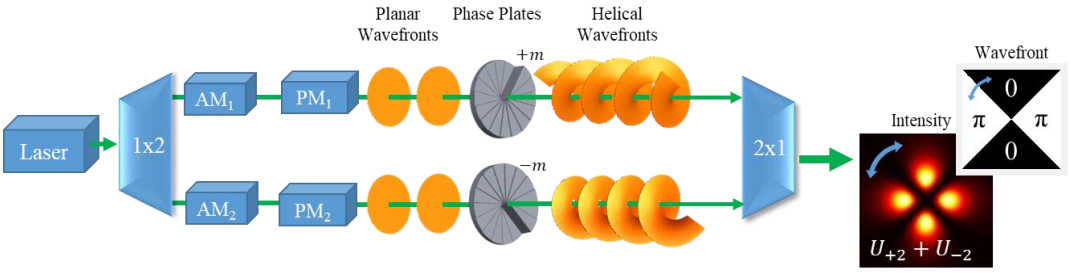

Figure 3.2.1. Setup illustration for the interference of OAM beams with opposite spiral phase with both amplitude and phase modulation with the 1x2 splitter coupled into the amplitude modulators (AM) and phase modulators (PM).

The relative phase delay δ between the two OAM beams is controlled using the phase modulators and will change the azimuthal locations of the interference fringes. As mentioned in section 3.1, a HOPES can be used to represent any combination of these two modes using the relative phase and powers of the two CCOAM states. The states are mapped to the HOPES using equivalent Stokes parameters [63]. By using these parameters we can map the position on the HOPES using four optical correlations. For more details on optical correlations and the HOPES, see appendix B. The full setup schematic is shown in Figure 3.2.2

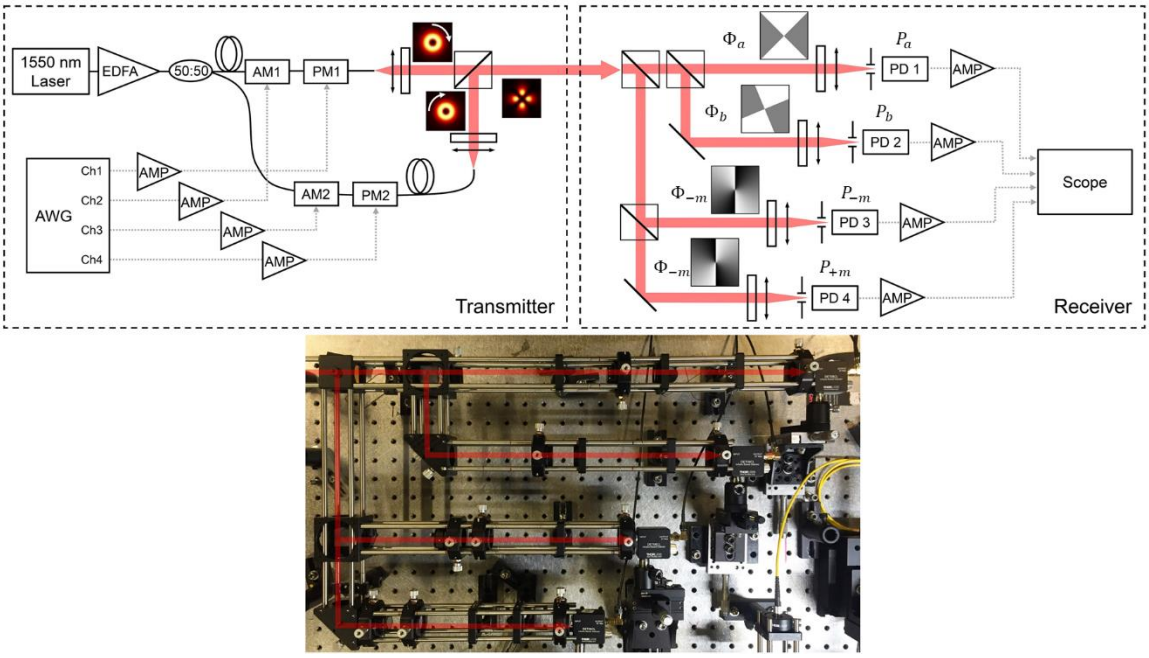

Figure 3.2.2. The experiment setup of the CCOAM communication system and the actual receiver picture.

In this work, a discrete set of point locations on the HOPES are used as symbol locations in a 3D constellation map, similar to the image shown in Figure 3.1.1 (d), with modulation information carried on the amplitude and phase of the beam profile. To implement the above mentioned concept into an optical communication system, a more general expression can be derived for an arbitrary symbol pulse representing the complex field of two co-polarized coherent OAM beams, with a total power, ρ, power ratio between each beam, α.

$$\begin{aligned} U_{KNL}(\rho_K,\alpha_N,\delta_L,t) &= U_{+m}(\rho_K,\alpha_N,\delta_L,t)+U_{-m}(\rho_K,\alpha_N,\delta_L,t) \\ &= \sqrt{\rho_K g(t)\alpha_N{}^2}\exp(-im\theta)\exp(-\frac{i\delta_L}{2}g(t)) \\ &+\sqrt{\rho_K g(t)(1-\alpha_N{}^2)}\exp(+im\theta)\exp(\frac{i\delta_L}{2}g(t)) \end{aligned} \tag{3.5}$$

In this case, $g(t)$ is Gaussian pulse shaping function for the amplitude and phase and, where χ is the polar coordinate used to map to the Poincaré sphere. Using this expression for a symbol in time, a pulse train with amplitude and phase modulation can be generated by encoding a symbol pulse every T seconds resulting in the following

$$p(t) = \sum_n U_{KNL}(\rho_K, \chi_N, \delta_L, t) * \delta_{impulse}(t - nT). \tag{3.6}$$

$U_{KNL}(\rho_K, \chi_N, \delta_L, t)$ is the complex field of the CCOAM optical signals which carry the multidimensional amplitude and phase modulation information encoded by the phase and amplitude modulators using the discrete power levels, discrete power ratios and the discrete phase levels mapped as 3D symbol locations denoted by combination of index *K*, *N*, and *L*. When the complementary power ratios α_N and $\sqrt{1-\alpha_N^2}$ is satisfied such that the total power is constant with ρ_K, the symbols lie on the *K*th sphere. *N* denotes the number of lateral symbol levels on *K*th sphere, or the number of latitude positions of the symbols: changing α_N moves the *N*th symbol along the Z-axis between the two poles. This can be determined using the elevation angle of the symbols, χ_N, using $\alpha_N = \cos(\chi/2)$ and $\sqrt{1-\alpha_N^2} = \sin(\chi/2)$, where $\chi_N \in [0, \pi]$. The values of χ_N are chosen so that the mapped symbol latitudes are equally spaced and are far enough from the poles to distinguish the azimuthal symbols. Experimentally, changing χ_N is accomplished by picking the proper working voltage for the chosen amplitude modulators shown in Figure 3.2.2, AM_1 and AM_2, so that the amplitude ratio for the two states is satisfied. On the *N*th latitude, symbols are discretized by phase location δ_L with equal phase spacing of $2\pi/L$ where *L* is the number of discrete

phase positions of the symbols on each latitude. The relative phase $\delta_L \in [0, 2\pi]$ is equally split between the two CCOAM states by using the proper working voltages for both phase modulators PM_1 and PM_2 simultaneously and in synchronization. The function $g(t) = exp(-t^2 / 2\tau^2)$ is the Gaussian shaping function and has a 30% pulse width τ and pulse period of T for both the amplitude and phase modulation signals. In this work, the modulation rate $1/T$ is 1.0 GBd.

Thus, through the amplitude and phase control of the two CCOAM states, symbols are mapped into 3D spherical space with *K*-sphere, *N*-latitude and *L*-phase. A total M_{KNL}-QAM equivalent 3D constellation scheme, where $M=KNL$. Data comprised of $\log2(M)$ bits can be mapped into M symbols with different spherical radius, latitude and phase positions.

Experimental Results

To recover the modulation information, the position of the symbols on 3D spherical space must be projected onto the three orthogonal axis set, which are equivalent to the Stokes parameters, S_1, S_2 and S_3. The recovery of both amplitude and phase modulation signals utilizes an optical correlation setup similar to our previous works [7, 39]. Optical correlators are commonly used in many mode detection applications where a phase-match element is designed to match and cancel the phase profile of the incident beam to form a correlation peak in the detection plane by exploiting the Fourier-transformation property of lenses. In order to recover the 3D information, four detections are necessary: two to recover the amplitude modulation and two to recover the phase modulation. The on-axis correlation spot power in the Fourier-plane indicates how closely the phase of the incident mode matches that of the phase-match element. As we have shown in previous work [39], the

phase difference between the CCOAM beams, δ, is recoverable through two optical correlations with the azimuthally offset cosine functions, Φ_a and Φ_b.

$$\Phi_a = \cos(m\theta), \qquad (3.7)$$
$$\Phi_b = \cos\left(m\left[\theta - \frac{\pi}{4m} \right] \right).$$

For the detection of the amplitude modulation θ, spiral phase plates are used as the match filter, given by Φ_{-m} and Φ_{+m}.

$$\Phi_{+m} = \exp(-im\theta), \qquad (3.8)$$
$$\Phi_{-m} = \exp(+im\theta).$$

The optical correlation of the incident beam through these four optics produces on-axis correlations spots with varying intensities given by

$$P_a = \rho\left[1+\sin(\chi)\cos(\delta)\right] \qquad (3.9)$$
$$P_b = \rho\left[1+\sin(\chi)\sin(\delta)\right]$$
$$P_{+m} = \frac{\rho}{2}\left[1+\cos(\chi)\right] \quad .$$
$$P_{-m} = \frac{\rho}{2}\left[1-\cos(\chi)\right]$$

Using these four expressions we can map the four signals to Cartesian coordinates using

$$X = P_a - \rho \qquad (3.10)$$
$$Y = P_b - \rho \quad .$$
$$Z = P_{c1} - P_{c2}$$

where $\rho = P_{+m} + P_{-m}$. For more details on the HOPES sphere, see appendix C.

In order to demonstrate the feasibility of this communication link, multidimensional 64- and 128-star QAM maps are used to transmit symbols at 1.0 GBd. MATLAB is used to create a uniform pseudorandom bit sequence (PRBS) using a Mersenne Twister pseudorandom number generator. The experimental results for both 64- and 128-QAM equivalent star constellations are shown in Figure 3.2.3 at the corresponding highest measured signal-to-noise (SNR) level, 16.8 and 17.3 dB, respectively. The symbols of different latitudes are represented by alternating dark and light colors. Sphere radii are represented with blue, orange, or purple colors. The 64-QAM constellation represents K=2, N=4, L=8 and M=KNL=64. This system has a spectral efficiency of $\eta \leq 6$ bits/s/Hz. The 128-symbol constellation should ideally represent K=2, N=8 and L=8. However, due to the limited optical power of the transmitter, an alternative with K=3, N_1=2, N_2=8, N_3=6, L=8 yielding M=(N_1+N_2+N_3)L=128 symbols is shown. This system has a spectral efficiency of $\eta \leq 7$ bits/s/Hz. The separation on both Z-axis and azimuthal direction are distinguishable and therefore enables decoding of each symbols. In order to visualize the 3 spheres of the 128-QAM constellation, symbols on each sphere are separated and plotted individually.

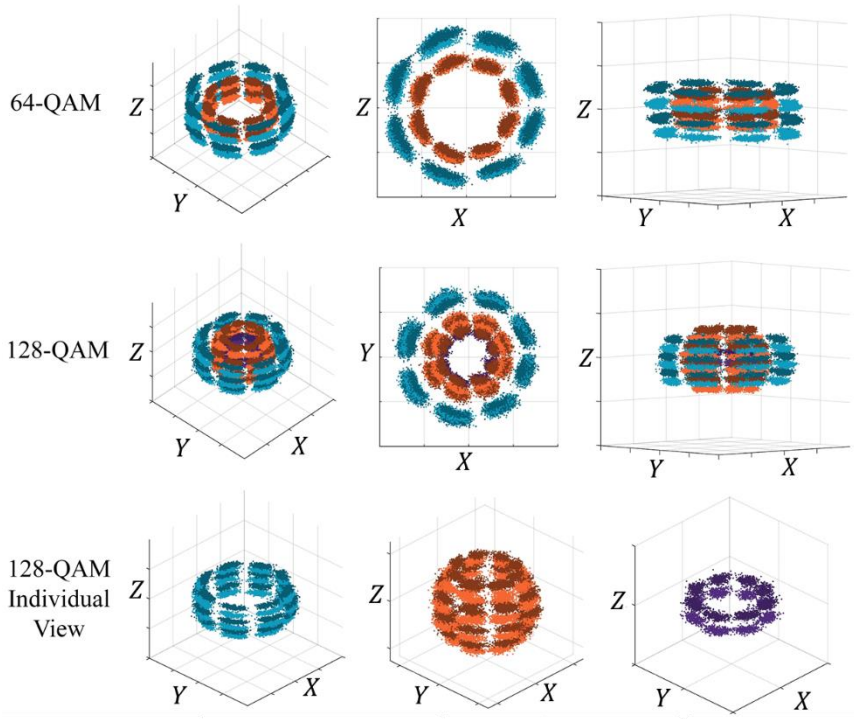

Figure 3.2.3. The measured double sphere 64-QAM and triple-sphere 128-QAM 3D star constellations plotted in a normalized optical power scale. For 128-QAM constellation, individual spheres are also shown in different scales.

The experimental constellation plots do not have perfect symmetry and distributions; multiple parameters could change the symmetry and distort the sphere which could cause additional errors in decoding. One defect is a tilt of the sphere axis, subtle but present in all experimental measured constellations. This is caused by a small amount of crosstalk between the two detections, P_{+m} and P_{-m}, mainly due to pinhole mis-alignment before the photodetector yielding an imperfect optical correlation. From section 1.3, recall that a higher separation of charge numbers minimizes channel crosstalk and should be explored in the future. Along the z-axis, errors will be caused by latitude level distortion, or uneven level spacing due to uneven power between the two OAM modes. As long as the

uneven balance of optical powers is minimal, the symbol locations will remain separable in Z-axis and will therefore minimally affect the BER.

3.3. Phase-only control for underwater signals

In this section, a phase-only modulated CCOAM beam is used to pump the nonlinear PPLN crystal to activate the second-harmonic generation process. This is necessary to create a high-powered optical signal with green light while maintaining modal control due to the nonlinear process of the second harmonic generation. Not only would amplitude modulation become distorted through the second-harmonic generation, but this process becomes more efficient for signals with higher power densities. This is why we are interested in using phase only modulation: the total beam power is ideally unchanged which we can see from the total power ρ.

The setup for this experiment is as follows: the CCOAM beam is generated using fiber-to-free space interferometry as in the previous section but without amplitude modulators in line, as illustrated in Figure 3.3.1. The CCOAM beam is focused through the PPLN crystal and collimated on the output. For simplicity, linearly polarized Laguerre-Gaussian modes are used in the theoretical analysis to approximate the incident mode.

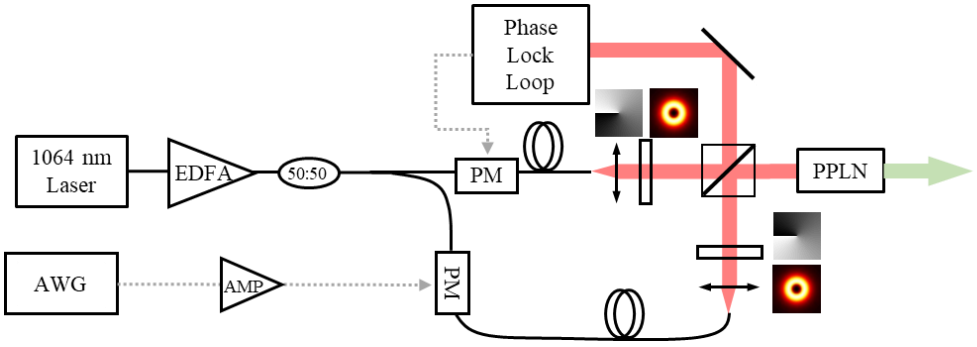

Figure 3.3.1. Setup visualization. The transmitter with m = +1 beams (rings) which are combined (two-lobes) using a beam splitter and transmitted to the frequency doubling crystal (three lobes). The 532 nm signal is then transmitted through a 3 meter water channel to the receiver comprised of a correlation setup and high-speed PIN detector. In addition, a portion of the signal is used to monitor and correct the phase drift from the fiber-based interferometry system.

The 1064 nm incident mode can be represented in scalar form by the sum given in equation 3.1, where U_m are the Laguerre Gaussian components and is given by equation 3.2, According to the nonlinear theory discussed in [64], the frequency doubled field of an OAM beam with charge number m can be approximated by

$$\begin{aligned}\vec{U}_{2m}(r,\theta,z,t) &\propto \left[\vec{U}_m(r,\theta,z,t)\right]^2 \\ &= c_{2m}\vec{U}_{2m} + c_{-2m}\vec{U}_{-2m}\exp(i2\delta) + c_0\vec{U}_m\vec{U}_{-m}\exp(i\delta)\end{aligned} \tag{3.11}$$

where the coefficients of the three generated modes, c_{2m}, c_{-2m}, and c_0 are based on different phase-matching conditions for different modes. Here we use the theory presented in [65] to compute the coefficients for three modes. For m=1, the doubled output creates the combination of U_{+2}, U_{-2} and a radial mode U_0 which is given by the third term in Eq. 3.11. Each mode has coefficients 0.52, 0.52 and -0.68 for c_{2m}, c_{-2m} and c_0 respectively and are

compared with experimental results in Figure 3.3.2. Here it can be seen that a change in δ produces a rotation of the interference intensity patterns as a result of the combined OAM wavefronts.

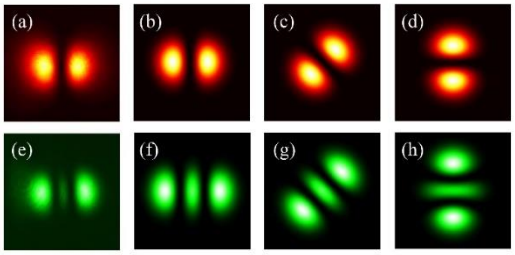

Figure 3.3.2. (a) Experimental pump intensity profile with m = 1 and simulated pump beam profiles for (b) $\varphi = 0$ (c) $\varphi = \pi/2$ and (d) $\varphi = \pi$. (e) Experimental frequency doubled intensity profile and simulated intensity profiles for (f) $\varphi = 0$ (g) $\varphi = \pi/2$ and (h) $\varphi = \pi$.

As can be seen in Figure 3.3.2 and equation 3.4, any change in δ produces an apparent rotation of the interference fringes but does not impact the amplitude of the fields, as there is no magnitude term that has δ dependence. Therefore, a change in δ will produce a beam with a constant total power regardless of the phase modulation δ applied. This allows the use of the frequency doubling system, otherwise any amplitude modulation would become distorted in the nonlinear process.

i. Geometrical Transformation System

Another method of generating CCOAM states is through a series of geometrical transformations, though the concept of creating and controlling coherent combinations of OAM beams is the same. A fiber-to-free space interferometer is built with a 1x2 fiber splitter, the outputs of this are each attached to a fiber-coupled phase modulator. The outputs

after the phase modulators are collimated and propagated through the HOBBIT system. The HOBBIT utilizes a series of optical transformations to generate OAM states [32, 66]. The setup consists of two coherent 1064 nm beams collimated and transmitted through the HOBBIT system as illustrated in Figure 3.3.3:

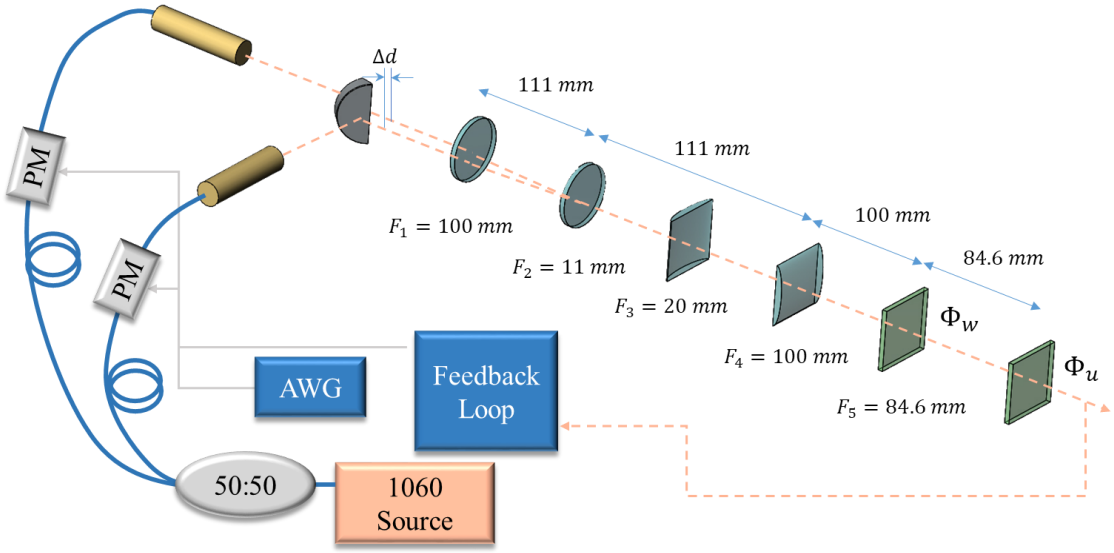

Figure 3.3.3 Schematic for HOBBIT design 1. F_1 and F_2 are the focal lengths of two spherical lenses, F_3 and F_4 are the focal lengths of two cylindrical lenses oriented in the x- and y- directions respectfully, and Φ_w and Φ_u are the two log polar optics with built-in lens function with focal length F_5.

The system above transforms two physical displacements of input beams into a corresponding higher-order Bessel beams of charge $\pm m$. The input to the HOBBIT design is a 1064 nm laser split using a 1:2 fiber splitter. A fiber coupled electro-optic phase modulator is placed along each path. By using D-shaped mirrors, as shown in Figure 3.3.3 two input beams can be sent through the HOBBIT system.

The first four lenses are used to generate an elliptical Gaussian beam, taking the input beam with a 0.5 mm diameter and converting it to a 0.5 mm by 2.5 mm distribution in the x- and y- axis respectively. This beam is then transmitted to a series of two optics, Φ_w and $\Phi_{u,}$ which perform a log-polar transformation, wrapping the elliptical Gaussian into an asymmetric ring. For more information on the log-polar transform, see [42, 66, 32] and Appendix C. To produce a charge *m* beam, the an input beam to the system shown in Figure 3.3.3 must be displaced along the y-axis off the center of the first lens by a specific amount, Δd in order to produce the desired linear phase gradient. This displacement is calculated using the lens focal lengths and the design parameters of the log-polar transformation optics:

$$\Delta d = \frac{m\lambda F_4}{2\pi a}\frac{F_2}{F_1} \tag{3.12}$$

where F_4 is the focal length of the Fourier lens (100 mm given in Fig. 3.4.1) and $2\pi a$ = 3.6 mm and is a design parameter of the log-polar optics. Note that in this system *m* does not have to be an integer value.

The ideal near-field expression for a linearly polarized beam at the output of this system can then be written as

$$U_m(r,\theta,z,t) = \hat{y}A_m(r,\theta)\exp(-im\theta), \tag{3.13}$$

where *r* and θ are polar coordinates and the ideal case of $A(r,\theta)$ for the HOBBIT system is identical for all modes and is defined by [32]:

$$A_m(r,\theta,z,t) = \exp\left(-\frac{(r-r_0)^2}{w_{ring}{}^2} - \frac{\theta^2}{\beta^2\pi^2}\right)\exp(i2\pi f_0 t)\exp(-ik_z z), \tag{3.14}$$

where r_0 is the ring radius, w_{ring} is the ring half-width, β=0.694 is the near-field asymmetry defined by the ratio of the elliptical Gaussian line length to the log-polar design parameter $2\pi a$, and k_z is the longitudinal wavenumber. In reality, $\vec{U}_m(r,\theta,z,t)$ is distorted due to paraxial limitations of the system but the exploration of this phenomena is not within the scope of this work.

For a CCOAM combination of two conjugate states where $m_2 = -m_1$, ρ=1, and χ=π/2 becomes

$$U_m(r,\theta,z,t)+U_{-m}(r,\theta,z,t)=\hat{y}\frac{1}{\sqrt{2}}A_m(r,\theta)\left[\exp(-im\theta)+\exp(im\theta)\exp(i\delta)\right] \tag{3.15}$$

where δ is the phase delay of the second mode relative to the first. The OAM terms in equation 3.15 can be simplified as

$$\vec{U}_m(r,\theta,z,t)+\vec{U}_{-m}(r,\theta,z,t)=\hat{y}2A_m(r,\theta)\cos\left(m\left(\theta-\frac{\delta}{2m}\right)\right)\exp\left(i\frac{\delta}{2}\right) \tag{3.16}$$

which generally the same result from the previous section so that the intensity profile has the distribution

$$\left|\vec{U}_m(r,\theta,z,t)+\vec{U}_{-m}(r,\theta,z,t)\right|^2=4\left|A_m(r,\theta)\right|^2\cos^2\left(m\left(\theta-\frac{\delta}{2m}\right)\right) \tag{3.17}$$

where again, we can see that changes in δ produce a rotation of the azimuthally distributed interference fringes according to the cosine term as can be seen in Figure 3.1.1 (b, c).

ii. Phase drift

In this work, interferometry is used to coherently combine and manipulate beam structure. This typically requires a source beam with a coherence length that well exceeds any path length differences. The source beam is then split into multiple copies. For the sake

of simplicity this work will describe a system that uses two coherent legs, such as a Mach-Zehnder Interferometer. Depending on the application, there are several methods of creating coherent copies including non-polarizing beamsplitters, one-to-many fiber couplers, and diffractive gratings. Each of these devices spatially separate the coherent copies. This is so that optical elements can be placed along the paths before they are then combined using similar techniques. Because the beams travel along different paths, the resulting interference patterns are highly sensitive to slight differences in path length that can be caused by environmental factors such as temperature fluctuations, vibrations, or even gravitational waves in some cases. Small phase differences on the order of the optical wavelength are all that is required. Keep in mind, for these applications we are using visible and infrared wavelengths which are on the order of hundreds to thousands of nanometers. In the systems above, laboratory environmental fluctuations such as air drafts produce phase changes on the order of π radians/second but can be faster during abnormal strain such as when a research assistant jumps nearby or bangs on the optical table. While laying optical fiber is a common sensing technique, such as in gyroscopes or strain measurements, it does require an invasive form of measurement where the fiber must be applied to the area. We are more interested in preventing these fluctuations from altering our transmitted signal so that we can probe the environments using a non-invasive method.

The slight changes in optical path length produces uncertainty in the system which adds an additional term to the output mode. This means that there is actually a phase term δ_{drift} applied to the system in addition to the desired controlled phase $\delta_{applied}$ so that the total relative phase of the system $\delta=\delta_{applied}+\delta_{drift}$. This makes the output mode unpredictable

because of the random drift term. This is not an issue in the communications setup presented in section 3.4, because we are mapping to the full HOPES and can detect a relative phase between the symbols. If instead we wish to minimize splitting of the signal, such as is desirable in the highly absorbing underwater environment, we may wish to recover the signal with as few measurements as possible.

It is possible to use a single detector to maximize detector power. For equally balanced modes, the recovered phase modulation is approximately given by $P_a \propto 1+\cos(\delta)$. The inverse cosine can be used to recover $\delta_{applied}$, but only for $\delta \in [0, \pi]$ meaning that the applied phase modulation $\delta_{applied}$ cannot exceed π, and the drift term δ_{drift} must not make the total relative phase δ exceed the bounds otherwise the signal will not be fully recoverable. A feedback loop is one solution to control δ_{drift} so that a single detector can be used at the receiver.

As presented in section 3.4, we can measure the drift using equivalent Stokes parameters to map the spatial structure to a HOPES. We can then use a feedback loop to control a phase modulator placed on the other coherent line to compensate for the drift term and lock the beam to the desired output. Using a detection setup similar to the ones found in [39, 40], two optical correlations can be used to map the state to the HOPES and recover the phase drift because we know that the state lies on the equator of the sphere.

For phase-only recovery, only two measurements are necessary because we know that the CCOAM mode we are sending does not have amplitude modulation and will lie on the equator of the HOPES because $\chi = \pi/2$. The two necessary correlations for a CCOAM state comprised of conjugate charge numbers require phase optics given by Φ_a and Φ_b which

are identical except Φ_b has a rotation angle of $\pi/(4m)$. For more information on full HOPS eqivalent amplitude control see [39, 40].

Recovery of the phase-locked signal shows a root-mean-squared phase error of less than λ/46 for 1 second worth of data, collected every minute for five minutes. When modulation is added, the recovery needs to be timed such that the feedback loop is inactive when data is sent and periodically checks the phase using a reference signal. This can be achieved using a reference signal to activate and deactivate the Arduino output. Further details on the phase-locking loop algorithm are given in appendix D.

iii. Experimental Results

The signals are collected after transmission through a 6-meter (double-pass) and 3-meter (single-pass) turbid underwater environment respectively, whose attenuation coefficient was varied by adding an aluminum hydroxide, magnesium hydroxide and simethicone solution. Recall that the optical signal is attenuated exponentially according to Beer's law. Before propagation through the water channel, the input signal power was approximately 600 mW.

After transmission through the water channel, the phase modulated signal is collected using a single optical correlator as the phase demodulator. The phase match optic is designed to correlate with the phase of $U_{+2}+U_{-2}$ where $\delta=0$. The electrical signal is then exported to a computer for processing.

First, we want to measure the beam quality after propagation through a highly turbid environment. A single sinusoidal signal of 1 GHz was applied to the transmitter to apply a phase modulation index of approximately 0.45π and sent though the 6-meter (double-pass)

water channel. This signal was sent through a double pass of the 3m channel and recovered using the receiver setup shown in Figure 3.3.4. The spectral power was measured at the receiver using a Menlo Systems APD 210 as well as the total power into the receiver. Both measurements are shown in Figure 3.3.5. The attenuation coefficient is estimated based on the amount of scattering agent added.

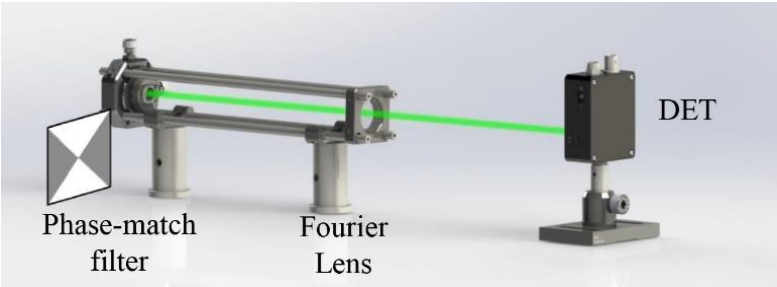

Figure 3.3.4. Receiver schematic showing phase match filter for two CCOAM beams with |m|=2 with correlation incident on the detector DET

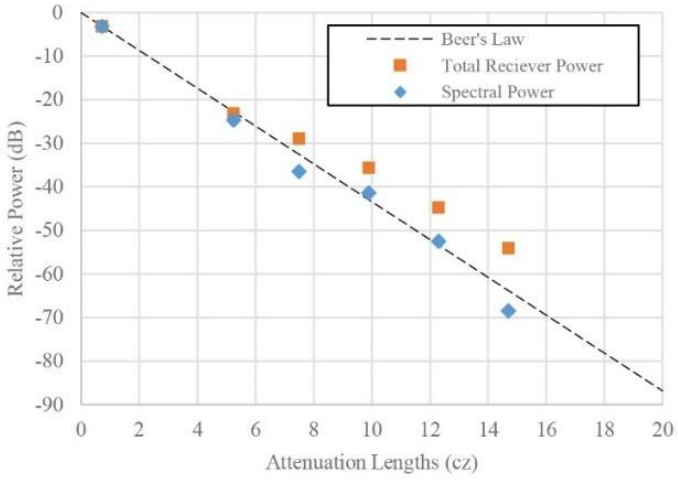

Figure 3.3.5. Sinusoid signal recovered after propagation through 6m turbid water showing Beer's law for estimating ballistic signal power, total power entering the receiver and the measured 1 GHz signal power received.

The total receiver power shown in Figure 3.3.5 follows the prediction given by Beer's Law from Eq. 1.1 up to around 6 attenuation lengths then curves up above the prediction, though not by much. This indicates that the receiver is collecting both ballistic and scattered light but because this setup uses a double pass, much of the forward scattered light is lost at the retroreflector. The correlator power follows more closely to Beer's law as is expected due to the ability of the optical correlator to filter out any light that does not correlate with the match-filter, essentially functioning as a method of narrowing the receiver field of view by pushing scattered light out of the field of view of the detector.

As shown in previous works [16, 67], amplitude modulation of a signal degrades at high modulation rates due to a wide field of view accepting multiply-scattered photons. This is analogous to acoustic latency at the receiver but is more commonly referred to spatial and temporal dispersion in free-space optical links. This effect becomes more severe as turbidity increases. The receiver has a narrow field of view and therefore turbidity primarily attenuates optical signals. This is as expected due to our previous work examining the propagation of structured light modes through scattering underwater environments [18]. Expanding the field of view would decrease the signal-to-noise ratio of the system due to the optical correlator, but would increase the power collected at the receiver. A sinusoidal signal was transmitted through highly turbid conditions, verifying successful transmission and recovery of a 1 GHz modulated signal through extreme environments.

Next, we want to demonstrate phase control using a more complex waveform to transmit information. Orthogonal frequency division multiplexing (OFDM) uses a summation of orthogonal frequencies to increase the data throughput of an otherwise limited

system. Typically, OFDM signals do not respond well to nonlinear transformation, such as second-harmonic generation or amplification, due to a high peak-to-average power ratio (PAPR). By using phase modulation to apply the OFDM signal, the total signal power remain constant, creating an ideal PAPR = 1. A modulated signal containing random information was transmitted through the 3-meter (single pass) water channel using the phase modulation of the CCOAM beams. The chosen modulation scheme is an OFDM signal carrying 16-QAM data symbols. The OFDM signal used in this work employed 192 data carriers and 8 pilot carriers with a subcarrier spacing of 5 MHz, a central frequency of 1 GHz, and a 25% cyclic prefix for a data rate of 3.072 Gbps. The signal is generated using a Tektronix AWG5028. Approximately 0.9x of the half-wave voltage is applied to the high-speed phase modulator. The output modes have a constant amplitude due to the radial symmetry of the two interfering modes, producing a constant envelope (CE)-OFDM signal. For more details on the OFDM and CE-OFDM modulation signals see appendix E.

The optical power collected by the high-speed PIN detector is then amplified by approximately 29 dB and transmitted to a Tektronix oscilloscope where the OFDM signal was recovered using SignalVu™ demonstrating successful recovery of a CE-OFDM signal applied onto the phase of coherent OAM modes. In this setup, a 400 mm lens is used to perform the Fourier-transform. The active area of the UPD is 100 μm, so a 25.4 mm imaging lens is then used to image and magnify the correlation plane by 40x for a correlation spot diameter of 200 μm.

As mentioned above, the optical correlation of the receiver helps to narrow the field of view of the detector. The active area of the detector is 100 μm, so a 25.4 mm imaging

lens is then used to image the correlation plane onto the PIN detector with a magnification of 40x, in order to enlarge the correlation spot to 200 μm, which is filtered out from the rest of the beam by the PIN aperture. This allows for the collection of primarily the on-axis photons, which will consist of photons that matched the optic.

The power collected by the high-speed PIN detector is then amplified approximately 29 dB and transmitted to a DPO73304DX Tektronix oscilloscope where the 16-QAM CE-OFDM signal is recovered using SignalVu, and the results are shown in Figure 3.3.6 for different underwater attenuation coefficients, showing successful signal recovery through 3 m of typical oceanic conditions according to Table 1.2.1. The first point on the plot shows the recovered results for clear deionized water. In this case, there are minimal particulates and we predict that refractive index fluctuations dominate over the scattering effects present in the subsequent data points.

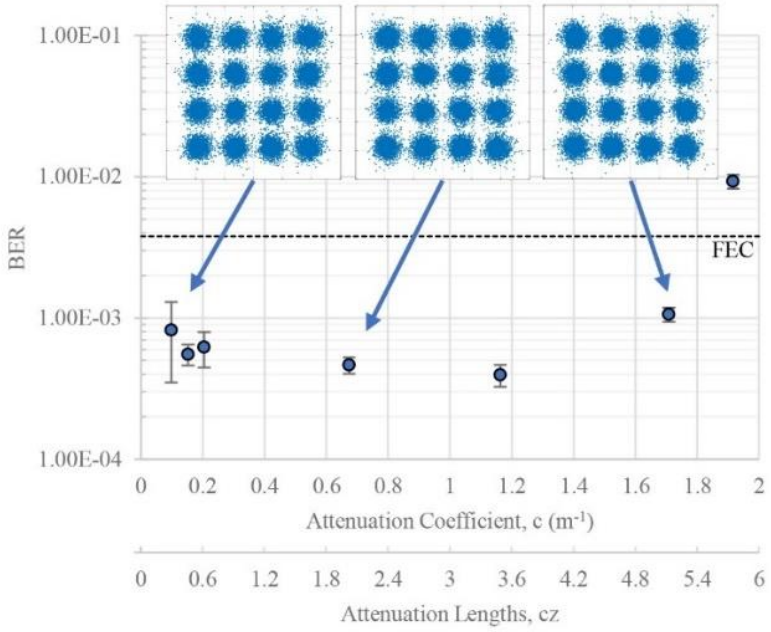

Figure 3.3.6. BER measured through varying degrees of turbid water with equivalent marine conditions indicated with z = 3 m.

From Figure 3.3.5 it is clear that a signal can be successfully recovered well beyond the turbid harbor conditions. The last datapoint in Figure 3.3.6 is below the FEC limit due to photon conversion limitations of the high-speed PIN detector and we believe that with a more sensitive detector, we could explore CE-OFDM modulation in the multiple scattering regime.

In this work, we exploit the radial symmetry and helical phase of OAM modes to create a constant-power dynamic spatial mode. We demonstrate the CE-OFDM using phase modulation of CCOAM beams to produce a 3.07 Gbps underwater free-space optical link with a bandwidth of 1.5 GHz, for a system with This system has a spectral efficiency of $\eta \leq$ 2.048. The modes are generated at 1064 nm and frequency doubled to produce modes at

532 nm that can be spatially and temporally controlled at high speed, which will be explained in further detail below.

3.4. Summary

In this chapter we demonstrate the first successful transmission of high speed amplitude and phase modulation using CCOAM beams at rates of 1 GHz. Using 1550 nm light we are able to demonstrate a proof of concept that could be translated to the blue/green region using different optical components. Control of both the total power levels, ratio of the two states, and relative phase of the CCOAM modes are demonstrated and analyzed. Next we demonstrated the first propagation of these modes through underwater turbid environments. To translate the system to work for in a WUO link, phase only modulation was necessary to get the power levels required to transmit through 3 m of turbid water. This was due to the nonlinear process of generating the green wavelengths. CE-OFDM is a modulation scheme commonly used to circumvent nonlinear processes in communications links because it has a constant amplitude. In addition, OFDM allows us to increase the data capacity of the link using signal processing techniques.

Phase modulation is demonstrated in an underwater turbid environment using frequency doubling. Frequency doubling the 1064 nm mode to 532 nm enables power-scalability at visible wavelength so that absorption in the underwater environment is minimized. In addition, the amplification allows for high speed phase modulation, and presents an interesting output mode that can still be recovered with a simple phase-only optical correlation. In this proof-of-concept work, modulation rates are limited by the available electrical components and 10 GHz modulation rates have been demonstrated in

underwater environments [25] and phase modulators are available with bandwidth of 40 GHz.

Three modulation schemes were demonstrated. First, a spatial QAM equivalent communications system was demonstrated using both amplitude and phase modulation. Second, a sinusoidal signal was applied as phase modulation only to verify successful transmission in the multiple scattering regime. This is a result of the correlation filter successfully filtering out the scattered light by directing it outside the field of view of the detector. Second, a data-carrying OFDM signal was demonstrated. Modulation of the signal occurred before two nonlinear components, an optical amplifier and a PPLN crystal demonstrating the capability of using phase modulation in nonlinear systems. Successful transmission is shown with bit error ratios (BER) below the FEC, excepting the data point close to turbid harbor conditions due to low signal power. At this highest turbidity the peak optical power incident on the detector produces a voltage signal that is on the order of the noise of the scope and does not demonstrate a degradation of optical coherence.

As mentioned in section 3.5 there is a phase drift in these interferometric systems that adds a degree of randomness, but with proper monitoring this can be compensated for. The monitoring technique requires at least two optical correlations to recover the phase information, and are designed for a specific mode. For systems of CCOAM combinations of more than two beams, alternative techniques need to be explored for efficiency and practicality, especially when transmitting through harsh environments where signal power can be rapidly attenuated by scattering particulates or water absorption.

In this work we have presented a demonstration of both amplitude and phase control of the CCOAM beams using a variety of modulation schemes chosen to increase the data capacity of the link. Phase and amplitude modulation was presented at 1 Gbaud, but components are available with higher modulation rates. We found that switching to an underwater link required system changes due to the photon-limiting environment including switching to a HOBBIT generation system to minimize losses, using a phase-only modulation scheme, and using a single detector at the receiver. Because of these changes, the random phase drift caused by the interferometry setup, required a phase-locking feedback loop to be built so that the single receiver could function optimally. In the next chapter we will examine how to obviate the fiber-to-free space interferometry setup and remove the random phase drift.

CHAPTER FOUR

TUNEABLE DYNAMIC STRUCTURED LIGHT USING ACOUSO-OPTICAL CELL

4.1. Introduction

As mentioned in the previous chapter, the HOBBIT system can be used to efficiently generate beams with OAM. It uses a set of optical elements to perform a geometrical transformation of Cartesian coordinates into log-polar coordinates. This transformation is performed on an elliptical Gaussian beam which is then wrapped to a ring. A tilt is applied to the wavefront using a physical displacement of the input beam by exploiting the Fourier transformation property of lenses. In the previous chapter we developed a method of creating the CCOAM states using fiber-to-free space interferometric techniques and ended up discovering a random phase drift due to environmental factors altering the optical path lengths for each interferometry leg.

Interferometry is not the only method of generating coherent tilted planar wavefronts. Acousto-optic cells have been long employed to rapidly and efficiently deflect optical signals and have even been employed in high-power systems [68], pulsed systems [69], and q-switched lasers [70, 71]. In our previous work, we used the HOBBIT system combined with an acousto-optic deflector (AOD) to probe a turbulent environment with an OAM chirp using a bucket detector to characterize the channel [46]. Unfortunately, AOD cannot reach the control speeds of the lithium niobate amplitude and phase modulators presented in the previous chapter because they are fundamentally limited by the acoustic

velocity of the traveling wave, therefore this system might be better applicable for sensing/imaging applications.

In addition to creating WUO communication links, one of our primary interests is utilizing these structured modes to probe turbid and turbulent environments. To do this, we need the ability to send out and recover a vast number of structured wavefronts that greatly exceed the environmental rate-of-change in order to extract information about the environment. The AOD is an attractive alternative to the amplitude and phase modulators because it has switching speeds that well exceed the rate-of-change of the environment. In addition, as we will show below, the AOD will provide much more precise control of the amplitude and phase of the CCOAM states than was previously achievable with the amplitude and phase modulators presented in chapter 3.

Imaging and controlling the interference pattern of multiple output modes does present an issue because the AOD adds a Doppler shift to the output modes as a result of the traveling acoustic wave. When creating multiple output modes with the AOD, each mode has a different optical frequency and produces a modulating interference pattern [72]. This is problematic only when the receiver sampling rate is slower than the pattern's rate of change and will be described in further detail in the following section.

4.2. Optical Doppler shift due to traveling acoustic wave

A single-tone sinusoid can be applied to the AOD to generate a specific OAM mode. The corresponding linearly polarized electromagnetic wave carrying OAM and propagating along the z-direction can be represented by

$$\vec{U}_m(r,\theta,z,t) = \hat{y}A_m(r,\theta,z)S(t)\exp(i2\pi\nu_0 t)\exp(-ik_m z)\exp(-im\theta) \tag{4.1}$$

where $A(r,\theta,z)$ is the amplitude function and is defined in equation 3.14, $\nu_0 = c/\lambda_0$ is the optical frequency of the input beam where c is the speed of light, k_m is the wavenumber, and m is the OAM charge number. $S(t)$ is the piston phase added to the wavefront as a result of the RF signal $s(t)=Re\{S(t)\}$ applied to the AO cell and is defined by

$$S(t) = \sum_{n=1}^{N} c_n \exp(i2\pi f_n t + i\delta_n). \tag{4.2}$$

where $2\pi f_n$ is the frequency required to create a beam with any OAM charge within system limitations, and c_n is used to control the total power

This represents a multitoned signal with N components, where δ_n is a constant phase shift and the frequency f_m is the is the frequency required to create a first-order deflection corresponding to any desired charge m beam. An AOD with acoustic velocity V_A and applied frequency f_m produces a first order deflection with angle ξ_m equivalent to

$$\xi_m = \frac{\lambda_m f_m}{V_A M} \tag{4.3}$$

where M is the magnification factor of a telescope placed after the AOD. The optical elements are aligned to the deflection angle ξ_0. The output wavelength changes as a result of deflection through the AOD and can be computed using

$$\lambda_m = \frac{c}{\nu_0 + f_m}. \tag{4.4}$$

The wavelength and optical frequency change proportional to the applied frequency and therefore the wavenumber can be calculated using

$$k_m = \frac{2\pi \cos(\frac{\lambda_m m}{2\pi a})}{\lambda_m} \tag{4.5}$$

Therefore, in order to produce a beam with desired charge number *m*, the deflection angle needs to be equivalent to $2\pi m$ over the active region of the log-polar transformation optics. Therefore the frequency of the RF signal applied to the AOD is:

$$f_n = f_c + m(\frac{V_A}{2\pi a})M \tag{4.6}$$

where *a* is a design parameter for the log-polar transformation, and f_c is the center frequency of the AOD and corresponds to *m*=0.

From equation 4.2 we can also apply more than one tone to the AOD using a summation of sinusoids with arbitrary starting phases δ. This produces a coherent superposition of corresponding OAM charges with a Doppler effect resulting from the optical interaction with the AOD. For illustration, we will theoretically examine an *N*=2 signal traveling through the AOD. The RF signal can be defined as $s(t)=Re\{S(t)\}$:

$$s(t) = c_1 \cos(2\pi f_1 t + \delta_1) + c_2 \cos(2\pi f_2 t + \delta_2) \tag{4.7}$$

which produces a combination of two different signals, $\vec{U}_{m_1} + \vec{U}_{m_2}$. The relative phase between $\vec{U}_{m_1}$ and $\vec{U}_{m_2}$ is simply defined by the difference between the phases of each wave given in equation 4.1:

$$\begin{aligned} \Delta\phi &= \phi_2 - \phi_1 \\ &= (k_2 - k_1) z + 2\pi (f_2 - f_1) t + (\delta_2 - \delta_1) + (m_2 - m_1)\theta \end{aligned} \tag{4.8}$$

From equation 4.8 , the relative phase is easily predictable. The interference profile resulting from the OAM terms $(m_2\text{-}m_1)\theta$ and the initialization phase $(\delta_2\text{-}\delta_1)$ is constant. As mentioned above, as the signal propagates through the AOD, it experiences a Doppler shift proportional to the frequency applied to the cell, both the wavenumber and optical frequency will shift resulting in the z- and t- dependent terms in equation 4.7. The difference between wavenumbers is extremely small and is therefore negligible except when propagating extremely long distances. The most significant impact is the change in the angular frequencies, producing a relative phase proportional to the difference between f_2 and f_1 that continuously changes with time.

Depending on the specifications of the AOD, the difference in angular frequencies, $2\pi f_n$, can easily range from 100 kHz to a few MHz and is very difficult to analyze these modal combinations using traditional imaging techniques. Typically, when these beams are imaged with a camera, which typically have integration times on the order of milliseconds and frame rates on the order of 30 frames per second (fps), these changes are blurred and an average intensity profile is generally collected as shown in the frequency doubling study of HOBBIT beams [52]. Even with high speed cameras that can reach framerates above 1000 fps, the integration time is still too long to image these beams properly. This makes it essentially impossible to image the interference fringes using a continuous wave source, as illustrated in Figure 4.2.1. Here, because the interference fringes are rotating over the entire exposure, we end up seeing what appears to be the incoherent combination of the two OAM modes.

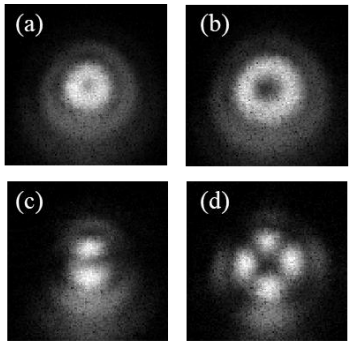

Figure 4.2.1 Illustration of pulsed beams integrated over 8 ms for (a) m=±1 and (b) m=±2 and integrated over 10 μs with a 1 ns pulse for (c) m=±1 and (d) m=±2.

Still, it is well known that the co-aligned interference patterns of beams carrying OAM produce periodic locations of constructive and destructive interference that are highly predictable based on the OAM terms [67, 39, 40] and can be seen in Figure 4.2.1 (b,c). Combining these signals with a pulsed source will enable the beam to appear frozen. The pulse will not only have to be much faster than the rate of change of the beam, but also have enough power to be imaged by the camera. This will enable the beam profile analysis by using the pulse as a strobe signal but will require precise control of the signals in time.

4.3. Continuous-wave (CW) operation

The CW HOBBIT system is designed similar to the system described in section 3.3 with some minor changes to accommodate the insertion of the AOD. The CW setup is detailed below in Figure 4.4.1 and is the same setup given in [32]. In this section, we will demonstrate the predictability and control of the CCOAM modes using the AOD.

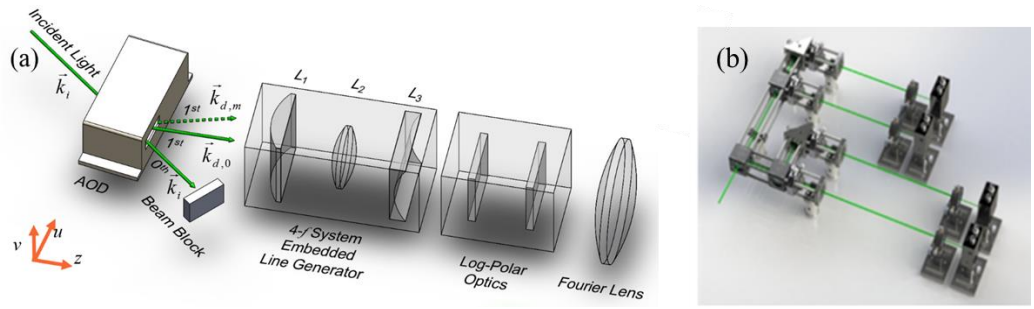

Figure 4.3.1. Setup diagram showing the (a) transmitter comprised of the AOD and the HOBBIT setup and (b) the receiver comprised of four optical correlators for mapping to the HOPES.

In order to control the amplitude and phase using the AOD, an N=2 state is created using m_1 = +2 and m_2 = -2. An electrical signal is created to match this beam using equation 4.7

$$s_K(t) = c_{1,K}\cos(2\pi f_{m1}t) + c_{2,K}\cos(2\pi f_{m2}t + \delta_K) \tag{4.9}$$

where each symbol K can have a different total amplitude, amplitude ratio, and phase, similar to the 3D constellation work presented in section 3.2. Two constellations will be used to demonstrate both 2D and 3D mapping of the CCOAM states in the HOPES space. The amplitude values given by c_n were determined by measuring the diffraction efficiency for various voltage levels through the system. The first is a 16-PSK equivalent and the second is a 512, 3D-QAM equivalent consisting of 8 levels of 8x8 symbol locations. The amplitude of the source is not manipulated by any other device besides the AOD.

For this setup, with m = ±2, f_c = 125 MHz, f_{-1} = 125.36 MHz, so that the beat frequency, f_b, is 1.44 MHz. Because we are unable to image the interference with a camera, an optical correlation was used to verify our results as is shown in Figure 4.3.2.

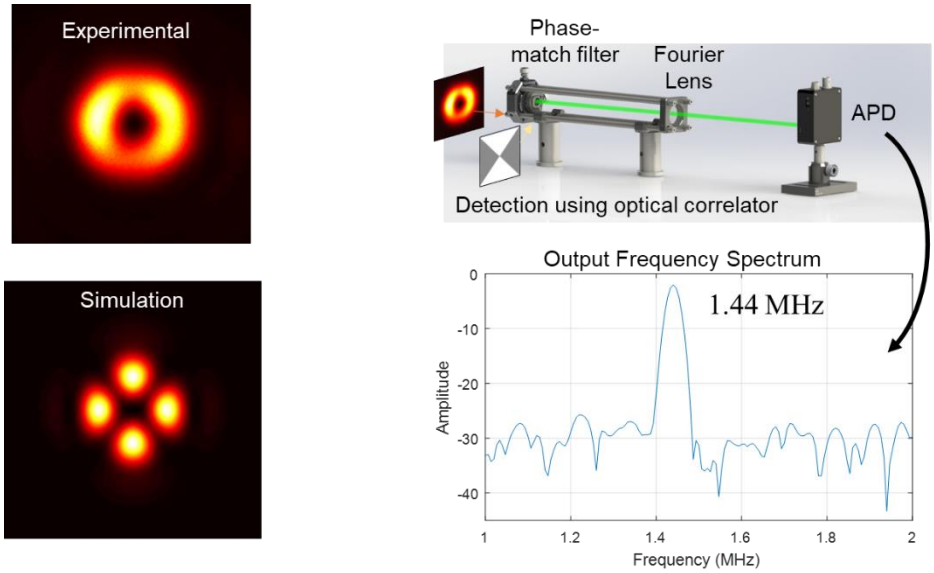

Figure 4.3.2. Illustration showing experimental vs simulated beam profiles. The simulated beam profile is instantaneous when in reality it is rotating at a rate of 1.44 MHz, which the experimental camera integrates.

The peak of the recovered spectrum matches our beat frequency, verifying rotation of the beam. Therefore, we know that with precise timing, we will be able to map and recover the CCOAM state to the HOPES space.

Experimental Results

A 532 nm (Hz) laser is sent through the HOBBIT system to generate two coherent OAM charges of $m = \pm 2$, with $f_{+2} \approx 124.28$ MHz and $f_{-2} \approx 125.72$ MHz, resulting in a theoretical rotational frequency of 1.47 MHz. The AOD crystal used operates in longitudinal mode, meaning the 1st order output has a rotated polarization. The 0th order output is blocked from transmitting through the system. Two different modulation schemes are applied to the acoustic cell to control the output beam using the method described above, a 512-QAM signal and a 16-PSK signal with a modulation rate $f_s = 1/T$ of 200 kBd. The

repetition rate of the transmitted symbols is fundamentally limited by the switching speed of the AOD, which in this case is 2.3 μs.

The output signal from the transmitter is propagated through 3.0 m of turbid water with attenuation coefficients of 0.22 m^{-1}, 0.28 m^{-1}, 0.36 m^{-1}, and 0.56 m^{-1}, measured using total beam attenuation of a 0^{th} order Bessel beam. At the receiver, the signal is split into four legs, each necessary for mapping to the HOPES as explained in the previous chapter. Each of the four signals is sampled exactly 3.0 μs after the start of the transmitted signal to allow for the rise time of the AOD. The four signals are recovered using the same technique presented in section 3.4. The recovered 512-QAM and 16-PSK constellations are shown in Figure 4.3.3 and have spectral efficiencies of $\eta \leq 4$ and $\eta \leq 9$ bits/s/Hz. Bit error ratio (BER) analysis is done by converting the symbol error ratio to bits assuming ideal gray encoding. The SNR of the signal is estimated by measuring the modulation error ratio [40]. This plot is also shown in Figure 4.3.3 along with simulated BER measurements done using a Monte-Carlo estimation assuming white Gaussian noise.

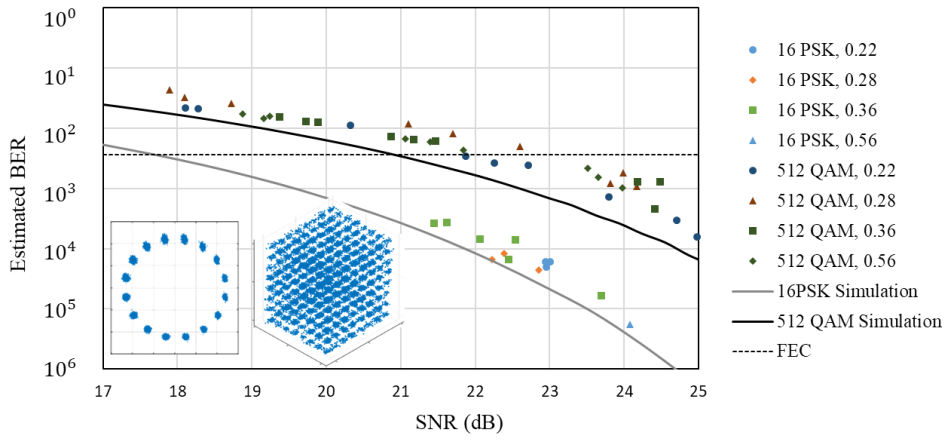

Figure 4.3.3. Figure showing BER results of three-dimensional 512-QAM constellation and two-dimensional 16-PSK constellation with attenuation coefficient indicated in m^{-1}. Each case is simulated using a Monte-Carlo algorithm. Experimentally recovered constellation plots are also shown.

Interferometer drift is eliminated in this mode generation system compared to a traditional Mach-Zehnder interferometry setup because the photons are travelling very close to the same path. Mode recovery is shown to be successful in for all turbidities, with increasing turbidity having a negligible effect on the BER of the signal as a result of SNR. Higher turbid water simply attenuates the signal, so more power is required to be sent to the receiver. This is likely due to the small field of view of the receiver, which will likely filter out any non-ballistic photons. In fact, the variance of the received BER is most likely caused by a slight misalignment of the beam into the receiver, as there were four different correlations to align.

In summary, we have demonstrated an extremely precise method of controlling the amplitude and phase of the CCOAM states using an AOD. The AOD is controlled using an

applied voltage signal whose frequency and amplitude determine the output state. Because the beat frequency of the CCOAM state is well known and constant, we are able to recover the relative states. Still this method is not perfect, if the selected charge numbers were also changed for each transmitted symbol, the beat frequency would change resulting in a different phase measurement. Therefore timing needs to be further examined, especially for future use with $N>2$. In addition, the switching speeds are not ideal for underwater communications and are more suitable for sensing and imaging applications. Therefore it would be of great interest to minimize the uncertainty of the transmitted beam, which we will do in the next section using a pulsed source

4.4. Pulsed Source Operation

In this section we will demonstrate the combination of the HOBBIT system with a pulsed source. The HOBBIT system is designed similar to that described in section 3.3 with some minor changes to accommodate the insertion of the AOD as well as a different wavelength. The setup is detailed below in Figure 4.4.1.

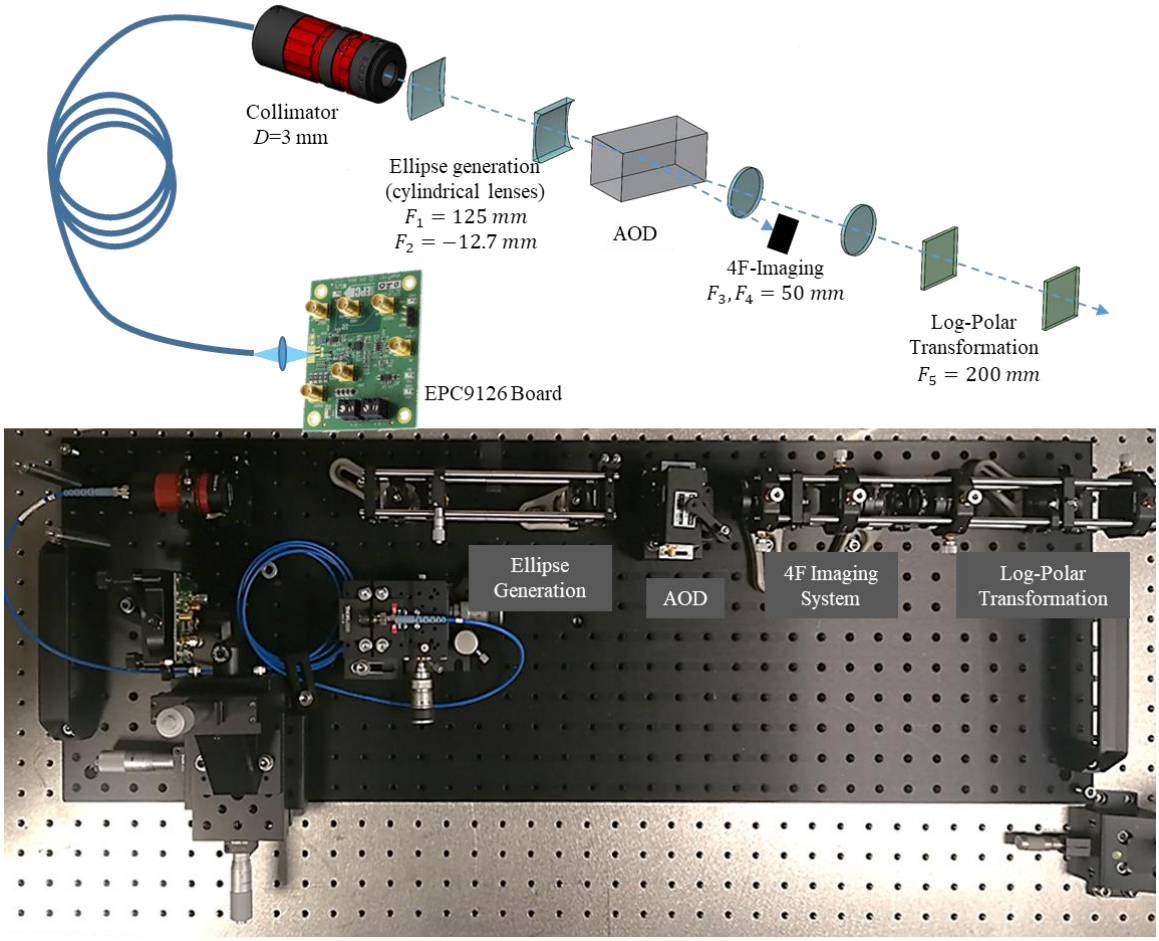

Figure 4.4.1 Schematic diagram showing fiber-coupled pulsed source, collimator, line generation lenses, acousto-optic deflector (AOD) with blocked 0^{th} order, a 4F imaging system to image the center of the AOD onto the first log-polar optic, and the set of log-polar optical elements used to wrap the ellipse into a ring.

For this HOBBIT build, a 3 mm by 0.3 mm elliptical Gaussian beam is created with a set of cylindrical lenses. This elliptical distribution is then propagated through a tellurium dioxide AOD which has a clear aperture of 10 mm by 10 mm and acoustic velocity of 0.65

mm/μs. The aperture is large, so we are able to put the elliptical Gaussian generation optics before the AOD. According to the equations in section 4.2, this reduces the beat frequency of the device. In this section, the beat frequency is on the order of kHz, where in the previous section it was on the order of MHz. In addition, the large aperture will allow us to transmit a larger beam through the cell, reducing the power density and increasing the maximum output of the system before components get damaged. While this work is at a low power, we are interested in eventually transitioning to higher power applications.

The center frequency of 120 MHz was chosen to correspond to m=0. The center of the AOD is reimaged onto the first log-polar optic using a 4-F imaging system with $F_3 = F_4$ = 50 mm producing a magnification M=1. The log-polar optics have the same design parameters mentioned in section 3.4 with $2\pi a$ =3.6 mm and b = 2 mm, such that the frequency required to change one charge number is approximately 180.56 kHz when calculated using equation 4.5.

According to equation 4.7, the rate of change of the modal combinations will be on the order of 10 MHz or less, so we want to probe the signals with a pulse that is over 100x shorter than the maximum rate of change, and have chosen to create an optical pulse with a full-width-half-max (FWHM) on the order of 1 ns. For this work we chose an OSRAM PLT5 450B blue laser diode, which we mounted to an EPC9126 board. The output wavelength was measured to be 454 nm with a FWHM of approximately 1 nm. The coherence length of this diode is therefore 65.8 μm.

The pulse width was approximately 1 ns and is shown in Figure 4.4.2. For a repetition rate of 1 kHz, and a driving voltage of 18.0 V, the output has an average power

of 5 mW. Integrating over the pulse shape shown, the peak power is approximately 100 mW, with a pulse energy of approximately 200 pJ. Figure 4.4.2 also shows a tail that decays exponentially over approximately 5 μs. This is significantly longer than the pulse width and therefore precise timing is required to minimize integration on the camera over this range.

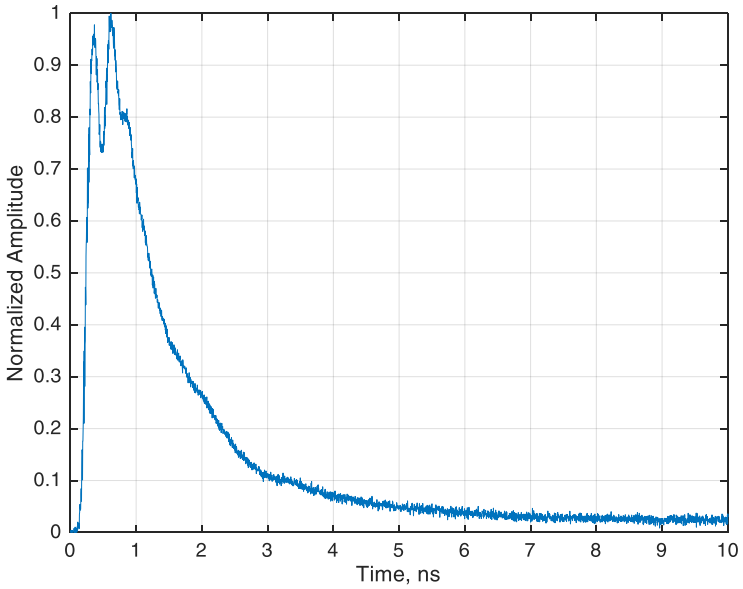

Figure 4.4.2. Optical pulse created with the EPC9126 board.

The Miro C210 high-speed camera will be used to collect images with a frame rate of 1000 fps for a 512x512-pixel area and an integration time of 10 μs and a timing accuracy of 20 ns. As mentioned above, there is a slow exponential decay that is on the order of this integration time and therefore precise timing is required not only to synchronize the camera shutter with the pulse and AOD, but is also necessary to minimize integration on the camera. A Tektronix 5208 AWG was used to control the timing of the diode pulse, AOD RF signal, and camera shutter as illustrated in Figure 4.4.3. Because of the long integration time, the timing between the pulse and the camera must be precise such that the pulse is near the end

of the 10 us window due to the tail mentioned above. This is to minimize integration of the undesired signal, which will appear as a blurring of the interference pattern due to the rotation caused by the Doppler shift.

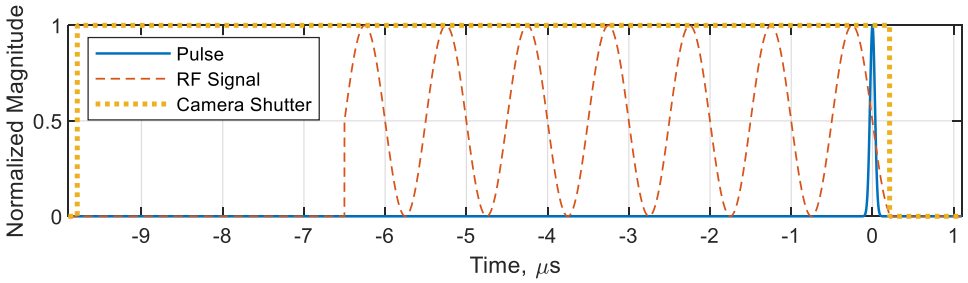

Figure 4.4.3 Timing visualization of signals with respect to pulse. Plotted pulse width and RF signal frequency are exaggerated for illustration purposes.

Figure 4.4.3 illustrates that t=0 is located at the optical pulse peak. Therefore $s(t)$ given in equation 4.7 can be modified as follows:

$$s(t)=\sum_{n=1}^{N} c_n \cos\left(2\pi f_{m_n}\left(t-t_0\right)+\delta_n\right) g(t) \tag{4.10}$$

where t_0 is greater than 6.6 μs, the rise time of the AOD and shifts sinusoid so that t=0 is aligned with the pulse, and g(t) is a rectangular envelope.

Experimental Results

In order to verify spatial and temporal alignment of the system, N=2 conjugate combinations were first examined to demonstrate interference patterns matching previous results [39, 40]. As mentioned in chapter 3, when conjugate pairs with OAM charge number $|m|$ are combined, 2m locations of complete destructive interference are formed and produce an azimuthal periodic intensity pattern. Creating an interferogram with the OSRAM 450 diode would be extremely difficult with its coherence length of approximately 66 μm,

because the optical path length differences need to be less than the coherence length in order to see interference fringes.

This is why the HOBBIT optical transformation system is so elegant: the beams travel along approximately the same optical path rather than separating as in the Mach-Zehnder interferometer in chapter 3. In fact, the only changes in optical path length that the coherent beams experience is a result of the acoustic waves traveling through the AOD and the resulting deflection. The deflection angles can be computed using equation 4.3 and are extremely small: on the order of 100 μRad. From Figure 4.4.1 we can see that the beam travels from the AOD to the first log-polar element approximately 200 mm for m=0. Theoretically the system is limited by the paraxial approximation to around m=±16 as has been shown [66]. This would correspond to an angular difference $\Delta\xi\approx$2 mRad. Through this system, the optical path length difference for the m=0 and m=16 beam would be approximately 407 nm which is still well within the coherence length of the diode.

Next we want to further examine the time-dependent term in equation 4.8. For two sinusoids, the difference in frequencies is commonly referred to as the beat frequency, $f_B=|f_{m2}-f_{m1}|$. This determines the rate of change or the rotational speed of the interference patterns. Recall from chapter 3 that phase modulation of 2π produces a rotation equivalent to π/m for conjugate modes where $m_2 = -m_1$ so that one full rotation requires 4mπ applied phase. In this case the beat frequencies become $f_{Bm}=2m(f_1-f_c)$ and therefore the angular rotation will be the same. For $|m|$=1, f_{B1} is approximately 361 kHz, well in excess of any traditional imaging system.

Therefore it is impossible to image using even a high speed camera in CW operation. By using a pulsed source, the camera is prevented from integrating over extended periods of time and we are able to see the expected patterns as shown in Figure 4.2.1.

The AOD signal period $s(t)$ is approximately 6.7 μs and it is important to determine the proper timing alignment between the optical pulse and s(t). Using equation 4.9 to create N=2 conjugate combinations with $m_2 = -m_1 = [1, 2, 3, 4]$ and $\delta_1=\delta_2=0$, timing offsets would produce different angular errors for each beam according to the table shown below, these errors correspond to the azimuthal orientation of the interference fringes. The results are aligned within ±10 ns.

Table 4.4.1. Angular error resulting from timing misalignment

Misalignment (ns)	**$\|m\|$=1**	**$\|m\|$=2**	**$\|m\|$=3**	**$\|m\|$=4**
0	0.00%	0.00%	0.00%	0.00%
1	0.36%	1.44%	3.25%	5.78%
10	1.44%	5.78%	13.00%	23.11%
20	3.61%	14.44%	33.50%	57.78%
50	5.42%	21.67%	48.75%	87.67%
100	7.22%	28.89%	65.00%	115.56%

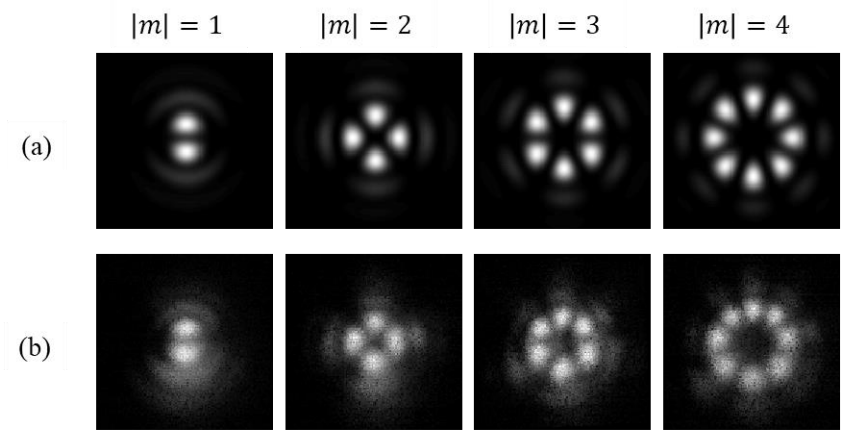

Figure 4.4.4. (a) Simulated and (b) experimental profiles for N=2 beams with $m_2 = -m_1$ and $\delta_1=\delta_2=0$.

The collected images have the correct orientation and interference fringes but are slightly blurred which is most likely caused by integration on the camera. As mentioned above, there is a 5 μs tail that will be integrated unless the camera shutter is timed properly. Wavefront recovery is now possible where previously we needed to perform several optical correlations [39, 40]. In addition to controlling the combination of OAM states, we can control the relative phase between the two beams using the phase shift term given in equation 4.9. For a signal with N=2, Figure 4.4.5 and Figure 4.4.6 shows phase control and the apparent rotation of the interference fringes compared with the ideal case. The orientation was calculated using image registration to track the bright lobes.

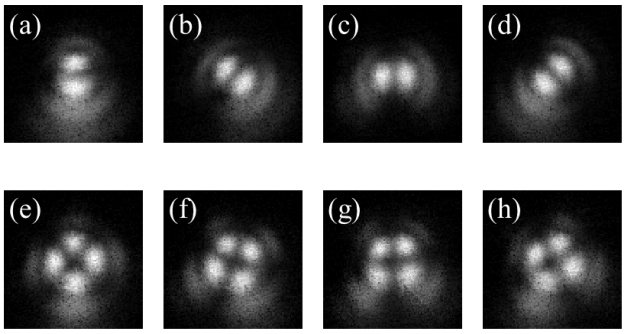

Figure 4.4.5 Experimental intensity profiles for m_1=+1, m_2=-1,and δ_1=0, and (a) δ_2=0, (b) δ_2=π/2, (c) δ_2=π, (d) δ_2=3π/2 and m_1=+2, m_2=-2,and δ_1=0, and (a) δ_2=0, (b) δ_2=π/2, (c) δ_2=π, and (d) δ_2=3π/2.

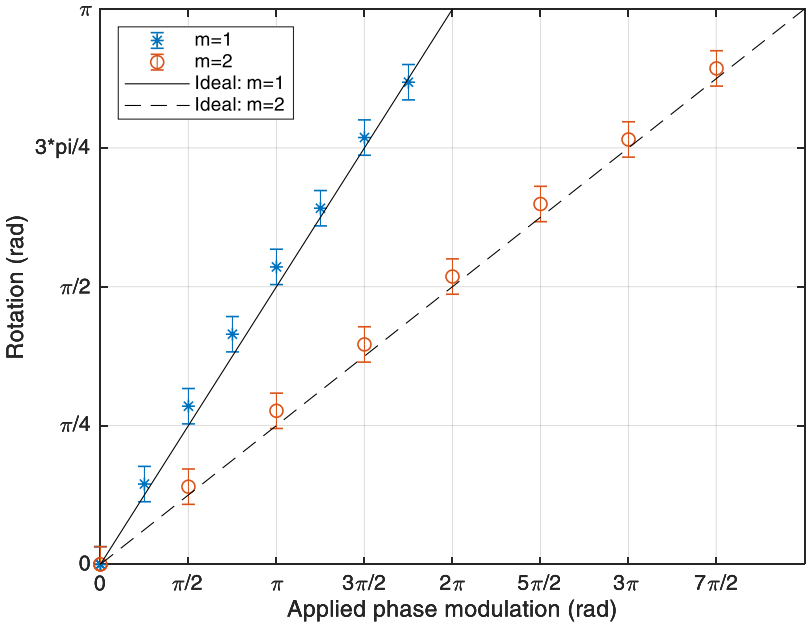

Figure 4.4.6. Measured angular rotation relative to the starting condition with δ_1=0, and δ_2 given by the x-axis.

Now that we are able to image the interference patterns, this opens up the possibility for wavefront recovery using interferometric techniques. Direct phase measurement interferometry (DPMI) can be employed using the 0th order HOBBIT beam as a reference

signal. For further details, see appendix G. By combining the 0^{th} order HOBBIT beam with a charge m HOBBIT beam we can recover the wavefront relative to the reference beam. This was done with m_2 ranging from -2 to +2 in increments of 0.25. The relative phase is set according to the equations given in the appendix. The phase of the reference beam δ_1=0 is held constant while the phase of the second beam δ_2 is set to [0, π/2, π, 3π/2] corresponding to interference intensity profiles I_1, I_2, I_3, and I_4. Ten frames of each interference pattern were collected in addition to the single *m*-beam. Using the four interference patterns, we are able to compute the wavefront relative to the reference beam using basic trigonometry

$$\phi(x,y) = \tan^{-1}\left(\frac{I_4(x,y) - I_2(x,y)}{I_1(x,y) - I_3(x,y)}\right) \tag{4.11}$$

Simulated results are shown in Figure 4.4.7 and experimental results are shown in Figure 4.4.8. Simulations are done using a numerical propagation of the HOBBIT nearfield output approximation given in chapter 3. Numerical propagation is done using the Rayleigh-Sommerfeld propagation kernel given in [5].

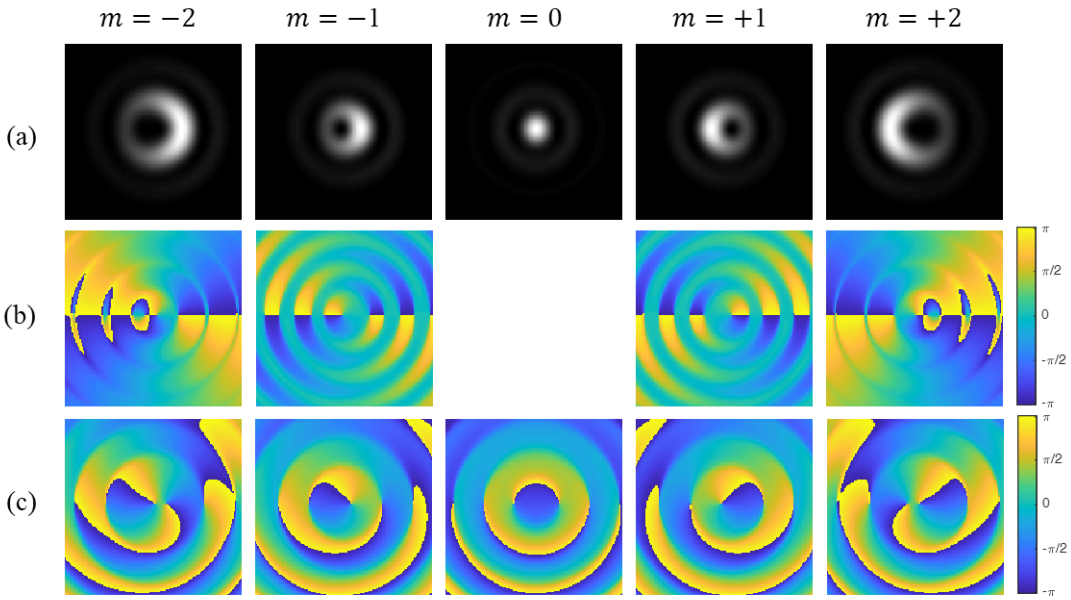

Figure 4.4.7. (a) Simulated intensity profiles for N=1 beams created using HOBBIT system with the wavefronts shown using (b) DPMI, and (c) the simulated wavefront.

Examining Figure 4.4.7 (c), we can see that the wavefront of the reference beam m=0 is not planar. This results in the recovered wavefronts shown in Figure 4.4.7 (b) and Figure 4.4.8 (b) having an actual wavefront computed using

$$\phi_m(x,y) = \phi_0(x,y) - \phi(x,y) \tag{4.12}$$

where ϕ_m is the actual wavefront of the OAM beam, and ϕ_0 is the wavefront of the reference beam.

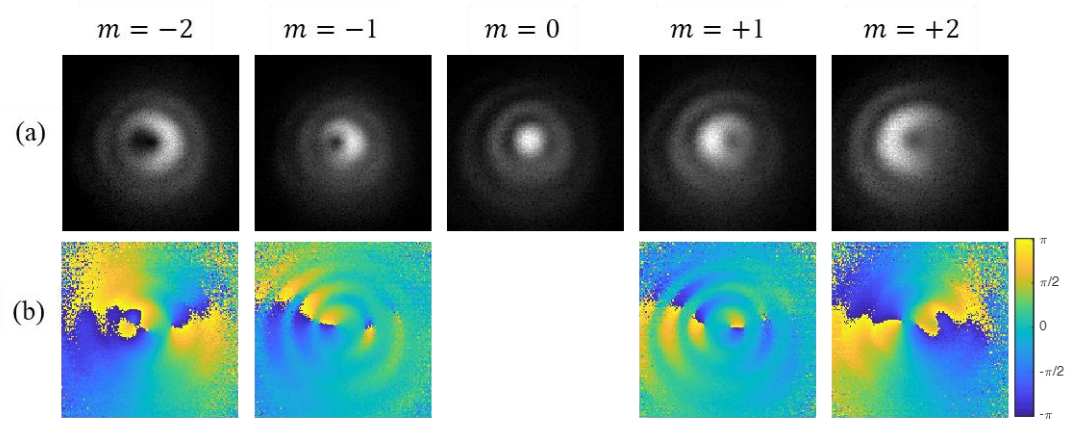

Figure 4.4.8. (a) Experimentally collected intensity profiles for N=1 beams created using HOBBIT system (b) experimentally recovered wavefronts $\phi(x,y)$ collected using DPMI

Using the recovered wavefront we can estimate the total OAM of the beam. Using the technique presented in [73], the total OAM charge was computed using the intensity and phase information. The resulting total OAM measurement is shown in Figure 4.4.9.

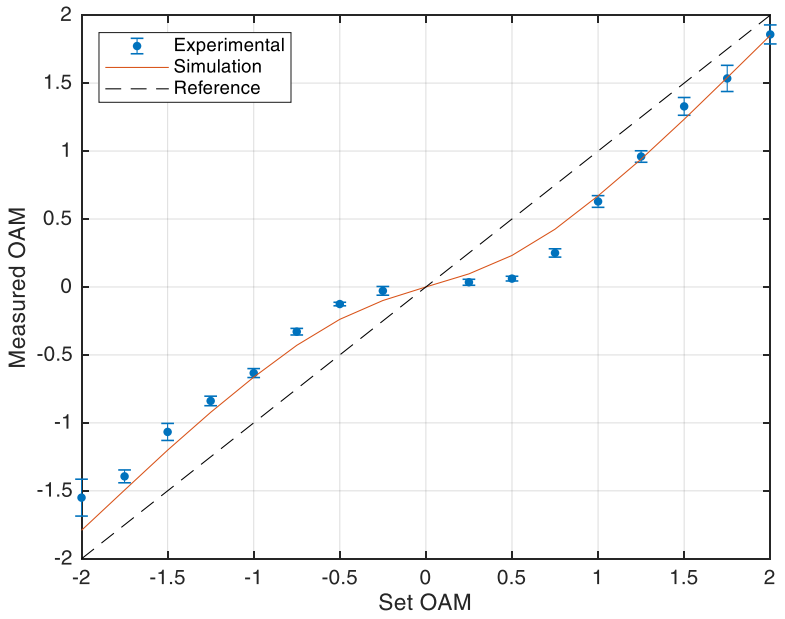

Figure 4.4.9. Recovered OAM using DMPI wavefront combined with the intensity profile.

The simulation total OAM was recovered using DPMI to compare with the experimental results. There is a distortion about m=0 and offset of the total OAM that has good agreement with the simulated OAM measurement. The reference line in figure 4.5.5 shows the recovered OAM using the true simulated wavefront, which is computed using a Rayleigh-Sommerfeld propagation kernel.

4.5. Summary

Previous implementations of the HOBBIT system have used CW laser sources, where an inherent Doppler shift can corrupt the beam if a detector is unable to precisely sample above the beat frequency of the combined modes. By properly sampling the signal in time, we can circumvent this issue, but this does not address the overarching issue of a

continuously modulating beam and demonstrate a link with very good spectral efficiency of $\eta \leq 9$. This will become particularly apparent when trying to create combinations of more than one beam due to multiple changing beat frequencies.

Instead, by combining the system with a pulsed source, this system is able to circumvent this issue while simultaneously providing precise amplitude and phase control of the CCOAM states. In addition, by using the pulsed source to collect images of interference patterns, we are now able to use the system to self-reference and successfully recover the approximate wavefront of the generated modes, which we had previously verified using multiple optical correlations. By using a pulsed source, we are able to study the beam profile at precise moments in time using a simple setup that only requires a camera and a Fourier lens in addition to the AOD-HOBBIT build.

Pulsed sources have several applications in nonlinear optics and machining, such as filament generation and control, environmental probing, and single photon sources. All cases where precise control can be key. Still, it important to note that the pulse width must be much shorter than the beat frequencies of the applied RF signal which are determined by the specifications of the AOD. Depending on the application, it may be desirable to utilize an AOD with a slower acoustic velocity, which from equation 4.6 produces a smaller change in required frequencies. On the other hand, with access to ultrashort pulses, a faster acousto-optic velocity may be acceptable. In addition, it would be interesting to explore alternative degrees of AOD control so that both the longitudinal and transverse wavevectors can be manipulated. This may enable the precise control and study of these beams along the axis of propagation in addition to the spatial control presented herein.

CHAPTER FIVE

CONCLUSION AND FUTURE WORK

This work, driven by desired for increased data capacity in the underwater and maritime environments, structured light modes were generated and manipulated in the visible blue/green regime. Experiments show that structured light can easily be created with CCOAM states. Not only can these states be amplitude-modulated but phase modulated as well to dynamically control the structure.

First, concentric spiral phase plates were introduced. Simulation and experimental results show that we can create CCOAM modes using a single optical element that exploits the divergence of OAM beams with propagation. This technique is important when generating interference patterns with optical sources that do not have long coherence lengths, typical of GaN blue laser diodes. Three different interference patterns were examined and propagated through a turbid underwater environment, where we found that despite propagation through extremely turbid environments similar to those found in harbors, spatial structure was extremely well maintained showing that beam quality is maintained despite the presence of scattering particulates. In addition, amplitude modulation was applied to the source to examine the modulation capabilities of such beams, demonstrating that the spatial structure of the beam seems to be more robust than the temporal coherence of the amplitude modulation signal.

Then, dynamic control was added to the structured light using interferometry. By creating coherent superpositions of co-propagating OAM states, complex wavefronts can be created and precisely controlled. Two systems are discussed: a Mach-Zehnder

interferometry system and the HOBBIT system both using frequency doubling of a 1064 nm source to create a higher power 532 source with a long coherence length so that the interferometric techniques are possible underwater. These two systems enable high-speed phase modulation that can be recovered with a very simple receiver setup. In this work, two different phase modulation schemes are presented: a 1 GHz sinusoidal signal and an OFDM signal with a 1 GHz bandwidth and 200 carrier frequencies. Both results concur with those from the previous chapter, showing that the spatial structure of the beams are maintained despite propagation through highly turbid environments and the modal information is recoverable with a phase-only optical correlation. This phase-only optical correlation is able to aid in filtering out the scattered photons, allowing the receiver to collect predominantly ballistic, non-scattered photons and can operate much faster than computational image processing techniques. Still, there are some issues present with MZI setups, namely a phase drift that occurs due to environmental factors of the two propagating signals. By adding in a second phase control term, we are able to minimize the drift and lock the desired mode. Still, the number of detectors required for the phase locked loop is dependent on the number of mode combinations and for 3+ combinations of beams, this would require a large number of beam splitters, creating undesirable power loss for systems that are already power-limited such as in the underwater environment.

Finally, a modified HOBBIT system that includes an AOD was introduced. The AOD enables a higher degree of control that the displacement system cannot achieve at high speed: we are able to tune arbitrary combinations of OAM states. The traveling wave produces a Doppler shift that produces a continuous change of intensity profile in time at

high speeds. The states are easily predicable because the Doppler shift is well defined, which was verified using a pulsed source to strobe the continuously rotating image on a high speed camera, set to integrate exactly one pulse. This imaging technique enables us to perform a self-referencing wavefront recovery method, which has potential applications in turbulence and turbidity sensing.

Overall, structured light can be used to increase the spectral efficiency of a link that is otherwise bandwidth limited. In fact, we demonstrated structured light control in air at rates of 1 GHz [40]. In addition, all the experiments presented in this work were linearly polarized monochromatic signals, meaning they could be combined with a wavelength division multiplexing system and polarization division multiplexing, not to mention orthogonal CCOAM pairs for SDM.

5.1. Future Work

In the future, applications of structured light in high power environments should be explored as well as their application in the single photon regime. The AOD is a very powerful tool that can be precisely controlled in order to attenuate optical signals, enabling single-photon power levels that would be particularly interesting to explore in combination with a pulsed source but is also robust enough to withstand high-power signals.

In addition, higher degrees of AOD control can be explored. The results presented in this work only included two-beam combinations generated with the AOD. These devices are not limited to two, but can be expanded to several-toned signals. Still, with multitoned signals there is an issue with the harmonic generation interacting with the electromagnetic wave known as inner-modulation products. These inner-modulation products reduce the

efficiency of the designed signal by deflecting a small portion of the signal along a different diffraction path. This is a problem that has commonly been studied when using acousto-optic devices and will need to be further explored before higher-order CCOAM states can be created and controlled. We also only explored single-axis deflection using the AOD. Preliminary simulation results have shown that utilizing a second axis of AOD deflection would enable control along the propagation axis in addition to the structured wavefront control presented in this work. We also demonstrated wavefront recovery through self-referencing. This may be useful to recover refractive index changes in an environment but preliminary work shows that we need to explore an initial separation of the two beams at the transmitter in order to recover this information. There are several ways that this could be achieved either by using the zeroth order output from the AOD or by using different output radiis.

Another area of exploration is the receiver setup for these CCOAM modes. Similar to how the HOBBIT system can be used in reverse as a mode sorter, the AOD-HOBBIT system could also be used in reverse to recover information about the system. One main goal of this work is to eventually use the structured light modes as a probe, gaining environmental information about a 3-dimensional environment so accurate mode recovery is crucial for determining minute changes in the transmitted beam.

Not only can the AOD-HOBBIT system be used in high-power applications but it can also be used in extremely low-power applications, such as the single photon level. The pulse presented in chapter 4 had an energy of approximately 200 pJ, while the energy of a single 454 nm photon is approximately 0.438 attojoules. While we are still approximately

eight orders of magnitude away from single photon levels, it is a rather simple change to attenuate the signal levels using the AOD or other components and would only require a single photon detector to measure and recover signals.

5.2. Major Contributions

First we explored how CCOAM states can be created and how their spatial structure is affected after propagation through extreme turbidity. We were the first to demonstrate the use of these modes in an underwater environment and that they are able to maintain modulation information. In chapter 1, we demonstrated the maintenance of the spatial structure of two incoherent superimposed OAM states. Chapter 2 demonstrated the spatial structure of static CCOAM states using image registration. The concentric phase plates provide a static framework for the CCOAM states so that we can easily study them under various conditions. Chapter 3 demonstrated the spatial structure of dynamic CCOAM states using an optical correlation whose relative power closely follows the Beer Lambert Law with increasing turbidity. The interferometry and dynamic control complicates this method but using a PLL can improve measurement accuracy.

The second fundamental question related to how we can control and manipulate the CCOAM states. In chapter 2, we have limited control because we use a single passive optical element to generate the states. In this case, we could only rrapidly control the amplitude control, demonstrated and was demonstrated using high and low signal levels. In chapter 3, fiber-to-free space interferometry is used which opened up the ability to not only control the amplitude, but the phase as well. We ended up finding that, due to the fiber present in the interferometry, there is a phase drift that must be compensated for in order to accurately

transmit the proper state if we wish to use a recovery method that minimizes photon loss. In Chapter 4, we are able to replace the fiber-to-free space interferometry system with an AOD which eliminates the random phase drift issue while providing extremely precise amplitude and phase control, but the traveling acoustic wave introduces a Doppler shift which produces a continuous but predictable modulation of the system. This AOD control is precise enough to recover wavefront information using a self-referencing interferometry technique.

Finally, the third question related to power scalability when controlling the CCOAM states. In underwater environments, optical power is rapidly lost due to absorption and scattering. Chapter 3 presented two systems. The first uses a MZI setup, which consists of a beamsplitters meaning that half the power is thrown away. This is unacceptable for high power applications. The second system uses the HOBBIT geometrical transformation system which has low losses, and the losses are well understood. For this reason, the setup is used in chapter four, where we are extremely photon starved because of the pulsed source. In the future we hope to have access to an ultrashort pulse, and the optics are all fabricated out of fused silica glass which has an extremely high damage threshold. Finally, we also demonstrate using this system as a pump signal in a second-harmonic-generation process to generate high power visible light signals in the green regime to maximize transmission underwater while maintaining phase control. This allowed the use of standard communications components to control the CCOAM states with low damage thresholds to be used because they are placed before the optical amplifier. In chapter 4, the interferometry setup is replaced with an AOD and a single pulsed source. While the source is not high-

powered, it is used to verify the feasibility of combining and aligning the system with a pulse. The AOD has a large active area, and AODs can be fabricated out of robust materials such as quartz, also known as crystalline silica which has very high damage thresholds.

As you can see, there is a wide range of future applications that can stem from this work just for the underwater environment, ranging from communications to sensing and applications. This work examined the precise amplitude and phase control needed to predict and control the output CCOAM state. By creating a predictable state that can be precisely and rapidly controlled, we are closer to the goal of combining several OAM states to remotely probe an environment.

APPENDICES

Appendix A

Optical Fabrication of Concentric Phase Plates

Three different diffractive phase plate designs are used to convert a Gaussian beam into the desired interference patterns. The concentric DPPS used in this work have a phase profile defined by equation 2.2 with r_1 = 0.625 mm and r_2 = 2.5 mm.

The phase delay, $\Delta\varphi$, experienced by a phase front traveling a distance h through a medium with refractive index n_1 can be calculated using

$$\Delta\varphi = \frac{2\pi}{\Delta h}\lambda / \left(n_1 - n_0\right) \tag{A.1}$$

where λ describes the wavelength of light and n_0 is the refractive index of the surrounding medium. The modulus 2π is taken of the phase profile, $P(\theta)$, in order to compress the optical element. Therefore, the maximum phase delay experienced by the phase front will be 2π radians. Utilizing this fact, equation A.1 can be manipulated to find the optical depth corresponding to a phase delay of 2π radians:

$$h_{2\pi} = \frac{\lambda}{n_1 - n_0} \tag{A.2}$$

The ideal height profile $h(\theta)$ of a concentric DPP is derived from equation (2.2) and is expressed as

$$h\left(\theta\right) = \begin{cases} \dfrac{m_1\lambda\theta}{\left(n_1 - n_0\right)2\pi}, & 0 < r \le 0.625\,mm \\ \dfrac{m_2\lambda\theta}{\left(n_1 - n_0\right)2\pi}, & 0.625\,mm < r < 2.5\,mm \end{cases} \tag{A.3}$$

where r gives the radius in milimeters, n_1 is the refractive index of the substrate, and n_0 gives the refractive index of the surrounding medium. For this work, $n_0 = 1$for air. The phase profile of the diffractive optics was designed by taking the modulo 2π of $h(\theta)$

This profile is then divided into 16 discrete levels, indicating four iterative etches in the fabrication process. This results in a calculated diffraction efficiency of 98.7% using equation (1). Similarly, the diffraction efficiency is 95.0% for an 8-level DPP and is 99.7% for a 32-level device. The 16-level devices, as can be seen in chapter 2, Figure 2.2.1, are chosen over the other options to balance the ease of fabrication and diffraction efficiency.

A photolithographic method is used to expose a pattern onto photosensitive resist wafer, which is then etched in an Inductively Coupled Plasma tool to transfer this profile into a fused silica. For each depth in the etching process the wafer is cleaned, coated in photoresist, exposed using an i-line projection lithography tool, developed, and plasma etched. An etch process consisting of three steps resulting in an 8-level device is illustrated in figure A-1.

For operation at 450 nm, the refractive index of fused silica is 1.466. Using equation (3), a phase delay of 2π radians occurs after propagation through approximately 960 nm of fused silica glass. This depth is divided into four etches: 60 nm, 120 nm, 240 nm, and 480 nm. The total etch depth is therefore approximately 900 nm. This is to ensure a proper phase wrapped profile. Precise etch depths and alignment of each layer is crucial, especially when designed for operation at shorter wavelengths. In this case, any small deviation may be on the same order of magnitude as the wavelength. This will result in a loss of efficiency. The

etch depth profile of the fabricated devices is given in figure A-2, where errors can result from fabrication errors, too high etch rates, or inconsistent plasma matching times.

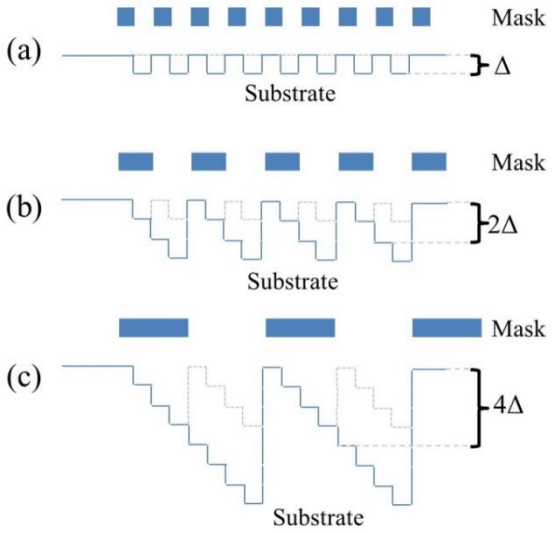

Figure A-1. Illustration of a 3-step etch process creating 8 levels, where Δ is the desired step size and is given by the total etch depth divided by the number of levels. The mask leaves a protective layer of photoresist which protects the substrate from being etched. Each subsequent layer is etched twice as deep as the previous layer for the a) first etch, b) second etch, and c) third etch.

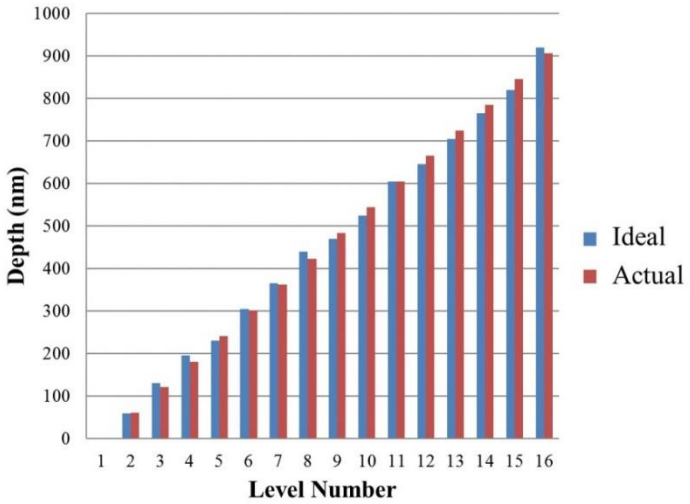

Figure A-2. The etch depths for each level of the device are compared to the ideal etch depths for a 16-level device operating at 450 nm.

Appendix B

Higher-order Poincaré Sphere (HOPS) Equivalent

CCOAM modes, when comprised of orthogonal OAM states, i.e., integer values of *m*, can be mapped to a vector space representing all possible combinations of the two states. The Poincaré sphere is most commonly used to represent polarization states resulting from two orthogonal polarization states: right and left hand circular. The HOPES is an analogous to this where instead we will look at two orthogonal left and right hand OAM states with equal OAM magnitudes [62]. Figure C.1 shows a Poincaré sphere for $m = 2$, where the poles represent pure OAM states, the equator represents a combination of the two with equal powers and a relative phase δ, and the rest of the surface of the sphere represents various ratios of the two, where the radius of the sphere represents the total power of the CCOAM mode [40].

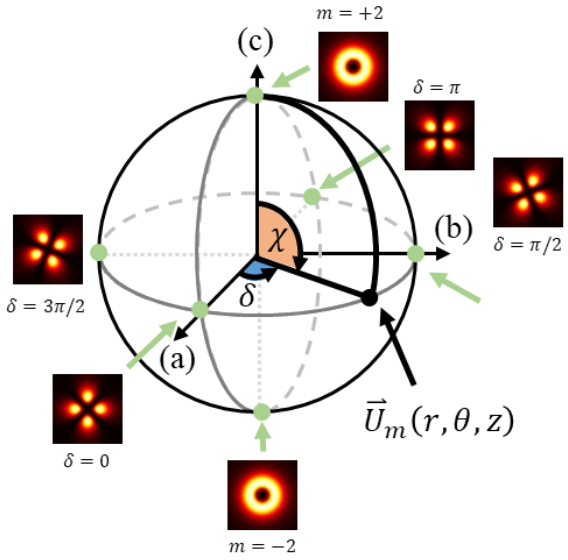

Figure C-1: HOPES for U_m which is the expression for the coherent combination of *m*=+2 and *m*=-2 with the three stokes parameter projections along (a), (b), and (c)

For a polarization Poincaré sphere, Stokes parameters are used to map a received mode into the vector space. For the HOPES, Stokes equivalent parameters will be used to recover the necessary modal information. Four measurements are typically needed to map the state. Two are used to map the signal to map to the axes given in Fig. C.1 (a) and (b), and two measurements are used to map to the axis given in Fig. C.1 (c) and to measure the total power of the signal.

Recall that the CCOAM state $U_{\pm m}(\rho,\chi,\delta)$ can be generalized as [74]:

$$U_{\pm m}(\rho,\chi,\delta)=\sqrt{\rho}\cos\left(\frac{\chi}{2}\right)\exp(-im\theta)+\sqrt{\rho}\sin\left(\frac{\chi}{2}\right)\exp(i\delta)\exp(+im\theta) \quad \text{(C.1)}$$

where (ρ,χ,δ) represent the spherical coordinates of the Poincaré equivalent sphere and θ is the azimuthal coordinate of the spatial profile. The projection of $U_{\pm m}(\rho,\chi,\delta)$ along the axis given in Fig. C.1 (a) has $\delta = 0$ and $\chi = \pi/2$, The projection along the axis given in Fig. C.1 (b) has $\delta = \pi/2$ and $\chi = \pi/2$. The power proportional to the top pole given along Fig. C.1 (c) requires $\chi = 0$. The power proportional to the bottom pole requires $\chi = 2\pi$ so that equation C.1 becomes

$$
\begin{aligned}
U_{\pm m(a)}\left(\chi=\frac{\pi}{2},\theta,\delta=0\right) &= \sqrt{\frac{\rho}{2}}\exp(im\theta)+\sqrt{\frac{\rho}{2}}\exp(-im\theta) \\
U_{\pm m(b)}\left(\chi=\frac{\pi}{2},\theta,\delta=\frac{\pi}{2}\right) &= \sqrt{\frac{\rho}{2}}\exp(im\theta)+\sqrt{\frac{\rho}{2}}\exp\left(i\frac{\pi}{2}\right)\exp(-im\theta) \\
U_{\pm m(c1)}(\chi=0,\theta,\delta) &= \sqrt{\rho}\exp(im\theta) \\
U_{\pm m(c2)}(\chi=2\pi,\theta,\delta) &= \sqrt{\rho}\exp(i\delta)\exp(-im\theta)
\end{aligned}
\tag{C.2}
$$

The corresponding phase-only correlation optics can therefore be defined by the conjugate of the phase of the four profiles given in Eq. C.2

$$
\begin{aligned}
\Phi_a &= \cos(m\theta) \\
\Phi_b &= \cos\left(m\left[\theta-\frac{\pi}{4m}\right]\right) \\
\Phi_{+m} &= \exp(-im\theta) \\
\Phi_{-m} &= \exp(+im\theta)
\end{aligned}
\tag{C.3}
$$

The phase profiles are shown in Fig. C-2 for m=2.

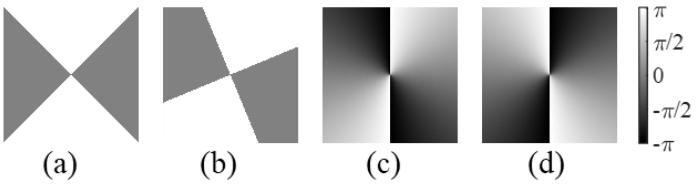

Figure C-2. Phase profiles of the phase-only correlation optics given in equation C.3 for (a) Φ_a, (b) Φ_b, (c) Φ_{c1}, and (d) Φ_{c2}. Note that (a) and (b) have the same profile with a relative rotation of π/4 radians for $m = 2$.

Using these four optical components as phase-match optics in a correlation setup produces on-axis powers given by the convolution of $U_{\pm m}(\chi,\theta,\delta)$ and the optics given in equation C.3 which can be easily calculated using convolution theorem property of Fourier Transforms:

$$\begin{aligned} P_a &= \rho\left[1+\sin(\chi)\cos(\delta)\right] \\ P_b &= \rho\left[1+\sin(\chi)\sin(\delta)\right] \\ P_{+m} &= \frac{\rho}{2}\left[1+\cos(\chi)\right] \\ P_{-m} &= \frac{\rho}{2}\left[1-\cos(\chi)\right] \end{aligned} \tag{C.4}$$

where P_{tot} gives the total power of the CCOAM mode, the position on the sphere can be determined using

$$\rho = P_{+m} + P_{-m} \qquad \text{(C.5)}$$
$$\chi = \cos^{-1}\left(\frac{P_{+m} - P_{-m}}{\rho}\right).$$
$$\delta = \tan^{-1}\left(\frac{P_b - \rho}{P_a - \rho}\right)$$

Note that P_{tot} is the radius of the sphere. Equivalently, the state can easily be represented in Cartesian coordinates:

$$X = P_a - \rho \qquad \text{(C.6)}$$
$$Y = P_b - \rho \quad .$$
$$Z = P_{c1} - P_{c2}$$

B.1. Optical Correlation Overview

Similar to the correlators in our previous work [7, 39, 40], the optical setups utilize a single optical correlation to recover phase modulation information by transforming the phase modulation information into an amplitude modulation that is then collected with a detector as shown in Figure 5.2.1. These setups exploit the convolution property of Fourier transforms. Propagation of a beam through an optical element can mathematically be represented as a multiplication of the two. Propagation through a lens produces a Fourier transform one focal length away from the lens. This produces a mathematical convolution whose on-axis intensity contains the correlation coefficient.

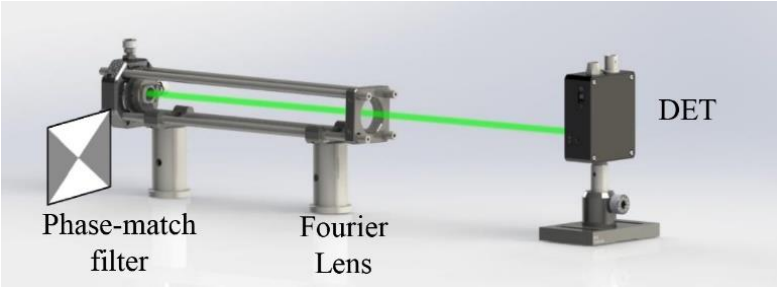

Figure 5.2.1. Receiver schematic showing phase match filter for two CCOAM beams with |m|=2 with correlation incident on the detector DET

The phase match optic corresponds to the argument of equation 3.3 which appears as a binary optic with four wedges with alternating phase values of 0 and π as shown in Fig. 3.2.1. The active area of the detector is aligned to collect the on-axis correlation information. As shown in [39, 40], the power contained in the correlation spot, P, can be analytically expressed by $P \propto \cos(\delta)+1$ such that as the relative phase δ is changed, the receiver power will hit a maximum value when $\delta=0$ and a minimum value when $\delta=\pi$. More details can be found in Appendix B, which fully describes mode recovery.

Appendix C

Log-polar transformation and optical design

The work presented in this document references a set of log-polar transformation optics that perform a geometrical transformation of an incident beam from Cartesian coordinates to Polar coordinates or vice-versa depending on the direction of propagation through the set [66, 49, 34, 33].

In this work, we are primarily concerned with the generation of OAM states. The two optics have phase profiles defined by

$$\Phi_u(x,y) = \frac{2\pi a}{\lambda f}\left(y\arctan\left(\frac{y}{x}\right) - x\ln\left(\frac{\sqrt{x^2+y^2}}{b}\right) + x\right) - \frac{\pi}{\lambda f}\left(x^2+y^2\right)$$
$$\Phi_w(u,v) = -\frac{2\pi ab}{\lambda f}\exp\left(-\frac{u}{a}\right)\cos\left(\frac{v}{a}\right) - \frac{\pi}{\lambda f}\left(u^2+v^2\right) \quad \text{(C.2)}$$

where the (x,y) coordinates are transformed into (u,v) or vice versa depending on the direction of propagation through the optics, f is the focal length of a built in lens and determines the separation of the optics, $2\pi a$ determines the line length, and b determines the shift of the line on Ω_W. For the $\lambda = 450$ nm build, $f = 200$ mm, $2\pi a = 3.6$ mm, and $b = 2$ mm. For more detection the optics are placed $\Omega_U \rightarrow \Omega_W$. For mode generation the signal is propagated in the reverse direction.

Appendix D

Phase Locked Loop

Mechanically, techniques such as cage systems and enclosures can be used to minimize system vibrations, temperature fluctuations, and air currents but this will not completely eliminate the issue, only slow it down. The measured rate of change of the phase drift is typically on the order of 1 Hz or slower, but could easily reach rates in excess of hundreds of Hz due to any vibrations or disturbances present.

In this work we create a phase-locked loop (PLL) to recover the phase delay of a known transmitted signal using the detection techniques presented in Appendix C. The beam generation setup is given in Figure 3.3.3. A small portion of the transmitted beam is collected using a 10% pickoff. This is then sent to a receiver setup, shown in Fig. D.1 to recover the beam orientation using two optical correlations. The optical correlation power is captured using two photo detectors. This signal is then collected using two ADC ports on an Arduino Due. A simple algorithm is then employed to normalize the signals and compute the phase information using the computations given in Appendix C. This is compared to the desired setpoint to calculate the error. This error is integrated over time and sent to an amplifier before being applied to a slow modulator on one leg of the system. See the following sections for a more detailed explanation of the algorithm and code. . In this work we apply a phase bias using a PI-control loop to achieve a system with RMS phase error of $< \lambda/46$.

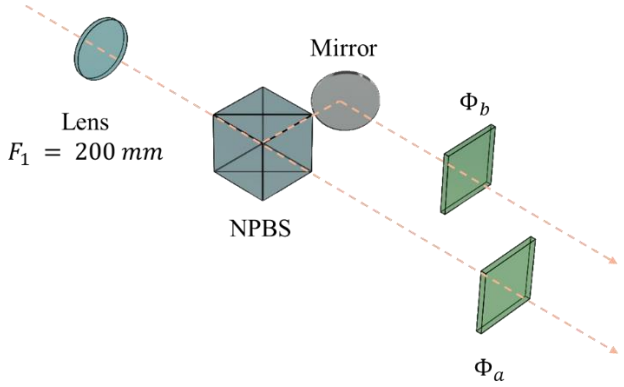

Figure D-1 Schematic diagram of receiver setup where the optical elements Φ_a and Φ_b are placed in the Fourier plane of the lens. A non-polarizing beam splitter (NPBS) is used to split the signal into two equal parts

D.1. Optical Correlation

This subsection will briefly cover the optical correlation used in the phase locked loop as it is slightly different than the setup given Appendix B. Both function on the Fourier transform convolution theorem which states that multiplication in the spatial domain produces a convolution in the frequency domain and vice-versa. The setup shown in Figure D-1 is simplified and the ideal case is shown in Figure D.2.

Figure D.2 shows a 4F system with a magnification of 1. It is well known that lenses take the Fourier transform of an input beam. In addition, the Fourier-transformation will have an additional parabolic phase term if the object or image you are trying to transform is not placed 1F before the lens. By placing the correlation filter at the focus of the lens, we are performing a multiplication of the Fourier transform of the incident mode by the phase component of the optic placed in this plane. As the beam propagates to the second optic, an additional 1F away, the inverse Fourier transformation is performed. Thus we have just

performed a convolution of the input beam with the phase-match optic. A convolution produces a correlation surface, whose on-axis information as mentioned in section 3.2 gives the correlation coefficient proportional to the total power of the beam.

In reality, 4F systems can have two different lens values. This produces a magnification of the output beam, where M = L2/L1. Therefore, by increasing the focal length of the second lens we can magnify the system, creating a larger correlation spot. In addition, because we are not interested in the wavefront of the correlation, we can remove the second optic. This was done in the setup, where the photodetectors were placed approximately 500 mm after the correlation optics such that the active area of the detectors could be used to collect only the correlation power.

D.2. Algorithm Implementation

The implemented PLL algorithm is shown in Figure C-1.

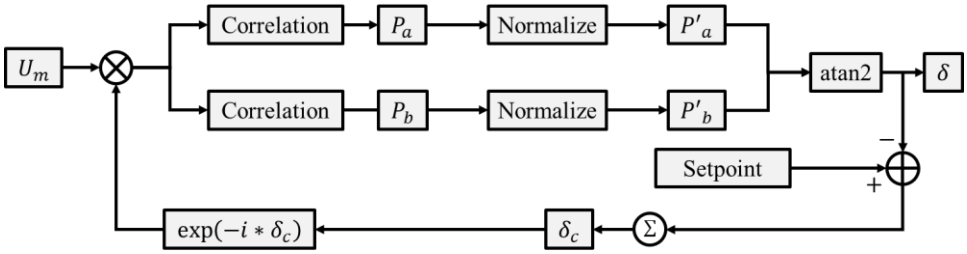

Figure D-2. General flow diagram overview for PLL. Two optical correlations are done to collect the orientation information. The Arduino code normalizes the signals so that the inverse tangent can be taken to recover the relative phase δ. δ is then compared to a setpoint in the code which determines the error relative to the desired orientation. The cumulative sum of the error is then applied to the phase modulator.

The actual implementation of the algorithm is slightly more complex, for two reasons. First, phase modulation is cyclical. Generally speaking, control loops need to be linear, time invariant systems. Therefore, when the inverse tangent is taken of the two correlation signals, the output is limited between [-π,π]. This means that the system no longer appears linear, instead there is a modulo 2π of the phase drift, meaning the system no longer has one to one mapping and is not linear. The inverse tangent produces apparent instantaneous phase jumps that cause unnecessary integration instability. Therefore, if the program looks at the difference between the current and previous values and if it sees a magnitude change greater than π, the signal is shifted up or down by 2π accordingly, creating a linear system.

First, the measured phase must be converted to a voltage signal applied to a phase modulator. Next the Arduino Due has a DAC output limited between 0.55 V and 2.2 V while the phase drift is unlimited. Therefore, after calculating the phase driftthe output is confined between -3π/2 and 3π/2, and when the signals hit these thresholds they are shifted by 2π in the proper direction. This not only limits the output voltage but allowing the range to exceed 2π prevents the output voltage from switching rapidly between positive and negative values when it is near the thresholds. Lastly, this signal is converted to a voltage value and scaled such that π modulation is equal to $V\pi$, the voltage required by the modulator.

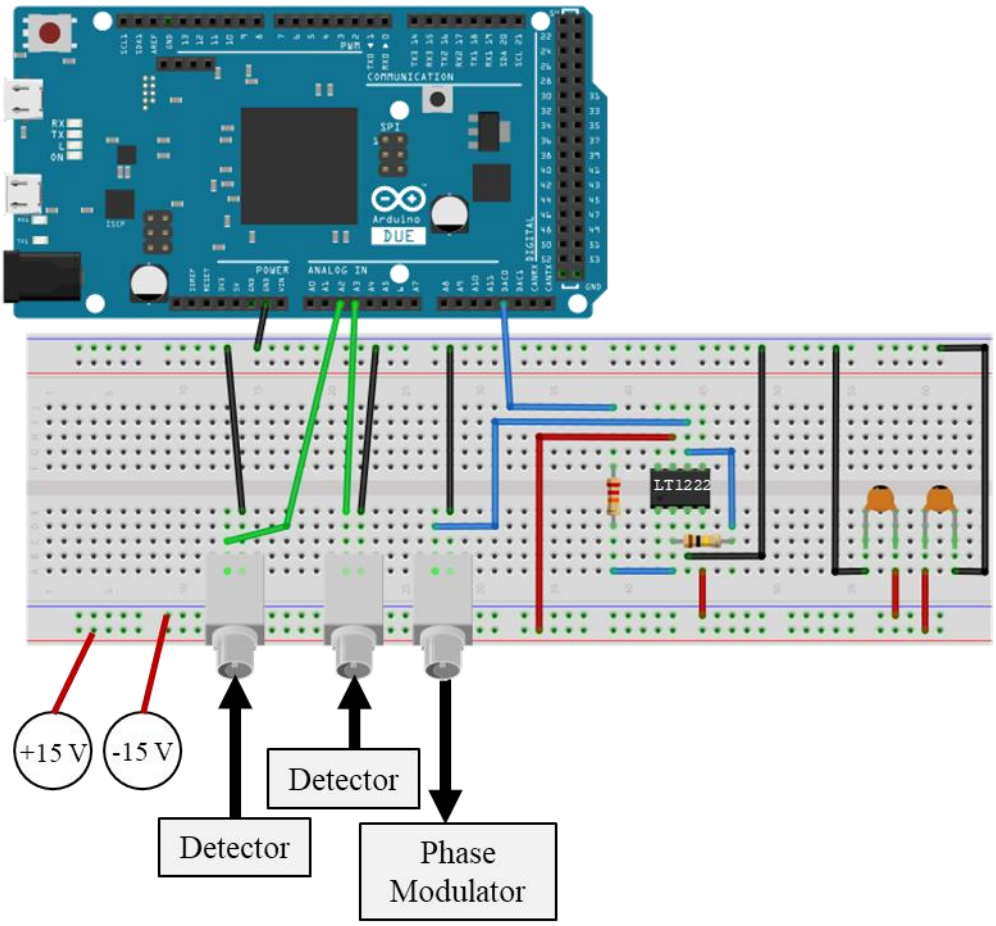

Figure D-3. Circuit schematic for Arduino Due feedback loop with amplification of the output signal.

Figure D-3 shows a simple operational amplifier chip, LT1222, used in an inverting operational amplifier setup. The schematic diagram is shown in Fig. D-4, where the gain of the circuit is calculated using.

$$V_{out} = -V_{in} \frac{R_f}{R_i} \tag{D.1}$$

where V_{in} is the signal output by the DAC0 pin, R_f and R_i are given in Figure D-1 and produce a 5x gain.

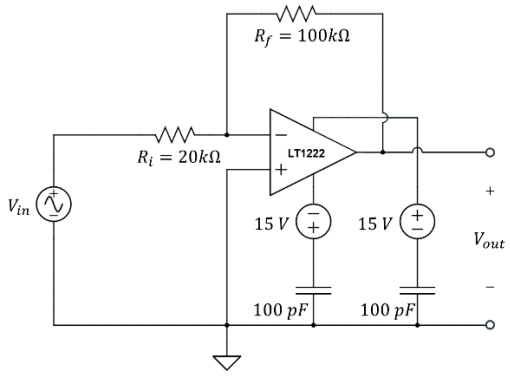

Figure D-4. Circuit schematic for operational amplifier design.

The LT1222 chip was selected for its high Gain-Bandwidth product of 500 MHz, so for a gain of 5x, the bandwidth of the amplifier is 100 MHz.

D.3. Code

```
#include <math.h>

//input and output pins
int analogINPin1 = A3;
int analogINPin2 = A2;
int analogINPin3 = A0;
int analogOUTPin_D0 = DAC0;
int analogOUTPin_D1 = DAC1;

//Value storage
int DET1 = 0;  // variable to store the value read
int DET2 = 0;  // variable to store the value read
int PHASE_out = 0;  // variable to store the value read
int max_val1 = 0;
int max_val2 = 0;
int min_val1 = 0;
int min_val2 = 0;
int dt;
int out1 = 0;
int out2 = 0;
double amp1;
double amp2;
double amp3;
double DET1_scaled;
double DET2_scaled;
```

```
double Theta;
double Theta2;
double ERROR1;
double ERROR2;
double OUTPUT_value;
double cumulative_error = 0;
double SHIFT1 = 0;
double SHIFT2 = 0;
double Prev_Theta = 0;
double Error_diff = 0;
double setpoint = 0;
double prev_error1 = 0;
double prev_error2 = 0;
bool TIMEOUT = 0;
int v2pi = 1655; //2pi value out of arduino
int v2pi_shift = 3500 - v2pi; // center voltage signal
int t_start = millis();
int t_end = t_start;

void setup() {
  // put your setup code here, to run once:
  Serial.begin(9600);      // open the serial port at 9600 bps:

  // set read and write resolution
  analogReadResolution(12);
  analogWriteResolution(12);
  t_start = millis();
}

void loop() {
  // put your main code here, to run repeatedly:
    //Test Timing
    digitalWrite(13,TIMEOUT);
    TIMEOUT = !TIMEOUT;  //Measure the output on pin 13 to get the
                              runtime for this code

    // read in voltages from two detectors
    DET1 = analogRead(analogINPin1);  // read the input pin
    DET2 = analogRead(analogINPin2);  // read the input pin


    //Compute total elapsed time
    t_end = millis();
    dt = t_end - t_start;


    //COMPUTE MAX AND MIN VALUES OF EACH DETECTOR for 1 second
    if (dt < 1000) {

      //Ramp output voltage
        PHASE_out = PHASE_out + 10;

        if (out1 >= 4000) {
          PHASE_out = 50;
```

```
    }

  analogWrite(analogOUTPin_D0, PHASE_out); //write ramp

  //STORE MAX AND MIN VALUES
  if (DET1 > max_val1) {
    max_val1 = DET1;
  }
  if (DET2 > max_val2) {
    max_val2 = DET2;
  }
  if (DET1 < min_val1) {
    min_val1 = DET1;
  }
  if (DET2 < min_val2) {
    min_val2 = DET2;
  }
}

//BEGIN PHASE RECOVERY
if (dt >= 1000) {


  amp1 = DET1;
  amp2 = max_val1;
  amp3 = min_val1;
  DET1_scaled = ((amp1 - amp3) / (amp2 - amp3) - 0.5) * 2;

  amp1 = DET2;
  amp2 = max_val2;
  amp3 = min_val2;
  DET2_scaled = ((amp1 - amp3) / (amp2 - amp3) - 0.5) * 2;


  //Calculate phase
  Theta = atan2(DET2_scaled,DET1_scaled);

  //Change in measured phase from previous step
  Error_diff = Theta - Prev_Theta;

  //CORRECT FOR MOD2pi of inverse tangent and rework where the
                          modulo is taken
    if (Error_diff > 2 * M_PI * 0.8) {
      SHIFT1 = SHIFT1 + 2 * M_PI;
    }

    if (Error_diff < -2 * M_PI * 0.8) {
      SHIFT1 = SHIFT1 - 2 * M_PI;
    }

      Theta2 = Theta - SHIFT1;
      Prev_Theta = Theta;
```

```
        ERROR1 = setpoint - Theta2;
        ERROR2 = ERROR1 + SHIFT2;

        //LIMIT OUTPUT (rework modulo)
        if (ERROR2 < -M_PI) {
          SHIFT2 = SHIFT2 + 2*M_PI;
        }
        if (ERROR2 > M_PI) {
          SHIFT2 = SHIFT2 - 2*M_PI;
        }

        //FINAL OUTPUT FOR ONE TIMESTEP
        ERROR2 = ERROR1 + SHIFT2;

        //CALCULATE CUMULATIVE ERROR
        cumulative_error = ERROR2 + prev_error2;
        prev_error2 = cumulative_error;

        //CONVERT OUTPUT PHASE TO ARDUINO VALUE (integer between 0
                                and 4092)
        OUTPUT_value = (cumulative_error / ( M_PI) + 1)/2 * v2pi +
                                v2pi_shift;
        out1 = (int) round(OUTPUT_value);

        //WRITE VOLTAGE OUT
        analogWrite(analogOUTPin_D0, out1);
        //analogWrite(analogOUTPin_D1, out2);  //Here you can put any
                                other voltages you want to monitor. Make
                                sure to do a voltage conversion!

    }
}
```

Appendix E

Constant Envelope OFDM

Orthogonal frequency division multiplexing (OFDM) is another common technique used to expand the data rate of a bandwidth limited system and has been successfully demonstrated in the underwater environment using blue laser diodes [11,12]. The data rates presented in [11,12] are extremely high for free-space underwater links, but the authors allude to potential spatial and temporal dispersion issues caused by optical propagation through turbid environments. In OFDM, bits of complex data are encoded using several orthogonal frequency carriers whose orthogonality minimizes crosstalk between the frequencies. In the time-domain, this signal appears as the summation of several shifted sinusoids of various amplitudes at each of the carrier frequencies. This summation typically results in a large peak to average power ratio (PAPR), which can be a major issue, particularly when applying any nonlinear manipulation of the signal such as amplification or other harmonic generation processes.

Constant envelope OFDM (CE-OFDM) is a technique that reduces the PAPR by modifying the OFDM signal [13]. This is extremely advantageous in an underwater environment for many reasons. OFDM signals are robust to latency effects and is an effective means of transmitting large quantities of data over short periods of time. In addition, CE-OFDM promotes power-scalability, and when combined with OAM, the delivered power is constant, promoting power delivery in addition to information transfer. CE-OFDM uses phase modulation to transform a typical OFDM signal into a signal that

can be used in nonlinear processes. At the receiver, phase demodulation must be used to perform the inverse transformation.

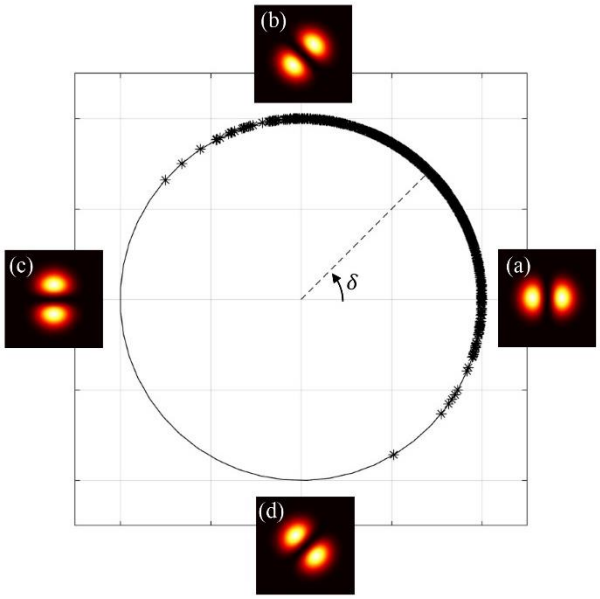

Fig. E-1. CE-OFDM illustration for s(t) with 2πh=0.5 and δ=π/4 where s(t) with corresponding beam profiles are shown at (a) φ(t) = 0, (b) φ(t) = π/2, (c) φ(t) = π, and (d) φ(t) = 3π/2.

A typical OFDM signal can be expressed as [14]

$$\varphi(t) = 2\pi hC\sum_{k=1}^{N} \Re\{X[k]\}\cos\left(\frac{2\pi kt}{T}\right) - \Im\{X[k]\}\sin\left(\frac{2\pi kt}{T}\right) \tag{E.1}$$

over $-T_{cp} \le t < T$, where T_{cp} is the cyclic prefix duration, T is the duration of the OFDM block, $2\pi h$ is the modulation index in radians such that the variance of $\varphi(t)$ is $\sigma^2 = (2\pi h)^2$, C is a constant, and X[k] is a vector of N complex data symbols. This is the real-valued

information-carrying message signal that is transformed into the CE-OFDM signal given by [14].

$$s(t) = A\exp\left\{i\left[\varphi(t) + \delta_0\right]\right\} \tag{E.2}$$

over $-T_{cp} \le t < T$, where A is the signal amplitude, and δ_0 is an arbitrary phase offset, and is ideally 0. Visually, this signal can be represented as shown in Fig. E-1 as a signal with constant amplitude and is encoded into the phase difference between the two CCOAM beams.

Instead of phase demodulation, direct detection is a technique used to reduce receiver complexity using a single measurement to recover the OFDM signal [15-17]. To do this optically, optical correlators are commonly used to very efficiently recover and identify mode structures [18] in which the recovered signal becomes

$$r(t) \propto \left[\cos\left(\varphi(t) + \delta_0 + \delta_{drift}\right) + 1\right] \tag{E.3}$$

where δ_{drift} is an additional phase drift that can occur when combining the OAM modes. This can be caused by random temperature fluctuations, vibrations, ect. that cause small differences in the optical paths of each coherent mode resulting from most interferometric combination techniques. In order to successfully recover the phase modulation on the signal, ideally this would be a 1-to-1 mapping of the $\varphi(t)$ to $r(t)$. Since only a single detector is used to recover the signal, the receiver will recover a distorted signal. When $2\pi h$ increases to 0.5 and beyond, the fidelity of the signal decreases as we leave the 1-to-1 mapping region. In fact, the recovered signal will begin to double. This can also occur if the reference phase

drifts too far. This is why the phase- locked control loop is necessary, otherwise the signal fidelity and distortion will randomly drift due to the cosine mapping at the receiver.

Appendix F

Pulsed Source

The EPC9126 board is able to create short optical pulses by charging and discharging capacitors. The discharged current flows through the laser diode and produces an optical pulse proportional to the current. A square wave signal operating at 1 kHz controls the repetition rate by switching on and off a transistor. The FWHM of the pulse is calculated using the equation given in [75]:

$$t_w = \frac{2\pi\sqrt{L_1 C_1}}{3} \tag{F.1}$$

Appendix G

Direct Phase Measurement Interferometry

Direct phase measurement interferometry (DPMI) is a coherent technique employed to calculate the wavefront of an optical signal using interferometric intensity patterns and is typically used to measure the quality of optical surfaces. Typically, the reference signal has a planar wavefront and it is used to measure the optical flatness of substrates. There are several techniques and algorithms, but in this work we are using the four-measurement technique where each interference pattern is created with a phase difference of 0, $\pi/2$, π, and $3\pi/2$ relative to the reference signal as given in [76]. The four intensity profiles can be described as

$$\begin{aligned} I_1(x,y) &= \left|\vec{U}_0 + \vec{U}_m\right|^2 \\ I_2(x,y) &= \left|\vec{U}_0 + \vec{U}_m \exp\left(-i\pi/2\right)\right|^2 \\ I_3(x,y) &= \left|\vec{U}_0 + \vec{U}_m \exp\left(-i\pi\right)\right|^2 \\ I_4(x,y) &= \left|\vec{U}_0 + \vec{U}_m \exp\left(-i3\pi/2\right)\right|^2 \end{aligned} \tag{F.1}$$

where the reference beam is given by

$$U_0(x,y) = U_0(x,y)\exp\left(-i\phi_0(x,y)\right) \tag{F.2}$$

and the expression for the beam with the wavefront we are trying to measure given by

$$U_m(x,y) = U_m(x,y)\exp\left(-i\phi_m(x,y)\right) \tag{F.3}$$

where U_0 and U_m represent the amplitude and ϕ_0 and ϕ_m represent the wavefront of the respective beams.

Plugging equations F.2 and F.3 into the equations given in F.1 give

$$\begin{aligned} I_1(x,y) &= |U_0|^2 + |U_m|^2 + 2U_0U_m\cos(\phi_0 - \phi_m) \\ I_2(x,y) &= |U_0|^2 + |U_m|^2 - 2U_0U_m\sin(\phi_0 - \phi_m) \\ I_3(x,y) &= |U_0|^2 + |U_m|^2 - 2U_0U_m\cos(\phi_0 - \phi_m) \\ I_4(x,y) &= |U_0|^2 + |U_m|^2 + 2U_0U_m\sin(\phi_0 - \phi_m) \end{aligned} \quad \text{(F.4)}$$

Using basic trigonometry we can combine the four equations given in F.4 so that

$$\phi_0(x,y) - \phi_m(x,y) = \tan^{-1}\left(\frac{I_4(x,y) - I_2(x,y)}{I_1(x,y) - I_3(x,y)}\right). \quad \text{(F.5)}$$

Therefore, the recovered wavefront $\phi(x,y)$ is actually the difference between the reference and unknown wavefronts.

$$\phi(x,y) = \phi_0(x,y) - \phi_m(x,y). \quad \text{(F.5)}$$

REFERENCES

[1] L. Allen, M. W. Beijersbergen, R. J. Spreeuw and J. P. Woerdman, "Orbital angular momentum of light and the transformation of laguerre-gaussian laser modes," *Physical Review A*, vol. 45, no. 11, p. 8185, 1992.

[2] B. M. Cochenour, L. J. Mullen and A. E. Laux, "Characterization of the Beam-Spread Function for Underwater Wireless Optical Communications Links," *IEEE Journal of Oceanic Engineering*, vol. 33, no. 4, pp. 513-521, 2008.

[3] B. R. Brown and A. W. Lohmann, "Complex spatial filtering with binary masks," *Applied optics*, vol. 5, no. 6, pp. 967-969, 1966.

[4] D. Casasent and P. Demitri, "Position, rotation, and scale invariant optical correlation," *Applied Optics*, vol. 15, no. 7, pp. 1795-1799, 1976.

[5] J. W. Goodman, Introduction to Fourier Optics, Roberts and Company Publishers, 2005.

[6] J. Wang, "Advances in communications using optical vortices," *Photonics Research*, vol. 4, no. 5, pp. B14-B28, 2016.

[7] J. Baghdady, K. Miller, K. Morgan, M. Byrd, S. Ossler, R. Robert and L. Wenzhe, "Multi-gigabit/s underwater optical communication link using orbital angular momentum multiplexing," *Optics Express*, vol. 24, no. 9, pp. 9794-9805, 2016.

[8] J. K. Miller, K. S. Morgan, W. Li, Y. Li, I. Srimathi-Raghu, J. Baghdady, J. Kelly and E. G. Johnson, "Underwater optical communication link using polarization division multiplexing and orbital angular momentum multiplexing," in *OCEANS 2017*, Anchorage, 2017.

[9] Y. Ren, L. Li, Wang Zhe, S. Kamali, E. Arbabi, A. Arbabi, Z. Zhao, G. Xie, Y. Cao, N. Ahmed and Others, "Orbital angular momentum-based space division multiplexing for high-capacity underwater optical communications," *Scientific Reports*, vol. 6, p. 33306, 2016.

[10] G. M. Hale and M. R. Querry, "Optical constants of water in the 200-nm to 200-μm wavelength region," *Applied Optics*, vol. 12, no. 3, pp. 555-563, 1 March 1973.

[11] R. M. Pope and E. S. Fry, "Absorption spectrum (380-700 nm) of pure water. II. Integrating cavity measurements," *Applied Optics,* vol. 36, no. 33, pp. 8710-8723, 1997.

[12] C. Wang, H.-Y. Yu and Y.-J. Zhu, "A long distance underwater visible light communication system with single photon avalanche diode," *IEEE Photonics Journal,* vol. 8, no. 5, pp. 1-11, 2013.

[13] J. Wang, C. Lu, S. Li and Z. Xu, "100 m/500 Mbps underwater optical wireless communication using an NRZ-OOK modulated 520 nm laser diode," *Optics Express,* vol. 27, no. 9, pp. 12171-12181, 2019.

[14] F. Hanson and S. Radic, "High bandwidth underwater optical communication," *Applied Optics,* vol. 47, no. 2, pp. 277-283, 2008.

[15] D. F. Swinehart, "The beer-lambert law," *Journal of Chemical Education,* vol. 39, no. 7, pp. 333-335, 1962.

[16] B. Cochenour, L. Mullen and J. Muth, "Temporal response of the underwater optical channel for high-bandwidth wireless laser communications," *IEEE Journal of Oceanic Engineering,* vol. 38, no. 4, pp. 730-740, 2013.

[17] K. S. Morgan, E. G. Johnson and B. M. Cochenour, "Attenuation of beams with orbital angular momentum for underwater communication systems," in *OCEANS 2015*, Washington, 2015.

[18] B. Cochenour, K. Morgan, J. K. Miller, E. G. Johnson, K. Dunn and L. Mullen, "Propagation of modulated optical beams carrying orbital angular momentum in turbid water," *Applied Optics,* vol. 55, no. 31, pp. C34-C38, 2016.

[19] N. B. Simpson, L. Allen and M. J. Padjett, "Optical tweezers and optical spanners with Laguerre-Gaussian modes," *Journal of Modern Optics,* vol. 43, no. 12, pp. 2485-2491, 1996.

[20] S. Franke-Arnold, J. Leach, M. J. Padgett, V. E. Lembessis, D. Ellinas, A. J. Wright, J. M. Girkin, P. Öhberg and A. S. Arnold, "Optical ferris wheel for ultracold atoms," *Optics Express,* vol. 15, no. 14, pp. 8619-8625, 2007.

[21] G. Foo, D. M. Palacios and G. A. Swatzlander, "Optical vortex coronagraph," *Optics Letters,* vol. 30, no. 24, pp. 3308-3310, 2005.

[22] B. Jack, J. Leach, J. Romero, S. Ranke-Arnold, M. Ritsch-Marte, S. M. Barnett and M. J. Padgett, "Holographic ghost imaging and the violation of a Bell inequality," *Physical Review Letters,* vol. 103, no. 8, p. 083602, 2009.

[23] R. Fickler, R. Lapkiewicz, W. N. Plick, M. Krenn, C. Schaeff, S. Ramelow and A. Zeilinger, "Quantum entanglement of high angular momenta," *Science,* vol. 338, no. 6107, pp. 640-643, 2012.

[24] E. Nagali, F. Sciarrino, F. De Martin, L. Marrucci, B. Piccirillo, E. Karimi and E. Santamato, "Quantum information transfer from spin to orbital angular momentum of photons," *Physical Review Letters,* vol. 103, no. 1, p. 013601, 2009.

[25] Y. Yan, G. Xie, M. P. Lavery, H. Huang, Ahmed Nisar, Bao Changjing, Y. Ren, Y. Cao, L. Li, Z. Zhao, A. F. Molisch, M. Tur, M. J. Padgett and A. E. Willner, "High-capacity millimetre-wave communications with orbital angular momentum multiplexing," *Nature Communications,* vol. 5, no. 1, pp. 1-9, 2014.

[26] A. E. Willner, H. Huang, Y. Yan, Y. Ren, N. Ahmed, G. Xie, C. Bao, L. Li, Y. Cao, Z. Zhao, J. Wang, M. P. Lavery, M. Tur, S. Tamachandran, A. F. Molisch, N. Ashrafi and S. Ashrafi, "Optical communications using orbital angular momentum beams," *Advances in Optics and Photonics,* vol. 7, no. 1, pp. 66-106, 2015.

[27] A. S. Rury and R. Freeling, "Mie scattering of purely azimuthal Laguerre-Gauss beams: Angular-momentum-induced transparency," *Physical Review A,* vol. 86, no. 5, p. 053830, 2012.

[28] C. Schwartz and A. Dogariu, "Conservation of angular momentum of light in single scattering," *Optics Express,* vol. 14, no. 18, pp. 8425-8433, 2006.

[29] J. Courtial and M. J. Padgett, "Performance of a cylindrical lens mode converter for producing Laguerre--Gaussian laser modes," *Optics Communications,* vol. 159, no. 1-3, pp. 13-18, 1999.

[30] K. Sueda, G. Miyaji, N. Miyanaga and M. Nakatsuka, "Laguerre-Gaussian beam generated with a multilevel spiral phase plate for high intensity laser pulses," *Optics Express,* vol. 12, no. 15, pp. 3548-3553, 2004.

[31] Z. Zhao, J. Wang, S. Li and A. Willner, "Metamaterials-based broadband generation of orbital angular momentum carrying vector beams," *Optics Letters,* vol. 38, no. 6, pp. 932-934, 2013.

[32] W. Li, K. Morgan, Y. Li, J. K. Miller, G. White, R. J. Watkins and E. G. Johnson, "Rapidly tunable orbital angular momentum (OAM) system for higher order Bessel beams integrated in time (HOBBIT)," *Optics Express*, vol. 27, no. 4, pp. 3920-3934, 2019.

[33] G. Ruffato, M. Massari, G. Parisi and F. Romanato, "Test of mode-division multiplexing and demultiplexing in free-space with diffractive transformation optics," *Optics Express,* vol. 25, no. 7, pp. 7859-7868, 2017.

[34] G. Ruffato, M. Massari and F. Romanato, "Diffractive optics for combined spatial- and mode- division demultiplexing of optical vortices: design, fabrication and optical characterization," *Scientific Reports,* vol. 6, p. 24760, 2016.

[35] D. Flamm, D. Naidoo, C. Schulze, A. Forbes and M. Duparre, "Mode analysis with a spatial light modulator as a correlation filter," *Optics Letters,* vol. 37, no. 13, pp. 2478-2480, 2012.

[36] M. Krenn, R. Fickler, M. Fink, J. Handsteiner, M. Malik, T. Scheidl, R. Ursin and A. Zeilinger, "ommunication with spatially modulated light through turbulent air across Vienna," *New Journal of Physics,* vol. 16, no. 11, p. 113028, 2014.

[37] C. Gibson, J. Courtial, M. Padgett, M. Vasnetsov, V. Pas'ko, S. Barnett and S. Franke-Arnold, "Free-space information transfer using light beams carrying orbital angular momentum," *Optics Express,* vol. 12, no. 22, pp. 5448-5456, 2004.

[38] E. Karimi, B. Piccirillo, E. Nagali, L. Marrucci and E. Santamato, "Efficient generation and sorting of orbital angular momentum eigenmodes of light by thermally tuned q-plates," *Applied Physics Letters,* vol. 94, no. 23, p. 231124, 2009.

[39] K. Morgan, Y. Li, W. Li, J. K. Miller, R. J. Watkins and E. G. Johnson, "Multilevel quadrature amplitude multiplexing using coherently coupled orbital angular momentum modes," *Optics Express,* vol. 26, no. 9, pp. 12180-12190, 2018.

[40] Y. Li, K. Morgan, W. Li, J. K. Miller, R. J. Watkins and E. G. Johnson, "Multi-dimensional QAM equivalent constellation using coherently coupled orbital angular momentum (OAM) modes in optical communication," *Optics Express,* vol. 26, no. 23, pp. 30969-30977, 2018.

[41] Z. Zhao, H. Song, R. Zhang, K. Pang, C. Liu, H. Zong, A. Almaiman, K. Manukyan, H. Zhou, B. Lynn and R. W. Boyd, "Dynamic Spatiotemporal Beams that Combine Two Independent and Controllable Orbital-Angular-Momenta Using Multiple Optical-Frequency-Comb Lines," *arXiv preprint arXiv:1904.13150,* 2019.

[42] M. P. Lavery, F. C. Speirits, S. M. Barnett and M. J. Padgett, "Detection of a spinning object using light's orbital angular momentum," *Science,* vol. 341, no. 6145, pp. 537-540, 2013.

[43] A. Ryabtsev, S. Pouya, A. Safaripour, M. Koochesfahani and M. Dantus, "Fluid flow vorticity measurement using laser beams with orbital angular momentum," *Optics Express,* vol. 24, no. 11, pp. 11762-11767, 2016.

[44] M. I. Akhlaghi and A. Dogariu, "Tracking hidden objects using stochastic probing," *Optica,* vol. 4, no. 4, pp. 447-453, 2017.

[45] B. Cochenour , L. Rogers, A. Laux, L. Mullen, K. Morgan, J. K. Miller and E. G. Johnson, "The detection of objects in a turbid underwater medium using orbital angular momentum (OAM)," in *Ocean Sensing and Monitoring IX*, Anaheim, 2017.

[46] R. J. Watkins, K. Dai, G. White, W. Li, J. K. Miller, K. S. Morgan and E. G. Johnson, "Experimental probing of turbulence using a continuous spectrum of asymmetric OAM beams," *Optics Express,* vol. 48, no. 2, pp. 924-935, 2020.

[47] M. J. Strain, X. Cai, J. Wang , J. Zhu, D. B. Phillips, L. Chen, M. Lopex-Garcia, J. L. O'Brien, M. G. Thompson, M. Sorel and S. Yu, "Fast electrical switching of orbital

angular momentum modes using ultra-compact integrated vortex emitters," *Nature Communications,* vol. 5, no. 1, pp. 1-7, 2017.

[48] T. Lei, S. Gau, Z. Li, Y. Yuan, Y. Li, M. Zhang, G. N. Liu, Z. Zu , J. Tian and X. Yuan, "Fast-switchable OAM-based high capacity density optical router," *IEEE Photonics Journal,* vol. 9, no. 1, pp. 1-9, 2017.

[49] G. C. Berkhout, M. P. Lavery, J. Courtial, M. W. Beijersbergen and M. J. Padgett, "Efficient sorting of orbital angular momentum states of light," *Physical Review Letters,* vol. 105, no. 15, p. 153601, 2010.

[50] D. Asselin and H. H. Arsenault, "Rotation and scale invariance with polar and log-polar coordinate transformations," *Optics Communications,* vol. 104, no. 4-6, pp. 391-404, 1994.

[51] G. Ruffato, M. Massari, M. Girardi, G. Parisi, M. Sontini and F. Romanato, "Non-paraxial design and fabrication of a compact OAM sorter in the telecom infrared," *Optics Express,* vol. 27, no. 17, pp. 24123-24134, 2019.

[52] K. Dai, W. Li, K. S. Morgan, J. K. Miller, R. J. Watkins and E. G. Johnson, "Second-harmonic generation of asymmetric Bessel-Gaussian beams carrying orbital angular momentum," *Optics Express,* vol. 28, no. 2, pp. 2536-2546, 2020.

[53] A. Mair, A. Vaziri, G. Weihs and A. Zeilinger, "Entanglement of the orbital angular momentum states of photons," *Nature,* vol. 412, no. 6844, pp. 313-316, 2001.

[54] J. A. Anguita, J. Herreros and I. B. Djordjevic, "Coherent multimode OAM superpositions for multidimensional modulation," *IEEE Photonics Journal,* vol. 6, no. 2, pp. 1-11, 2017.

[55] M. Padgett, F. Miatto, M. Lavery, A. Zeilinger and R. Boyd, "Divergence of an orbital-angular-momentum-carrying beam upon propagation," *New Journal of Physics,* vol. 17, no. 2, p. 023011, 2015.

[56] T. J. Kulp, D. G. Garvis, R. B. Kennedy and T. Salmon, "Results of the second tank trial of the LLNL/NAVSEA underwater laser-imaging system," *Ocean Optics X,* vol. 1302, pp. 398-413, 1990.

[57] K. S. Morgan, J. K. Miller, W. Li, J. Baghdady and E. G. Johnson, "Propagation and dynamic manipulation of coherent orbital-angular-momentum modes through underwater turbid environments," in *Oceans 2016*, Monterey, 2016.

[58] K. S. Morgan, J. K. Miller, W. Li, Y. Li and E. G. Johnson, "Higher order Bessel beams integrated in time (HOBBIT) for free space underwater sensing and communication," in *Oceans 2017*, Anchorage, 2017.

[59] K. Morgan, J. K. Miller, W. Li, Y. Li and E. G. Johnson, "Dynamic Free-Space Propagation of Interfering Composite Vortices," in *Propagation Through and Characterization of Atmospheric and Oceanic Phenomena*, San Francisco, 2017.

[60] J.-F. Bisson, K. Miyamoto and T. Omatsu, "Power-scalable and high-speed orbital angular momentum modulator," *Japanese Journal of Applied Physics*, vol. 58, no. 3, p. 032009, 2019.

[61] A. E. Siegman, Lasers, University Science Books, 1986.

[62] M. J. Padgett and J. Courtial, "Poincaré-sphere equivalent for light beams containing orbital angular momentum," *Optics Letters*, vol. 24, no. 7, pp. 430-432, 1999.

[63] X. Yi, Y. Liu, X. Ling, X. Zhou, Y. Ke, H. Luo, S. Wen and D. Fan, "Hybrid-order Poincaré sphere," *Physical Review A*, vol. 91, no. 2, p. 023801, 2015.

[64] K. Dholakia, N. B. Simpson, M. J. Padgett and L. Allen, "Second-harmonic generation and the orbital angular momentum of light," *Physical Review A*, vol. 54, no. 5, p. R3742, 1996.

[65] G. Walker, A. S. Arnold and S. Franke-Arnold, "Trans-Spectral Orbital Angular Momentum Transfer via Four-Wave Mixing in Rb Vapor," *Physical Review Letters*, vol. 108, no. 24, p. 243601, 2012.

[66] W. Li, J. K. Miller, I. Srimathi-Raghu, Y. Li, K. Morgan and E. G. Johnson, "Efficient 1550 nm Diffractive Log-Polar Element Based Orbital Angular Momentum Mode-division Multiplexing," *Laser Science*, pp. JTu2A-37, 2017.

[67] K. S. Morgan, J. K. Miller, B. M. Cochenour, W. Li, Y. Li, R. J. Watkins and E. G. Johnson, "Free space propagation of concentric vortices through underwater turbid environments," *Journal of Optics,* vol. 18, no. 10, p. 104004, 2016.

[68] M. J. Mughal and N. A. Riza, "Compact acoustooptic high-speed variable attenuator for high-power applications," *IEEE Photonics Technology Letters,* vol. 14, no. 4, pp. 510-512, 2002.

[69] V. Y. Molchanov, S. I. Chizikov, O. Y. Markarov, N. P. Solodovnikov, V. N. Ginzburg, E. V. Katin, E. A. Khazanov, V. V. Lozhkarev and I. V. Yakovlev, "Adaptive acousto-optic technique for femtosecond laser pulse shaping," *Applied Optics,* vol. 48, no. 7, pp. C118-C124, 2009.

[70] F. E. Ellis, "Fast acousto-optic Q-switch laser". US Patent 4,308,506, 29 Dec. 1981.

[71] S. Schnell, V. G. Ostroumov, J. Breguet, W. A. Luthy, H. P. Weber and I. A. Scherbakov, "Acoustooptic Q-switching of erbium lasers," *IEEE Journal of Quantum Electronics,* vol. 26, no. 6, pp. 1111-1114, 1990.

[72] K. S. Morgan, Y. Li, W. Li, J. K. Miller, R. J. Watkins and E. G. Johnson, "Higher Order Bessel Beams Integrated in Time (HOBBIT) for Underwater Sensing and Metrology," in *CLEO: Applications and Technology 2019,* San Jose, 2019.

[73] S. N. Alperin, R. D. Niederriter, J. T. Gopinath and M. E. Siemens, "Quantitative measurement of the orbital angular momentum of light with a single, stationary lens," *Optics Letters,* vol. 41, no. 21, pp. 5019-5022, 2016.

[74] B. Jack, A. M. Yao, J. Leach, J. Romero, S. Franke-Arnold, D. G. Ireland, S. M. Barnett and M. J. Padgett, "Entanglement of arbitrary superpositions of modes within two-dimensional orbital angular momentum state spaces," *Physical Review A,* vol. 81, no. 4, p. 043844, 2010.

[75] J. Glaser, "High Power Nanosecond Pulse Laser Driver Using an GaN FET," in *PCIM Europe 2018; International Exhibition and Conference for Power Electronics, Intelligent Motion, Renewable Energy and Energy Management*, Nuremberg, 2018.

[76] K. Creath, "Phase-measurement interferometry techniques," *Progress in Optics*, vol. 26, no. 26, pp. 349-393, 1988.

[77] C. Gabriel, M.-A. Khalighi, S. Bourennane, P. Leon and V. Rugaud, "Monte-carlo-based channel characterization for underwater optical communication systems," *Journal of Optical Communications and Networking*, vol. 5, no. 1, pp. 1-12, 2013.